Sylwia Pawłowska

DIFFUSION AND MIGRATION OF NANO PARTICLES AND FILAMENTS SUSPENDED IN OSCILLATING FLOW

Acknowledgements

Diffusion and migration of nano particles and filaments suspended in oscillating flow

Sylwia Pawłowska

Institute of Fundamental Technological Research, Polish Academy of Sciences

Abstract

The subject of this work is an experimental analysis of the dynamics of nanoobjects suspended in a liquid. The research will make it possible to appreciate the role played by hydrodynamic and ionic interactions on the transport properties of Brownian solid spherical objects, as well as strongly deformable nanofilaments and macromolecules.

In the first stage of the work, an analysis of the Brownian fluctuations of spherical nanoparticles suspended in electrolytes was conducted. This report presents the results of the research carried out on the influence of the medium ionic strength and the wall on the size of the apparent (hydrodynamic) diameter of these spherical nanoobjects.

The second stage of the research concerns the mobility of deformable nanoobjects with a structure similar to long macromolecules. These are nanofilaments made of a hydrogel material. The original coaxial electrospinning technique was developed to produce them. This technique allows for the fabrication of core-shell fibres, with a highly elastic hydrogel filamentous core.

The mechanical properties of nanofilaments are evaluated by analysing their Brownian characteristics. The aim of this analysis is to determine the value of the persistent length of the object analysed, which is correlated with its bending Young's module. After assessing their full morphological characteristics and mechanical properties, the behaviour of hydrogel nanofilaments in the flow was analysed. An experimental system was used to analyse the dynamics of filament deformation and the migration of nanofilaments in the oscillating flow, simulating intercellular and inter-tissue flows in living organisms.

The basic goal of the analysis of the dynamics of nanofilaments is the possibility to use them as models of elongated biological particles, such as proteins and DNA. The analysis of their movement and deformation in the flow will support the verification of existing theoretical models, and will expand our understanding of the physical phenomena which are responsible for the folding dynamics of long biomolecules. Another very important aim of this work is to offer the possibility of using such highly deformable, biocompatible objects in biomedical applications.

Dyfuzja i migracja nano cząstek i filamentów zawieszonych w przepływie oscylacyjnym

Sylwia Pawłowska

Instytut Podstawowych Problemów Techniki, Polskiej Akademii Nauk

Abstrakt

Przedmiotem pracy jest eksperymentalna analiza dynamiki nanoobiektów zawieszonych w cieczy. Badania pozwolą na ocenę roli oddziaływań hydrodynamicznych, chemicznych i fluktuacji brownowskich na dynamikę i parametry transportu w mikro i nanoskali dla obiektów sferycznych, silnie deformowalnych filamentów i makromolekuł.

W pierwszym etapie pracy przeprowadzono analizę ruchów brownowskich sferycznych nanocząstek zawieszonych w elektrolitach. W pracy przedstawiono wyniki przeprowadzonych badań dotyczących wpływu siły jonowej medium oraz bliskości ścianki na wielkość średnicy hydrodynamicznej tychże sferycznych nano-obiektów (efektywnego oporu lepkiego).

Drugi etap badań dotyczył mobilności deformowalnych nanoobiektów o strukturze analogicznej do długich makromolekuł. Są to wytworzone z materiału hydrożelowego nanofilamenty. Opracowano oryginalną metodę ich wytwarzania, wykorzystującą technikę elektroprzędzenia współosiowego. Nowością w prowadzonych badaniach jest zamknięcie hydrożelowego materiału w postaci filamentów, charakteryzujących się dodatkowo wysoką elastycznością.

Po pełnej charakterystyce morfologicznej oraz właściwości mechanicznych, hydrożelowe nanofilamenty poddane zostały analizie ich zachowania w przepływie. Stworzony układ eksperymentalny, posłużył do analizy dynamiki deformacji oraz zjawiska migracji nanofilamentów w przepływie oscylacyjnym, symulującym przepływy międzykomórkowe i międzytkankowe w żywych organizmach. W pracy zbadane zostało zjawisko migracji w poprzek kanału. To zagadnienie jest istotne dla opisu transportu deformowalnych makromolekuł w kapilarach.

Przeprowadzone badania dynamiki nanofilamentów stwarzają możliwość ich wykorzystania jako modeli wydłużonych cząstek biologicznych (białka, DNA), weryfikacji istniejących już modeli teoretycznych, oraz zrozumienia zjawisk fizycznych odpowiedzialnych za fałdowanie i dynamikę zginania biomolekuł. Kolejnym bardzo ważnym celem pracy jest możliwość wykorzystania takich silnie deformowalnych, biokompatybilnych obiektów w zastosowaniach biomedycznych.

Symbols and abbreviations

The short list of most frequently used symbols and abbreviations is provided below:

a, b	-	long and short axis of the elongated object (rod, filament) [-]
a_l, σ	-	parameters of the matching function [-]
a_c	-	acceleration [m/s^2]
a_d	-	diffusion factor depending on the problem dimension (= 2, 4, 6) [-]
A	-	relative flexural stiffness [-]
A_s	-	cross section area of the rod [m^2]
AAm	-	acrylamide
AFM	-	Atomic Force Microscope
APS	-	ammonium persulfate
BIS-AAm	-	N, N'-methylene bisacrylamide
BSA-FITC	-	Bovine Serum Albumin conjugated with fluorescein
BU	-	degree of buckling (= d_c/L)
c	-	distance from the channel wall [m]
C_D	-	drag coefficient [-]
CHCl$_3$		Chloroform
d	-	particle (filament) diameter [m]
d_c	-	circle diameter [m]
d_e	-	short axis of ellipse encircling filament [m]
d_h	-	hydrodynamic diameter [m]
d_{ph}	-	physical diameter [m]
D_a	-	translational diffusion coefficient along principal axis [m^2/s]
D_b	-	translational diffusion coefficient along minor axis [m^2/s]
D_{ex}	-	experimental diffusion coefficient [m^2/s]
D_f	-	flexural diffusivity [m^2/s]
D_{th}	-	theoretical diffusion coefficient [m^2/s]
D_Θ	-	rotational diffusion coefficient [rad^2/s]
DMF	-	N,N-dimethylformamide

DLS	-	Dynamic Light Scattering
DLVO	-	Derjaguin-Landau and Verwey-Overbeek
E	-	flexural Young modulus of filaments [Pa]
E_r	-	relative elastic modulus [Pa]
E_x	-	extensional Young modulus of filaments [Pa]
EA1	-	AAm:Bis-AAm with mass ratio (w/w) 37.5:1
EA2	-	AAm:Bis-AAm with mass ratio (w/w) 20:1
EA3	-	AAm:Bis-AAm with mass ratio (w/w) 4:1
EDL	-	electric double layer
EE	-	end-to-end distance
EL	-	degree of elongation (= d_e/L_e)
EN1	-	NIPAAm:Bis-AAm with mass ratio (w/w) 37.5:1
EN2	-	NIPAAm:Bis-AAm with mass ratio (w/w) 20:1
EN3	-	NIPAAm:Bis-AAm with mass ratio (w/w) 4:1
F_d	-	hydrodynamic drag force [N]
F_e	-	elasticity force [N]
I	-	moment of inertia of filament [m^4]
IA	-	inclination angle
k_b	-	Boltzmann's constant [kg m^2/s^2 K]
k_x, k_y	-	elasticity constant, trap stiffness [N/m]
K	-	relative extensional (Hookonean) stiffness [-]
KCl	-	potassium chloride
L_e	-	long axis of ellipse encircling filament [m]
L	-	object (filaments) contour length [m]
$\underline{L}$	-	length-to-diameter ratio [-]
L_p	-	persistence length [m]
LiCl	-	lithium chloride
m	-	mass [kg]
$MSD, <x^2>,$	-	mean square displacement of particles [m^2]
$<(\Delta x(t))^2 >$		
$NiCl_2$	-	nickel chloride
NIPAAm	-	N, N-isopropylacrylamide
OT	-	Optical Tweezers
P	-	force [N]
Pe	-	Peclet number [-]
PDMS	-	polydimethylsiloxane
PLCL	-	Poly(L-lactide-co-caprolactone)
Q	-	flow rate through the channel [m^3/s]
R	-	radius of object [m]
R_e	-	the equivalent radius for a spherical intender [m]
R_t	-	the tip radius of curvature [m]
Re	-	Reynolds number [-]
Sp	-	Sperm number [-]

SDS	-	sodium dodecyl sulfate
SEM	-	Scanning Electron Microscope
Δt	-	time interval [s]
T	-	absolute ambient temperature [K]
TEMED	-	N,N,N',N'- tetramethylethylenediamine
U_r	-	average lateral migration velocity [m/s]
U_s	-	absolute slip velocity, ratio of translational velocity of particle (filament) to the calculated local fluid flow velocity [-]
W	-	channel width [m]
WLC	-	worm-like-chain model
$V(x,y,z,t)$	-	flow velocity of liquid in the channel [m/s]
V_{max}	-	maximum absolute flow velocity at the channel axis [m/s]
V_r	-	absolute relative migration velocity, ratio of averaged over observation time lateral velocity of particle (filament) to the maximum flow velocity V_{max} [-]
V_x, V_y	-	voltages, proportional to X and Y position of the incident beam of OT [V]
x	-	distance from the channel center line [m]
$\underline{x}$	-	relative distance from the channel center line [-]
x_0, y_0	-	displacement of the fitting window [m]
$x(t)$, $y(t)$	-	frame coordinates [-]
Δx	-	displacement of object [m]
κ	-	bending rigidity [Nm^2]
δ	-	indentation depth [-]
$\theta(t)$	-	orientation of filament [rad]
Θ	-	tangent angle [rad]
v_f	-	Poisson's ratio of the hydrogel [-]
η	-	dynamic viscosity of the carrier fluid [Pa s]
ρ	-	density of the carrier fluid [kg/m^3]
ω	-	angular oscillation frequency of the flow [rad/s]

Contents

12

Introduction

Transport processes in biological systems are based on laminar, creeping flows supported by molecular diffusion. The intercellular and cellular transport of molecules, subcellular organelles, and cells immersed in an aqueous environment is based on "stochastic" transport phenomena. Molecular diffusion becomes very efficient over short distances. While typical biomolecules need hours to be transported a few centimetres by diffusion, such transport takes less than 1s at subcellular distances. Therefore, the random movement of nanoobjects driven by intermolecular interactions initiates all living processes, whereas hydrodynamic interactions mainly play the role of a drag force, modifying species mobility.

The thermal fluctuations generated by molecules are not only noises. It has been demonstrated that such fluctuations are fundamental to the function of biological systems. Several results are possible with the same probability, unlike in a mechanical system where there is a deterministic result. In ensemble measurements, the obtained values – which are the average values of many molecules – have usually been wrongly interpreted as deterministic values. In biological systems, however, the average values are not necessarily effective, but the values of individual molecules play a decisive role [1, 2]. The biomolecular system may spontaneously fluctuate, and one of the two states occurs alternately. The preferential binding of ligands to one of the spontaneously fluctuating protein structures leads to their activation or deactivation. This mechanism appears essential for a long-scale evolutionary development of living species, and for the short-time creation of signalling paths for the early immune response of individual cells [3, 4].

To evaluate the role of diffusion in microsystems, we must discriminate between two specific configurations. The idealistic model is a free-moving spherical particle. Its mobility is well described at least in terms of physical geometry and displacements of its centre of mass. On other hand there are long molecules, described as strongly deformable chains of complex shape with different mobility. In the following we will attempt to describe some of the problems connected with the interpretation of the behaviour of such objects and share the following it observations and conclusions.

Particle size is a very important parameter in such branches of science and technology as materials science, medicine, pharmacology, biology, energy technology, and others. This size, understood as a linear length measure, can be uniquely defined only for spheres, and is referred to as the radius or diameter. In the case of shapes other than spheres, it is important to clearly define what the measured particle size is [5].

The hydrodynamic diameter is the apparent size representing a sphere having mobility of the physical object analysed. The phenomenon of the significant differences between hydrodynamic diameters, determined on the basis of the diffusion coefficient of nanoparticles, varies, and its physical value is fairly well known in literature. It is mainly based on effects related to the influence of the solvent. Such factors as the ionic strength or the distance from the wall, and the effect of a size, will be discussed in this paper. Other effects such as the surface structure of nanoparticles (associated with the presence of surfactants), agglomeration, and particle concentration are described in the following papers [6-14].

The hydrodynamic diameter provides information on the core, coating material, and the solvent layer attached to the particle as it moves under the influence of Brownian motion. The Stokes-Einstein equation can be used for calculating a hydrodynamic size from the diffusivity, although this ignores the influence of the ion cloud surrounding each particle and the relevant surface charge [15]. The most common theoretical models link these differences to the presence of the electric double layer [16, 17] surrounding the particles suspended in aqueous solutions. The electric double layer (EDL) is a diffuse layer of charges which surrounds the particles dispersed in liquid. It is created by the dissociation of the surface ions and the redistribution and adsorption of the ions from the solution near the particle surface. The charged liquid layer surrounding the particle is made up of two parts: (i) an inner region (Stern layer), where ions are strongly bound; (ii) an outer layer, defined as the diffuse region (Gouy Chapman layer), where ions are not so strongly attached as in the inner layer. It evidently modifies nanoparticles mobility.

The characterization of the flexibility or stiffness of biomolecules and polymers is essential for describing their structure and dynamics. Complex molecular interactions are usually described in a reduced way with spherical subunits (e.g. as in the case of model spherical proteins or bead-models of flexible polymers). Their dynamic structure may be regarded as stiff or semiflexible chains. Observing by optical means the dynamics of the flexible molecules suspended in a liquid one may evaluate their main mechanical properties, which are responsible for their complex behaviour, like folding-unfolding sequences of DNA chains. The description of such phenomena at a molecular scale, however, is still limited to very short length and time scales. At such scales it is difficult or nearly impossible to answer basic questions

about potential effects of hydrodynamic interactions, initiating or even causing some complex behaviours of long biological molecules. Our aim is to introduce micro-scale models of flexible objects, where length scale allows for precise optical measurements and the application of simple hydrodynamic models. Hence, it became necessary to develop techniques permitting the production of highly flexible fibres, with deformability and elasticity resembling long DNA chains.

In the following chapter the unique method for the fabrication of short nanofibres using the core-shell electrospinning technique is discussed. The proposed electrospinning method of producing gel-like fibres made it possible to obtain highly deformable hydrogel nanofilaments with a diameter of around 200 nm. The understanding of the behaviour of these highly flexible objects allows for the verification of existing theoretical models and can help to elucidate physical phenomena which are responsible for the folding and bending dynamics of long molecular objects.

The characterization of suspended micro- and nanoobjects depends mainly on their geometry and material parameters. In the case of spherical particles, their geometry is described by a single dimension, usually defined by their physical diameter. Deformable droplets or solid rods are characterized by three dimensions: height, width, and length. In addition, for droplets, the viscosity ratio characterizes their deformability in a shear flow. In the case of more complex structures, such as elongated and deformable fibres, apart from the dimensional parameters, their deformability is characterized by the fibres' material elasticity. The knowledge of these parameters is essential for describing the mobility of Brownian objects suspended in liquid.

Thermal energy causes random movements of molecules or small particles suspended in fluids. A particle suspended in a fluid kept at absolute temperature T has, on average, a kinetic energy $k_bT/2$ associated with movements along each coordinate, where k_b is the Boltzmann's constant. Such chaotic movements of particles (micro- and nanoobjects) are due to their collisions with molecules of the fluid in which they are suspended. This phenomenon was discovered by the Scottish biologist Robert Brown (1827).

William Sutherland (1905), Albert Einstein (1905) and Marian Smoluchowski (1906) concluded that the observed Brownian movement of the particles suspended in a liquid is a direct proof of its molecular structure [18]. They suggested that the study of the mobility of Brownian particles permits the detailed analysis of solvent properties. Their work proved the direct relation between the mean square displacement of the observed particles (MSD) and the diffusion coefficient D [19]. The MSD value is evaluated as a time or space average over a large number of observed displacements.

For the spherical particles suspended in a homogeneous liquid, the diffusion is determined by the translational diffusion coefficient and the usually neglected, rotational diffusion coefficient. In the case of asymmetric particles (elongated shape objects), non-isotropic translational diffusion coefficients are possible: along the main axis (D_a) and along the minor axis (D_b). Here, also the rotational diffusion coefficient (D_θ) [19, 20] is not negligible.

Within the limit of small Reynolds numbers and long-time scales, the Brownian diffusion coefficient for the translational motion of isolated spherical particles can be evaluated using a simple formula given by Stokes law for a sphere moving in a viscous liquid. The theoretical evaluation of drag forces for ellipsoidal objects moving in viscous liquid makes it possible to calculate the corresponding diffusion coefficients of long, thin ellipsoids [21].

The problems of characterizing the diffusion of flexible objects, such as nanofilaments or long molecular chains, can be solved only on a statistical basis due to the large number of degrees of freedom. There are not just translational and rotational motions of the object to be analysed. The flexibility of rubber-like, elongated elastic objects is usually described by two parameters: stretching and bending. Such an approach makes it possible to adopt the so-called warm-like-chain (WLC) approximation, which is widely used for modelling polymer chains in different simulation methods [22-25]. Another approach used in polymer science is a dumbbell model. In this model, two particles that represent two ends of the object (e.g. a filament) are connected by a spring. The spring represents entropic forces. The end-to-end mobility vector describes stretching and orientation (conformation) of the dumbbell, thus representing the mechanics of the deformable object. The mobility vector of the centre-of-mass describes the translational transport of a dumbbell in a flow field [26, 27].

The microfluidic systems developed for focusing and sorting cells and biological objects are based on the hydrodynamic interactions responsible for the cross-flow migration of selected objects suspended in the carrier liquid. The cross-flow migration problem already starts to be complex in the case of elongated objects (e.g. rod-like particles, molecules). In most cases, microscale migration effects of elongated objects are simplified to an ellipsoidal model introduced by Jeffrey [28, 29], and possibly applied to stiff fibres. The migration problem becomes quite complex in the case of long flexible objects (e.g. filaments, macromolecules). Without a doubt, this phenomenon is affected by changes in conformation, object elongation, or tumbling.

The cross-flow migration of fibres or other long objects in a channel flow is one of the fundamental issues of modern lab-on-chip techniques, being important in a variety of biological, medical, and industrial contexts (e.g. Brownian dynamics of proteins, DNA or biological polymers, cell movement, movement of microbes, and

drug delivery) [30]. The full analysis of objects suspended in the liquid are affected not only by their geometry but also by their behaviour. In the case of elongated objects such as filaments, this behaviour is more complex and dependent on mechanical properties.

Here, we explore this problem by constructing long, elastic nanocariers, with yet-unexploited applicability in biology and medicine. A major concern was that of being able to deliver drugs or other pharmaceutical agents to patients in the most physiologically acceptable manner. In this paper we focus on application of polymeric fibres as a drug delivery system. A very important principle for the use of polymer nanofibres for drug delivery is that drug particulate dissolution rates increase when the drug concentration and corresponding carrier surface area are increased. Polymer nanofibres for controlled drug delivery are characterized by several advantages, such as, for example, large surface area to volume ratio [31]. The possibility of delivering topical drugs opens up a number of application opportunities. The potential advantages of this delivery method include the possibility of doing so in a targeted manner, thus reducing the total drug dose and, consequently, its toxicity for non-target sites, also preventing the need for other systemic treatments, such as oral administration [32]. In drug delivery systems for biomedical application, the electrospun fibres help encapsulate the therapeutic agent [33].

Our experiments performed in transparent microchannels permitted the precise, microscopic analysis of examined objects, i.e. nanoparticles and hydrogel nanofilaments. Understanding the relationship between particle or filament microstructure and macroscopic flow properties opens the door to designing nanoobjects, which could be transported by body fluids for dedicated drug release and/or local tissue regeneration. It should be noted that, at the present time, the analytical/numerical modelling of such processes is difficult and not sufficiently credible, thus leaving experiments as the only alternative.

The report is organized as follows. In Chapter 2 we will present the list of all materials used in the experiments, basic apparatus, descriptions of electrospun core-shell nanofibers preparation, and microfluidic devices preparation. In the next chapter (Chapter 3) full analysis of Brownian diffusion of spherical polystyrene particles will be given. We check influence of ionic strength of medium and wall effect on the value of nanoparticle hydrodynamic diameter. Experiments with lateral migration of nanoparticle under the influence of an oscillatory flow will also be performed. In Chapter 4 we will focus on highly deformable hydrogel nanofilaments. After morphological and mechanical characterisation, we will analyse their behaviour in Brownian fluctuations and oscillatory flow conditions. Especially we focus on changes of filament conformation and lateral migration as a result of oscillatory flow.

Finally, in Chapter 5 we show the results of analyses of our highly deformable hydrogel nanofilaments as controlled drug delivery systems.

More detailed description of the issues covered in the introduction, as well as the used apparatus, experiments and sample preparation techniques is included in the doctoral thesis: *"Dynamics of nano objects suspended in liquids: experimental analysis"* [34].

Materials, preparation, and apparatus

2.1. Materials

2.1.1. Solid spherical particles

Three different types of solid spherical particles were used for Brownian motion analysis. Fluorescent polystyrene particles (emission wavelength of 550 nm and physical sizes 48 nm, 63 nm, 100 nm, 300 nm, 600 nm, 1000 nm, 3200 nm, dispersed in 1% (w/w) aqueous solution [Fluoro-Max Red Aqueous Fluorescent Particles – Thermo Scientific™]), carboxylate-modified polystyrene particles (95 nm, 200 nm, 328 nm, Fluoro-Max Dyed Carboxylate- Modified Microparticles – Thermo Scientific™), and gold particles (60 nm, 100 nm, Aldrich) were studied. Nanoparticles were suspended in water or salt (KCl, LiCl and $NiCl_2$ (Sigma-Aldrich)) solutions with different concentrations.

2.1.2. Polymer filaments

Hydrogel filaments were produced using the following chemical components: Poly(L-lactide-co-caprolactone) (PLCL, 70% L-lactyde and 30% caprolactone unit, Corbion Purac, Netherlands), chloroform ($CHCl_3$, POCh, Poland), N,N-dimethylformamide (DMF, POCh, Poland), Bovine Serum Albumin conjugated with fluoresceine (BSA-FITC, Sigma Aldrich, Poland), acrylamide (AAm, Sigma Aldrich, Poland), N,N-isopropylacrylamide (NIPAAm, 97%, Sigma Aldrich, Poland), N,N'-methylene bisacrylamide (BIS-AAm, 99.5%, Sigma Aldrich, Poland), ammonium persulfate (APS, 98%, Sigma Aldrich, Poland), N,N,N',N'-tetramethylethylenediamine (TEMED, 99%, Sigma Aldrich, Poland), and photoinitiator (2-Hydroxy-4′-(2-hydroxyethoxy)-2-methylpropiophenone) (Irgacure 2959, 98%, Sigma Aldrich, Poland).

2.2.   Preparation methods

2.2.1. Electrospun core-shell nanofiber preparation

Nanofibres and nonwovens made of them are unique nanostructures with an extraordinary potential in both technical and medical areas. Filter applications, functional textiles, fibre reinforcement, catalysis, drug delivery, wound healing, and tissue engineering are just a few examples of their potential applications. The term nanofibre commonly applies to a fibre with a diameter of less than 1 micrometre. The manufacture of objects characterized by such a small size requires the use of special techniques.

Electrospinning is a process that forms nanofibres through an electrically charged jet of polymer solution or polymer melt. This technique provides a simple and versatile method for producing ultrathin fibres from a wide range of materials that include polymers, composites, and ceramics. Electrospun fibre diameters usually range from tens of nanometres to a few micrometres [35, 36].

In this work core-shell electrospinning is used to fabricate hydrogel nanofilaments; in our opinion this is the only technique that enables obtaining soft hydrogel filaments by encapsulating them in a mechanically stable polymeric shell [37].
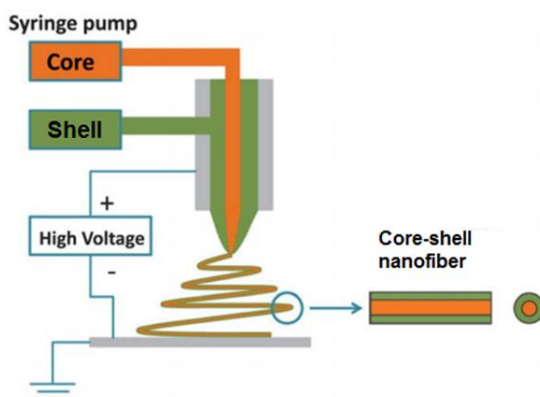
Figure 2.1. Coaxial electrospinning setup for core-shell fibres [38].

During the core-shell electrospinning, two different solutions are dosed at the same time through the inner and outer needles, and charged in the same way as in the classic single nozzle (Fig. 2.1). The resulting core-shell fibre consists of two material structures in which one is surrounded by the other. The coaxial electrospinning depends on the same parameters as those in conventional electrospinning [38-40].

Using precisely controlled syringe pumps, the flow rate of each component can be varied to control
the dimensions of the core and shell material [41, 42], as well as the overall nanofibre diameter [43]. For proper encapsulation of the core material, the flow rates of both components should be carefully matched. If the core-to-shell flow rate ratio is too small, an insufficient outflow of core solution cannot ensure a continuous smooth core phase, and only a chain of small droplets is encapsulated [38].

The electrospinning shell solution was prepared by dissolving 1 g of PLCL polymer in 10 g of mixture of DMF and CHCl$_3$ 1:9 (w/w). The core solution (10 wt.% AAm/BIS-AAm or NIPAAm/BIS-AAm) was prepared by dissolving 2.24 g of AAm (or NIPAAm) and 0.06 g of BIS-AAm in 20.7 g of deionised water in the ratio of 37.5:1 of AAm or NIPAAm and BIS-AAm, respectively. Mixtures of core polymer AAm (or NIPAAm) and BIS-AAm with mass ratio of 20:1 and 4:1 were also prepared (Table 2.1). PLCL polymer solution and core mixture were prepared one day before nanofibre fabrication. Before electrospinning, 10 µl of APS and 0.007 g of BSA-FITC were mixed with 1 ml of NIPAAM (or AAm) / BIS-AAm solution. The addition of a small amount of BSA-FITC made it possible to use fluorescence for image acquisition and to study protein release dynamics [44]. Lastly, a suitable amount of TEMED (1 µl) was added to the solution of AAm/ BIS-AAm/APS which was then vigorously shaken. The addition of TEMED triggered hydrogel polymerization (Fig. 2.2 (a)).
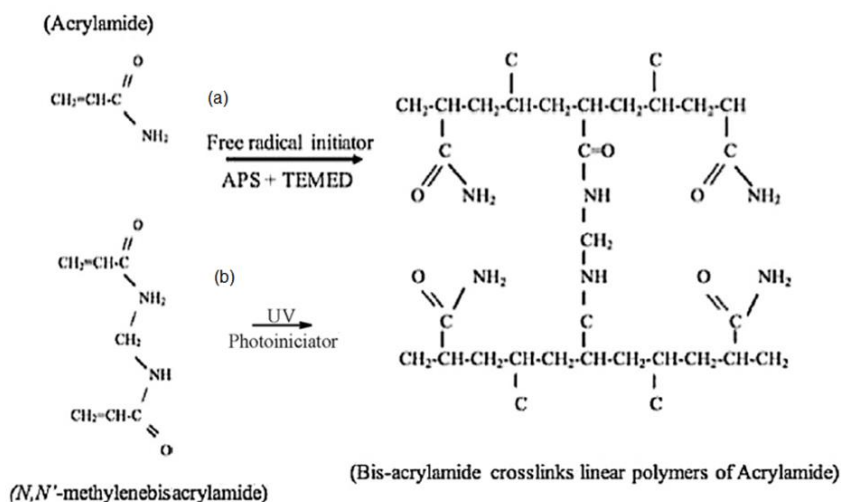

Figure 2.2. Polymerization process of AAm-BIS-AAm hydrogel: (a) with a free radical initiator; (b) with photoinitiator and UV light [45, 46].

To improve the control of the polymerization process an alternative method for preparing the hydrogel core was tested using a photoinitiator (Irgacure 2959) instead of APS and TEMED as the molecule that triggers the polymerization reaction under

the influence of UV irradiation (Fig. 2.2 (b)). This procedure made it possible to control the polymerization of the core-forming solution inside the PLCL shell accurately and easily. Based on bibliographical data [47-49], the used here proportion of polymeric components forming the hydrogel core (NIPAAm/AAm and BIS) and the photoinitiator (PhIn) is given in Table 2.1.

Table 2.1. Concentration of components for core-shell fibre preparation.

		(a)			(b)
		37.5:1	**20:1**	**4:1**	**37.5:1**
Core (10%)	**AAm / NIPAAm**	100 [mg/mL]	100 [mg/mL]	100 [mg/mL]	100 [mg/mL]
	BIS-AAm	2,67 [mg/mL]	5 [mg/mL]	25 [mg/mL]	2,67 [mg/mL]
	BSA-FITC	7 [mg/mL]			
	TEMED	1 [μL/mL]			-
	APS	10 [μL/mL]			-
	PhIn	-			5 [mg/mL]
Shell (9%)	**PLCL**	1 [g]			
	CHCl₃	9 [g]			
	DMF	1 [g]			

Monomers and photoinitiator were dissolved in deionized water no later than one day before the electrospinning process. Before starting the electrospinning process, the core mixture solution must be degassed by bubbling argon for half an hour. Degassing is important for removing oxygen from the core solution, thus avoiding the formation of radicals through a reaction that competes with the hydrogel polymerization. Another method for removing oxygen involves the use of low pressure (20 mbar environment) for degassing. However, it will reduce the volume of the mixture by the solvent evaporation and the concentration of polymer components becomes different from the initial one and difficult to estimate.

The polymerization process (with a photoinitiator as the initiator of this process) was carried out using a UV lamp (density of power 225 mW/cm^2) for 1 minute under a cooling bath. The average temperature of the bath was between 2ºC and 4ºC.

The cooling of hydrogel during the polymerization process is necessary to prevent any change due to overheating in the structure of the hydrogel. The temperature of hydrogel after irradiation should be not higher than 32ºC, in order to ensure that the sample does not lose water, the concentration of polymers does not change, and – most importantly – to avoid inhomogeneity during the formation of the polymer cage. Acrylamide is much less sensitive to high temperatures during a polymerization

process. Its Lower Critical Solution Temperature (LCST) is higher (above 50ºC) than in the case of NIPA (32ºC) [48-51].

2.2.2. Preparation of microfluidic devices

The first step in microfluidic device fabrication includes the design of the microchannel architecture by producing a mask. The mask is a film made using the CtF (Computer to Film) exposure method, on which the areas presenting the microstructure scheme are transparent. It is necessary for the UV light to pass through these areas in the next step of photolithography. Therefore, the mask is a negative of the design of the microfluidic system. Then the film is used to prepare matrices using the negative lithography technique. This technique, called soft lithography, is commonly used in the fabrication of PDMS microfluidic chips. The essential materials for the fabrication of the matrices are a backplate (silica wafers) and a suitable photoresist (Su-8 2075, MicroChem). Su-8 is a group of epoxy-based negative photoresists which, during exposure to UV, become crosslinked. Only non-illuminated areas of photoresists are removed from the silicon wafer by the developer solvent. This procedure requires the use of specific laboratory equipment as a spin coater (SCS G3 Spin Coater Series) and an UV lamp (DYMAX Flood Lamp 5000).
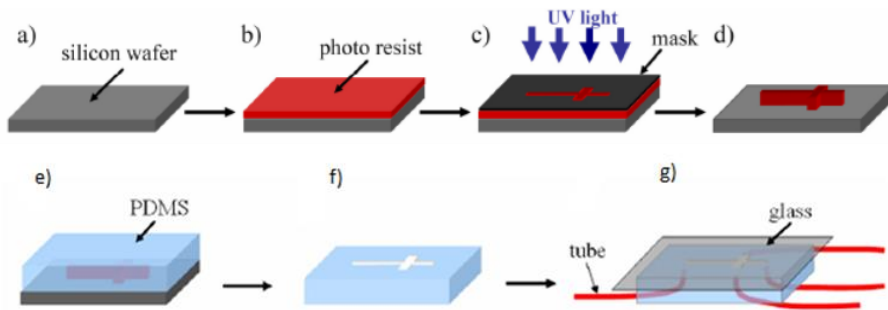
Figure 2.3. Photolithography and fabrication of a PDMS microfluidic system [26].

The prepared matrices are used to achieve a proper microchannel architecture, by stamp the thermocuring elastomer of poly(dimethylsiloxane) (PDMS, Dow Corning), which perfectly reflects the convex elements of the matrix. The fabricated PDMS microchannel is then sealed with a microscope glass cover slip (joining method using oxygen plasma) used for the observation of the phenomena studied under a microscope. A typical scheme for the production of PDMS microfluidic systems is shown in Fig. 2.3.

2.3. Apparatus

The basic microscopes used for imaging are a Nikon Eclipse E-50i epi-fluorescent microscope with double-shutter CCD camera and double-pulsed Nd:YAG laser, a Leica AM TIRF system based on inverted fully automated microscope Leica DMI6000 with AFC, an environmental chamber, a set of lasers and 120 W mercury metal halide lamps, and a confocal microscope Leica TCS SP5 X with environmental chamber. For image recording three different cameras were used: EM-CCD Hamamatsu C9100-02 (1000x1000 pix, monochrome, cooled, high EM gain, 256 fps), Leica DFC365FX (1391x1040 pix, monochrome, cooled, 122 fps), and Leica DFC295 (2048x1536 pix, colour, 12 fps). For the analysis of mechanical properties (in the case of filaments) and micro-object morphology, an atomic force microscope (AFM, Ntegra Spectra, NT-MDT, Limerick, Ireland) and portable scanning electron microscope JSM-6010PLUS/LV were used.

An innovative device used to analyse the interaction of spherical particles with the wall of the microchamber (wall effect evaluation) was Optical Tweezers, developed at IPPT PAN and based on the inverted microscope (IX71, Olympus Optical Co. Ltd, Tokyo, Japan) which is part of a commercial AFM (Ntegra Spectra, NT-MDT, Limerick, Ireland) [52].

In order to be able to produce hydrogel nanofilaments for further analyses the environmental chamber for electrospinning built at IPPT PAN was used. The electrospinning chamber is equipped with a polymer dosing pump system, a high voltage generator, and a grounded collector. Another important apparatus created at IPPT for the purposes of the present study is a pulsating pump for generating an oscillatory flow. Its operation principle is based on the use of a rotating disk, which is mounted eccentrically on the stepper motor (Fig. 2.4. The disk presses the pushing arm and, consequently, closes and opens the cross-section of the elastic tube filled with the working liquid, thus generating a flow in the microchannel connected to it.
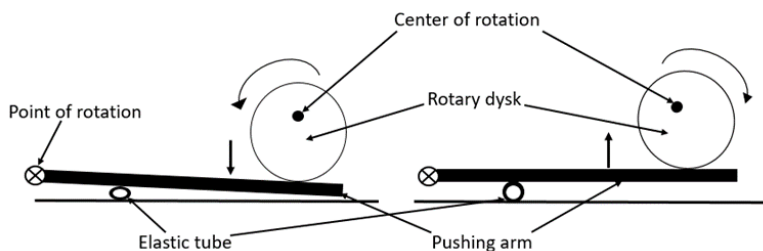

Figure 2.4. Scheme of the work idea of the pulse pump.

Mobility of spherical particles

Over one hundred sets of single-particle tracking experiments were performed to evaluate the role played by the particle size and ionic strength of the suspension liquid on mobility the particle. These experiments aimed to elucidate the background of reported discrepancies between physical and measured hydrodynamic diameters in nano- and microscale experiments with colloidal suspensions.

3.1.   Morphological characteristics of solid particles

The morphology of commercially available spherical particles was tested using SEM and AFM microscopies. These measurements were necessary to confirm the physical size of the particles used in experiments, in order to determine the hydrodynamic size of the particles tested.

Pieces of appropriately purified silica wafer were used as a substrate on which the analysed particle samples were placed. These were washed with solvents – deionized water, isopropanol, and acetone in succession – and then subjected to compressed air drying and oxygen plasma treatment (for about 10 minutes), thus obtaining an additional cleaning and increased hydrophilicity of the substrate.

After drying, samples were analysed using an AFM (Ntegra, NT-MDT), equipped with a rectangular silicon cantilever (CSG01, NT-MDT), which worked in contact mode to obtain the sample surface topography.

For SEM analysis, particle samples were sputtered with gold using a Polaron model SC7620 mini sputter coater (Quorum Technologies Ltd., Ashford, UK). Measurements were obtained using a SEM model JSM 6390 LV microscope (Jeol, Japan).

3.2. Experiments on Brownian diffusion

3.2.1. Sample preparation

The tables below (Tables 3.1 a, b, c) summarize the parameters of the particles and experimental conditions used for Brownian motion analysis. Particle concentration is given as a volume concentration.

Table 3.1a. Spherical polystyrene particles.

Physical particle size [nm]	Solution	Concentration of solution	Concentration of particles*
63	H_2O	-	1:500000
	KCl	0.1 mM; 1 mM; 10 mM	1:500000
100	H_2O	-	1:100000 1:250000 1:500000
	KCl	10^{-9} mM; 10^{-8} mM; 10^{-6} mM; 10^{-5} mM; 10^{-4} mM; 10^{-3} mM; 0.005 mM; 0.01 mM; 0.05 mM; 0.1 mM; 1 mM; 10 mM; 40 mM; 80 mM; 100 mM	1:100000 1:150000 1:250000
	LiCl	10^{-9} mM; 10^{-8}; mM; 10^{-6} mM; 10^{-5} mM; 10^{-3} mM; 0.1 mM; 10 mM	1:150000 1:250000
	$NiCl_2$	10^{-9} mM; 10^{-7}; mM; 10^{-6} mM; 10^{-5} mM; 10^{-3} mM; 0.1 mM; 10 mM	1:200000 1:250000
300	H_2O	-	1:150000
600	H_2O	-	1:100000
1000	H_2O	-	1:50000

* From original solution where the particles were supplied at a nominal 1% solids after dilution with deionized water.

Table 3.1b. Carboxylate-modified polystyrene particles.

Physical particle size [nm]	Solution	Concentration of particles*
100	H_2O	1:1000
200	H_2O	1:1000
300	H_2O	1:1000

* From original solution where the particles were supplied at a nominal 1% solids after dilution with deionized water.

3.2 Experiments on Brownian diffusion

Table 3.1c. Gold particles.

Physical particle size [nm]	Solution	Concentration of particles*
40	H_2O	1:10000
60	H_2O	1:10000
100	H_2O	1:10000

* From original solution where the particles were supplied at a nominal 1% solids after dilution with deionized water.

3.2.2. Observation methods

In the case of gold particles (not fluorescent), the PDMS chamber was illuminated on one side with a laser, while a camera recorded images perpendicularly to the reflection of the light wave on the surface of particles. To avoid the impact of the bottom wall, which could change the movement dynamics of particles, the focal plane of the microscope was set at the middle of the channel. Images were taken at specific time intervals (0.5-2 fps) and exposition time (100 ms), which was adjusted to obtain the greatest possible brightness of the particles. Over 1,000 images were taken for each sequence (Fig. 3.1).
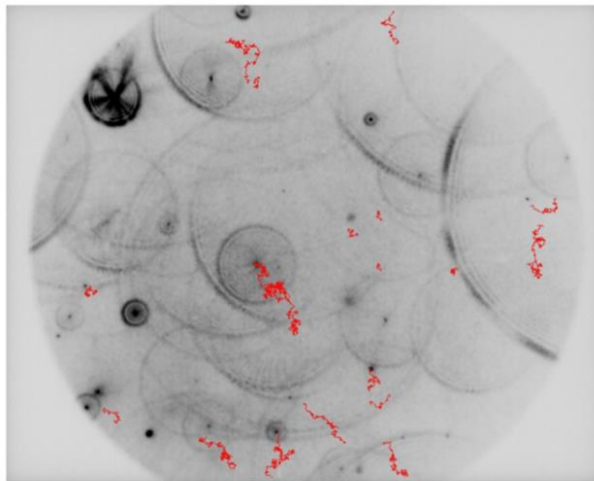

Figure 3.1. Trajectories of 100 nm gold particles dispersed in water and observed under the microscope (red tracks). Several circles indicate diffraction rings from immobile disturbances, mostly particles settled at the bottom wall.

3.3. Diffusion coefficient evaluation (Brownian)

Before analysing the Brownian motion (particle displacements), the raw experimental images had to be filtered to detect the positions of particles. A denoising Wiener filter built in Matlab software was used. For each detected particle the image brightness $f(x,y)$ was fitted using the equation:

$$f(x,y) = a_1 exp\left(\frac{-(x-x_0)^2}{2\sigma_x^2} - \frac{(y-y_0)^2}{2\sigma_y^2}\right)$$ (3.1)

where x_0, y_0 – displacement of the fitting window; a_1, σ – parameters of the matching function.

Knowing the position of the particle in each picture, time interval between frames, and scale of the microscope-camera system, we were able to calculate the trajectory of the particle in a series of photos (Fig. 3.1). The measured diffusion coefficient was calculated for each particle track obtained from such analysis, using the following equation:

$$D_{ex} = \frac{<MSD>}{a_d \Delta t}$$ (3.2)

where $<MSD>$ – mean square displacement; $a_d = 2, 4, 6$ – factor based on the problem dimension (for 2D analysis $a_d = 4$); Δt – time interval between images.

Experimental results were compared with the theoretical diffusion coefficient calculated as:

$$D_{th} = \frac{k_b T}{3\pi\eta d_{ph}}$$ (3.3)

where k_b – Boltzmann constant; T – temperature inside the channel; η – dynamic viscosity of the fluid; d_{ph} – diameter of the particle (physical size).

For each series, the calculated arithmetic mean and standard deviation for experimental diffusion coefficient (D_{ex}) were compared with the theoretical diffusion coefficient (D_{th}) and represented as the ratio of diffusion coefficients D_{ex}/D_{th}.

For a few experimental runs, the diffusion coefficients, determined on the basis of particle tracking experiments, were compared with the data obtained from the commercially available Malvern NanoSight NTA hardware (NanoSight Ltd., Minton Park, Amesbury, UK).

The experimentally determined particle diffusion coefficient made it possible to determine its hydrodynamic diameter. The following formula was used to calculate this value:

$$d_h = d_{ph} \frac{D_{th}}{D_{ex}}$$ (3.4)

where: d_h – hydrodynamic diameter; d_{ph} – physical diameter, D_{th} – theoretical diffusion coefficient calculated from the Stokes-Einstein equation ; D_{ex} – experimental diffusion coefficient.

3.4.   Wall effect evaluation

To investigate the impact of the microchannel wall on the mobility of solid particles, we used the Optical Tweezers (OT) system developed at IPPT PAN. For this purpose, polystyrene particles (1μm diameter) suspended in pure deionized water and in four different potassium chloride solutions were used. In the experiment, the particle suspension was obtained by a 1:100 volume dilution of 1% particle solution samples.

The experiments were performed inside a PDMS microfluidic chip (Fig. 3.2) with 60 μm deep channels filled with water or salt solutions. The temperature of the experimental chamber was set to 295 K. Before each experiment microchannels were degassed under a vacuum pump (20 mbar) for one hour, and then they were placed for several minutes into water or KCl solution.
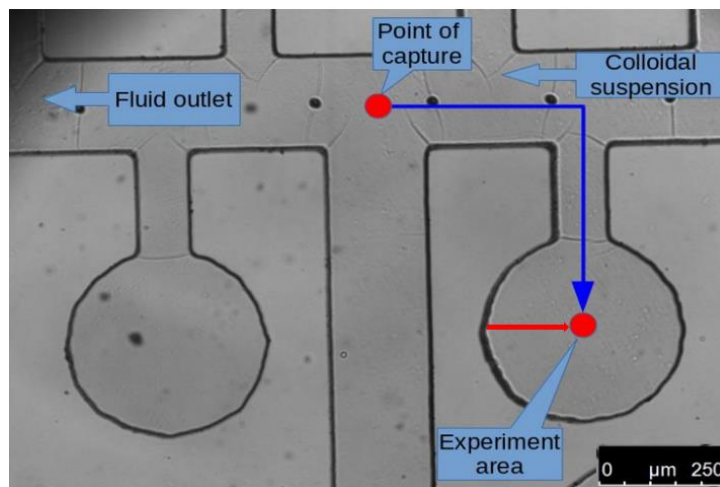

Figure 3.2. Microchannels with round wells designed for experiments with optically trapped particles. Circle chambers had a diameter of 200 μm and depth of 60 μm. The red arrow indicates the direction in which the wall moves as a result of the microscopic table moving [52].

Round wells have only one way-in which helps provide a flow-free chamber. Once the Optical Tweezers catched the particle we transferred it to the chamber by moving the microscopic table with microchannels. Than the measurement of particle displacements starts (Fig. 3.3). Thanks to multiple wells we were able to conduct several experiments in the same microchannel.
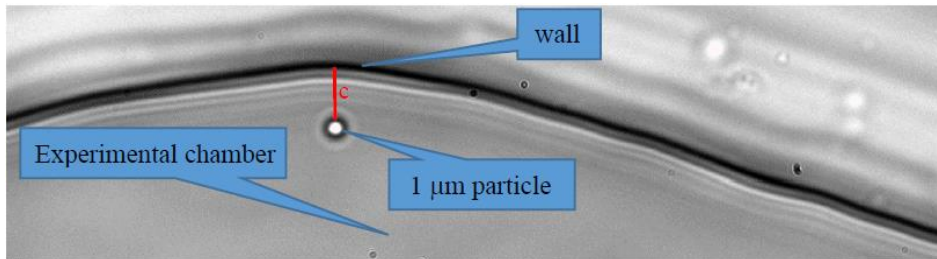

Figure 3.3. Starting position of 1 μm particle trapped by OT during a single experiment inside the chamber. The red line indicates the direction of the particle motion tagged by OT into the wall; *c* is the shortest distance from the wall. The black contour in the image indicates the wall.

Particles were set at an average distance of 3-8 μm from the wall, and then tagged into it. The particle distance from the bottom of the chamber was 5μm. The speed of the table movement was 500 μm/s, the size of the movement step was 50 nm in the direction of the y axis. After each movement, the microscopic table stopped and the particle-wall interactions measurement was started. At each position of the particle its Brownian motion was indicated by OT signal fluctuations. The mean displacement of the particle position within OT focus indicated the net force due to the particle-wall interactions. The recording speed of the particle Brownian motion was equal to 1 kHz. A single recording lasted 2 seconds. The first 0.2 seconds of measurement were used to stabilize the system. The average for a given measurement point was calculated from the next 1.8 seconds (average value from 1800 time points). Each series consisted of 50-200 measuring stop points. Laser power was set to 10% of the maximum, which is equal to 9 mW. The moment of contact between the particle and the wall was determined as the time step when the particle falls out from the optical trap area and the amplitude of its vibrations rapidly decreases.

3.5.   Lateral migration

Cross-stream migration is a phenomenon that has been investigated – over many decades – for micro- and nanoobjects under the influence of the fluid flow in which they are suspended. In presented here experiments that investigated the migration process an oscillatory flow was used for two reasons. Firstly, it allows for a long time

analysis without the need to create very long channels or a complex tracking measuring setup. Secondly, such an oscillatory (pulsatile) flow simulates the intracellular fluid motions in the human body.

Fluorescent polystyrene particles with a diameter of 1 μm, suspended in a 10 mM KCl solution, were used. This salt concentration was chosen in order to obtain the conditions in which the double electric layer is most compressed and the values of physical and hydrodynamic particle diameters are similar. To avoid particle-particle interactions, it was important to obtain a low concentration of particles in the liquid. For this reason, a particle solution with a concentration of 1:20000 (from 1% solids) was used.

Microfluidic channels with a rectangular cross-section (200 μm x 60 μm) and a length of 30 mm were used in experiments. Microchannels were fabricated by soft lithography from polydimethylsiloxane (PDMS). At one end, the channel was connected by a steel capillary to a home-built pulsatile pump, at the other end with a syringe filled with a suspension of spherical particles (Fig. 3.4). The same experimental setup was used to investigate the lateral migration of elongated hydrogel nanofilaments, which will be discussed in Chapter 4.
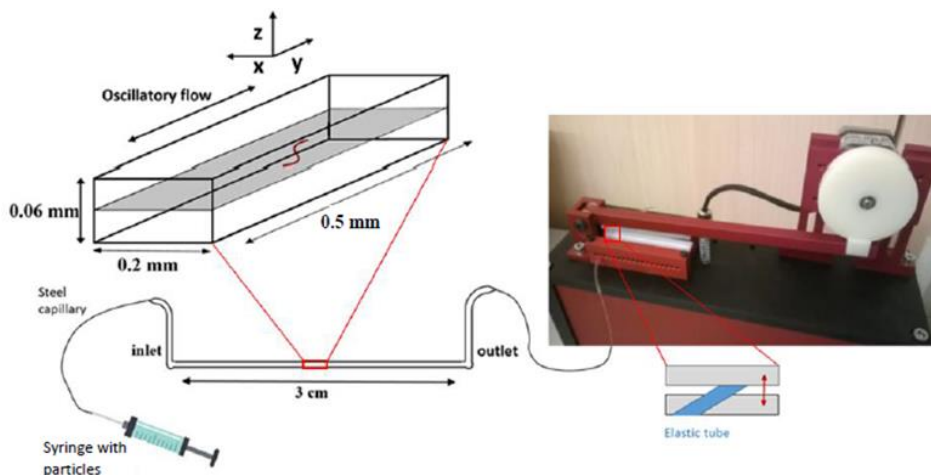
Figure 3.4. Experimental set up for the analysis of nanoobject dynamics. The experimental channel and pulsatile pump were connected with the reservoir (syringe) by a steel capillary.

An inverted epifluorescence microscope (Leica AM TIRF MC) with a 20x/0.40 NA microscopic lens, an appropriate set of filter, and a mercury lamp (Leica EL6000) as a source for fluorescence excitation were used for particle observation. For recording particle displacements, using from 500 to 2,000 individual images for each series, a high-gain EM-CCD camera (C9100-2, Hamamatsu) was employed. Particles were observed at 15 mm from the channel inlet and 30 μm above the bottom wall of

the microchannel. Experiments were performed inside the environmental chamber of the microscope with a stabilized temperature of 302 K.

The maximum flow velocity amplitude (V_{max}) used for the experiments was between 0.06 mm/s and 0.27 mm/s, while the forcing frequency varied between 0.26 Hz and 0.59 Hz. The flow of Newtonian liquid through the microchannel with a rectangular cross-section was characterized by a small Reynolds number *Re* (= $V_{max}W\rho/\eta$) based on the channel width *W*, which varied in the range of 0.01 to 0.07.

The variation in the distance between the position of the analysed particle and the microchannel centreline was measured. This distance changed periodically during each oscillatory flow cycle, hence the instantaneous lateral migration velocity periodically varied. The absolute value of the particle migration velocity U_r was defined as the ratio of the average total lateral displacement of particles and the total observation time.

3.6.   Evaluation of the focal depth

The evaluation of the particle lateral migration is based on the assumption that particles remain within the plane of observation defined by the microscope focal depth. This was distinguished by analysing only sharp, fully bright images of particles. To determine the range of distances in which the objects observed by the optical device appear sharp, the focal depth was experimentally determined. For this purpose, we immobilised 1 μm fluorescent particles suspended in the experimental channel and recorded their images by changing the vertical position of the microscope table. Results of this experimental evaluation are presented in Fig. 3.5.
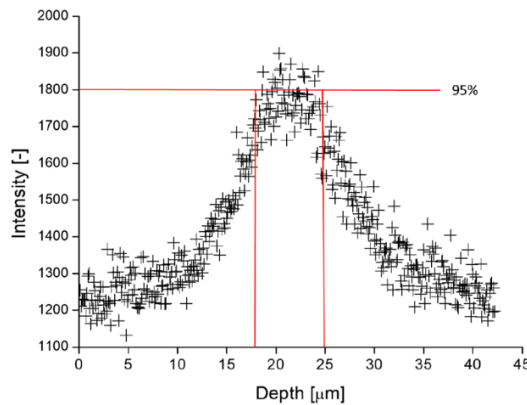

Figure 3.5. Graph indicating the focal depth of the experimental system. The intensity of the fluorescent particle was recorded for 400 steps of the microscope table moved from the top wall to the bottom wall of the channel, where the distance between steps was equal to 100 nm. The evaluated focal depth is about 10 μm.

A graph of the intensity of the particles' brightness based on depth (Fig. 3.5) made it possible to estimate the thickness of the focal plane for the microscope lens 20x / 0.40 NA used in the experiments. This value depends on factors such as lens magnification and aperture, therefore it will vary when these parameters are changed.

3.7.   Results and discussion

3.7.1. Particle morphology

The analysis conducted using AFM and SEM microscopes confirmed the physical size of the tested particles (Fig. 3.6).

(a)   (b)

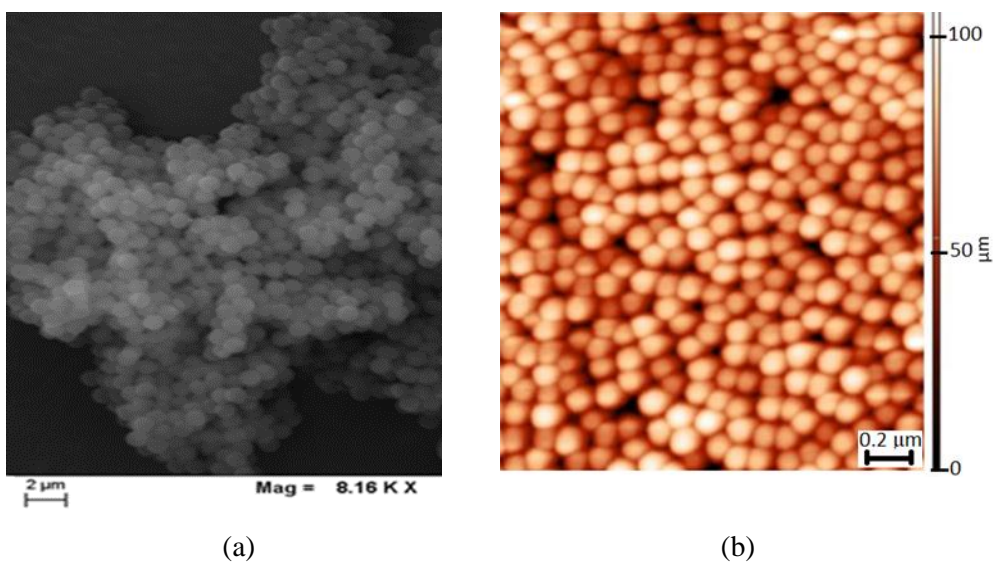Figure 3.6. (a) 1 μm polystyrene particles observed by SEM; (b) AFM image of 100 nm polystyrene particles, substrate: silicon.

It is worthwhile to note that some interesting honeycomb structures were observed during the imaging of the particle layer previously suspended in a mixture of Triton X-100 / methanol (Fig. 3.7), demonstrating the attempt at self-organization which is typical in building biological tissues.
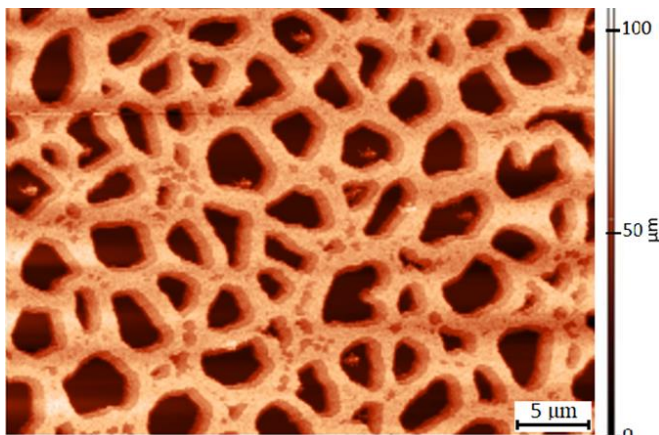
Figure 3.7. AFM surface topography of 100 nm polystyrene particles immersed in Triton X-100/Methanol (1:1); particles concentration 1:100, poured onto the silicon substrate.

Similar structures were not observed with other surfactants in methanol (SDS and Tween). In addition, it was noted that the hole sizes varied with different Triton X-100 to the evaporated methanol ratios. This was probably related to the evaporation of methanol, because large amounts of evaporated methanol leave large spaces between the particle aggregates. In practice, this phenomena could be used to modify the pattern of such structures according to needs, for example by building appropriate matrixes for cell culture proliferation.

3.7.2. Hydrodynamic diameter for different types of particles

Polystyrene particles, carboxylate-modified polystyrene particles, and gold particles of various sizes were suspended in deionized water and their Brownian motion analysed. Following the procedure outlined earlier in this chapter, the diffusion coefficients determined were used to calculate the hydrodynamic diameter of the investigated particles. The final results, based on a series of thousands of measurements, each of which consisted of 500 to 1,000 frames, are shown in Table 3.2.

The results obtained for polystyrene particles show that the largest differences between hydrodynamic diameter and physical diameter occur in the case of small particles (up to 300 nm). This difference can arrive at over 100% (as in the case of 63 nm particles). In the case of larger particles (at least 600 nm), both sizes are comparable. In comparison with the results obtained by other researchers [53-55], mainly using the DLS method, our results indicated the existence of quite large differences between physical and measured diameter.

Table 3.2. Experimental data obtained as hydrodynamic diameter (d_h) for polystyrene particles of different nominal diameters suspended in deionized water.

Nominal diameter [nm]	Physical diameter [nm]	Hydrodynamic diameter [nm]
63±6	-	186±11
100±10	92±7	132±65
300±15	-	409±61
600±18	-	639±127
1000±50	959±53	960±149

By analysing the diffusion coefficients of polystyrene particles of various sizes (from 63 nm to 1000 nm), we were able to observe a remarkable relationship (Fig. 3.8). When decreasing the particle sizes, there was a well visible systematic decrease in their relative diffusion coefficients.
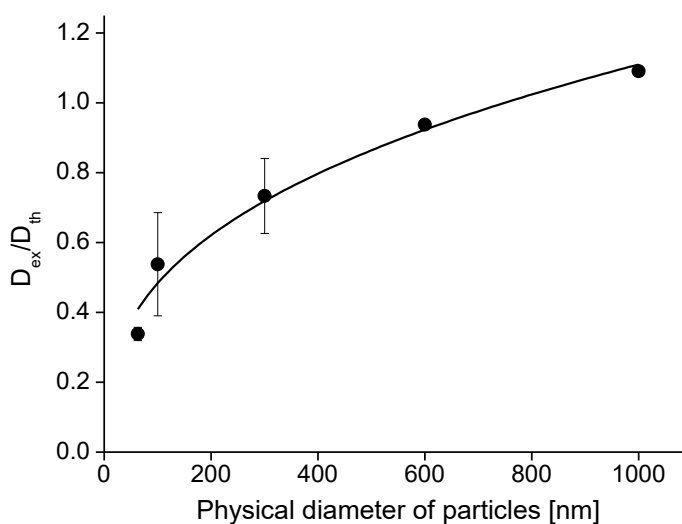
Figure 3.8. Dependence of the relative diffusion coefficient (ratio of experimental to theoretical diffusion coefficients) on the physical diameter for polystyrene particles suspended in deionized water.

This effect may be related to the thickness of the electric double layer (EDL), characteristic of any given medium, in which the tested particles were suspended. Its thickness (typically from 5 nm to 100 nm) is negligible for large-diameter particles, hence the value of the measured hydrodynamic diameter is close to the value of the physical diameter. By decreasing the particle size, the effect of the EDL increases,

and its thickness may even approach the particle diameter. To the best of our knowledge, this phenomenon has not been observed by other researchers and requires a more detailed analysis.

In an indirect way, low colloidal stability can cause a significant discrepancy between the hydrodynamic and physical diameters of the particles examined. The particles in most colloidal dispersions in aqueous media carry an electric charge. The stability of such dispersions is very sensitive to the addition of electrolytes. Surfaces can become electrically charged by the ionisation of surface groups [56]. For this reason, we investigated another particle type with a carboxylate-modified surface. Colloidal stability requires a minimum amount of surface charge. For particle materials containing acidic groups, their dissociation gives rise to a negatively charged surface. The negative charge causes a repulsive electrostatic force to counteract the inherent attractive van der Waals force [57]. Such polystyrene particles with a modified surface were suspended in deionized water and their hydrodynamic size was estimated using our tracking procedure. The experimental results averaged for nearly thousand series are shown in Table 3.3.

Table 3.3. Experimental data obtained for carboxylate-modified polystyrene particles suspended in deionized water. Nominal diameter versus hydrodynamic diameter.

Nominal diameter [nm]	Hydrodynamic diameter [nm]
95	845±430
199±1	1262±462
328±9	1457±930

As we may find, the measured hydrodynamic diameter is much higher than expected. In all three cases it is several times higher than the physical particle size. The simple explanation of particle agglomeration was ruled out. Observing the traces of individual particles, we were unable to detect any unexpected changes in their image spots or brightness. Therefore, since the results for this particle type, obtained in numerous repeated series, were significantly different every time from the expected values, we decided to discontinue this investigation. An interpretation of the observed phenomenon has yet to be formulated.

The third particle type studied, by tracking their trajectories, were gold particles. Due to the lack of a fluorescent factor in the structure of the particles, we recorded the light scattered on their surface. One of the shortcomings of this strategy is the fact that the air bubbles present in the solution also scatter light, which is then recorded and analysed as originating from the examined particles, thus negatively affecting the final result. The obtained results for gold particles are shown in Table 3.4. As can be seen,

the hydrodynamic diameter of the particles is up to 60% greater than their physical size.

Table 3.4. Experimental data obtained for gold nanoparticles suspended in deionized water. Physical versus hydrodynamic diameter.

Nominal diameter [nm]	Hydrodynamic diameter [nm]
40	65±19
60	102±17
108±7	162±33

By applying gold particles we expected to minimize the effects of the EDL layer or chemical deposits on their mobility. It seems that this is not the case. Similarly to polystyrene particles, the differences between physical and measured particle diameters are significant. Hence, to evaluate the correctness of our analysis performed with the particle tracking scripts developed at IPPT, 63 nm and 100 nm polystyrene particles and 100 nm gold particles suspended in water were tested using a commercially available NanoSight device (NanoSight Ltd., Minton Park, Amesbury, UK). The images recorded during the NanoSight measurement were extracted from the device and used by IPPT script for analysing Brownian motion. The results obtained by the commercial NanoSight software and our own software are compared in Fig. 3.9.
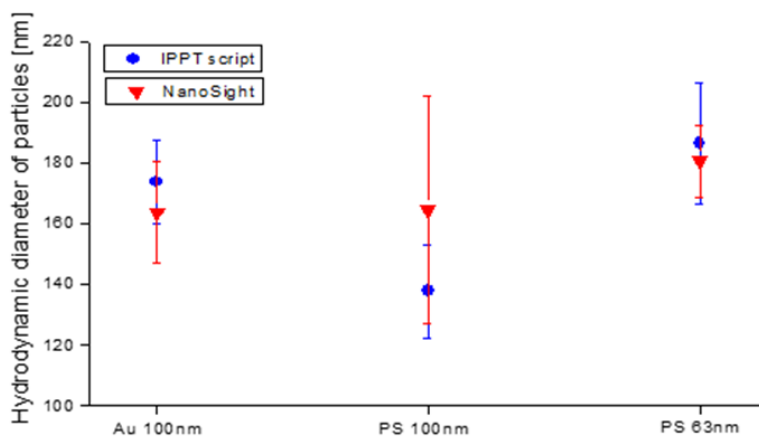

Figure 3.9. Comparison of hydrodynamic diameter results obtained for three particle types: Au100nm – 100 nm gold particles, PS100nm – 100 nm polystyrene particles, PS63nm – 63 nm polystyrene particles. Experiments performed in deionized water. Red dots – Nanosight results, blue dots – IPPT particle tracking scrip.

In the case of 100 nm gold particles and 63 nm polystyrene particles, the resulting hydrodynamic diameters partly overlap. For 100 nm polystyrene particles the differences are greater. Even taking into account relatively large standard deviations of the results obtained with both methods, the averaged hydrodynamic diameter obtained using NanoSight is almost 20% greater than that determined using IPPT script. Nevertheless, it can be concluded that the results obtained by the two methods used (IPPT and NanoSight scripts) overestimate the physical diameter of particles in a similar way (Fig. 3.10). It seems that only using a special calibration procedure and the correction factors included in the commercial software is it possible for users to obtain values corresponding to the physical diameter of the investigated colloids.

(a)   (b)

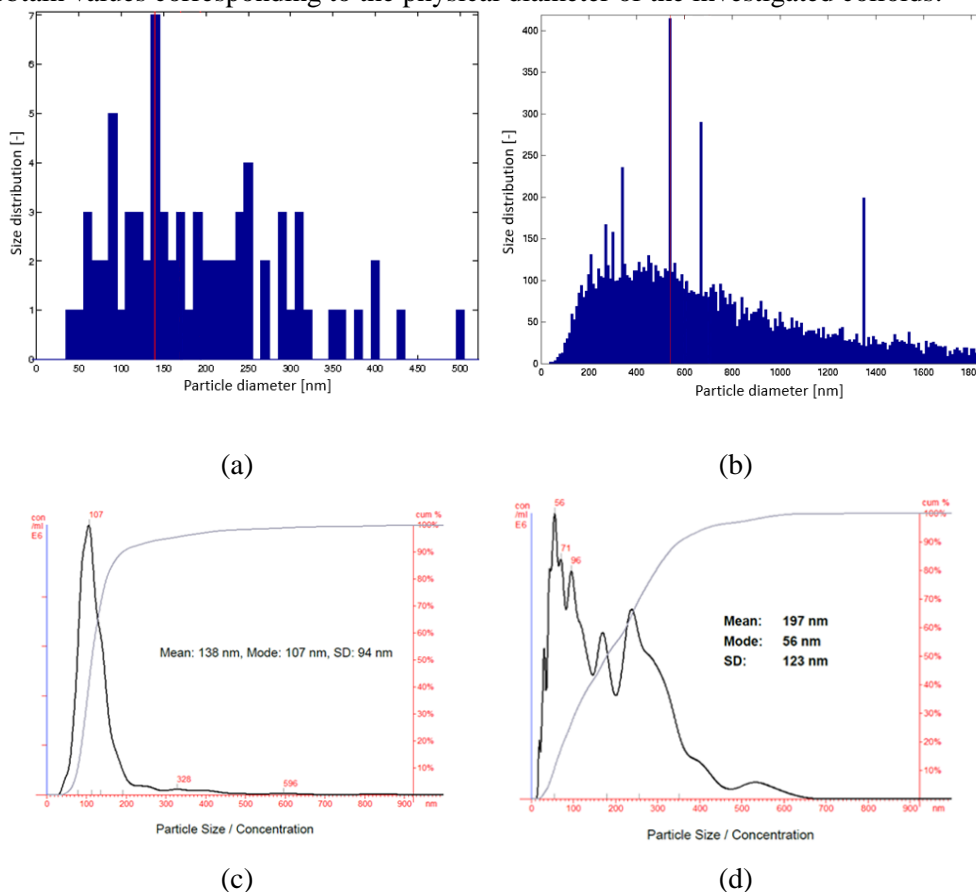(c)   (d)

Figure 3.10. The size distribution as a function of the particle diameter: (a) 100 nm polystyrene particles suspended in 10 mM KCl solution; (b) 600 nm polystyrene particles suspended in deionized water; (c) 100 nm polystyrene particles suspended in deionized water; (d) 63 nm polystyrene particles suspended in deionized water.

3.7.3. Ionic strength effect

To analyse the influence of the ionic strength of the medium on the value of the hydrodynamic diameter of particles, two types of solutions were prepared using a monovalent (KCl) and a divalent salt ($NiCl_2$). The range of salt concentrations ranged from 10^{-9} mM to 100 mM, depending on the type of salt. The results were based on thousands of experimental series conducted, each consisting of 500-1,000 camera frames.
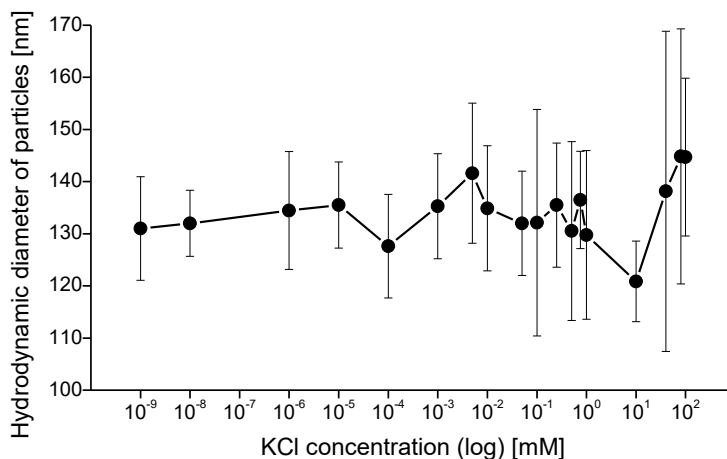

Figure 3.11. Hydrodynamic diameter of 100 nm polystyrene particles obtained at different concentrations of KCl.

Fig. 3.11 shows how the changed KCl concentration affects the measured hydrodynamic diameter. Looking at the chart, we can see that at a 10 mM salt concentration the EDL thickness reaches its minimum, while increasing again at a higher salt concentration. At this salt concentration the measured hydrodynamic diameter is closest to the physical diameter. This conclusion is confirmed by the guidelines of the International Standard on DLS, which state that the salt concentration suppresses the electrical double layer. Similar results have been obtained by other researchers [53]. Below the 10 mM salt concentration, hydrodynamic values are higher and fluctuate, while the corresponding hydrodynamic diameter is about 30% to 45% greater than the physical size of the tested particles.

On the basis of the results obtained by us, it is difficult to state clearly whether the hydrodynamic diameter decreases or increases with the increased salt concentration (ionic strength of the medium). Therefore we cannot confirm the results obtained by Xu [16], Chassahne [53], and Gittings [15], stating that the hydrodynamic diameter continuously decreases with increasing ionic strength.

We confirm, however, that when the concentration of a monovalent salt exceeds 10 mM, the hydrodynamic diameter significantly increases. This could be related to the formation of particle aggregations, the size of which increases when the salt concentration increases. In short, our investigation indicates that the hydrodynamic diameter of spherical nanoparticles depends strongly on the ionic strength of the liquid in which they are suspended.
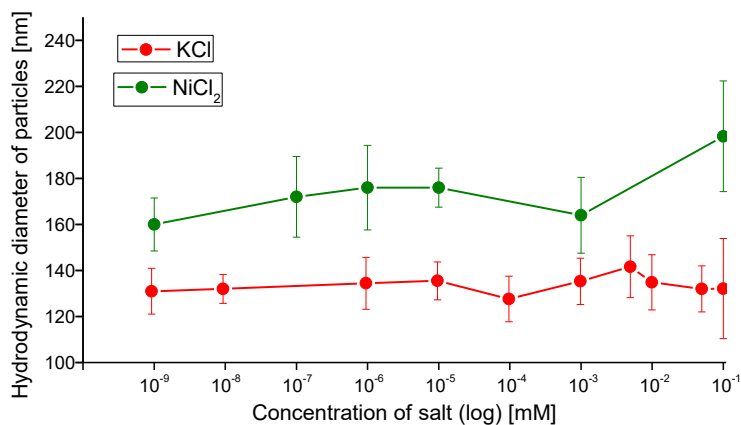

Figure 3.12. Hydrodynamic diameter of 100 nm polystyrene particles obtained at different concentrations of monovalent (KCl) and divalent (NiCl$_2$) solutions.

In the case of a divalent salt (NiCl$_2$), the situation is slightly different. Fig. 3.12 compares the impact of KCl and NiCl$_2$ salt concentrations on the hydrodynamic diameter of the analysed particles. At low salt concentrations, in both cases, waveforms are similar – the value of the hydrodynamic size does not change much with the increased ionic strength. The situation begins to change when the salt concentration reaches 10 mM. Unfortunately, in the case of NiCl$_2$, we were unable to obtain results for samples with a concentration higher than 10 mM, because we observed only large aggregates (even several times larger than single particles) over this value, thus hampering the performance of our particle tracking analysis. However we can guess that, as in the case of a monovalent salt, particles have a great tendency to group themselves in salt concentrations above 10 mM: a result also reported by other researchers [53] for this type of salt.

On the basis of the results we obtained, it is difficult to determine unequivocally in which divalent salt concentration the hydrodynamic particle size is closest to its physical value. According to the research presented by Chassagne [53], this value should be similar to that of a monovalent salt, and equal to around 10 mM. As already mentioned, the waveform of the curves look similar at lower concentrations of the salts tested (below 10 mM). However, it is clearly visible that in the case of a divalent

salt, the hydrodynamic diameter values obtained are higher than the corresponding values for a monovalent salt at the same concentrations. This is most likely related to the different packing of ions forming the double electric layer.

As in the case of the particles suspended in deionized water, polystyrene particles (63 nm and 100 nm) suspended in potassium chloride solution at various concentrations (0.1 mM, 1 mM, 10 mM) were examined using a commercially available device (NanoSight) to determine their hydrodynamic particle size. The images of the particles recorded over the course of NanoSight measurements were extracted and used to analyse the Brownian motion by IPPT script. The results obtained by these two programs are compared in Fig. 3.13 and Fig. 3.14.

Figure 3.13. Hydrodynamic diameter of 100 nm polystyrene particles as a function of the potassium chloride concentration evaluated by IPPT script (blue dots) and a commercial NanoSight instrument (red dots).

In the case of 100 nm particles, except for those suspended in the 1 mM KCl solution, the results are very similar. An even greater convergence of results was obtained for 63 nm particles. In both cases, the values obtained were higher (in the case of 63 nm particles a few times higher) than the physical particle size. On the basis of this analysis and a similar analysis for particles suspended in water, we can conclude that the program we developed for the analysis of Brownian motion makes it possible to determine the hydrodynamic diameter of nanoparticles with an accuracy comparable to that of commercially available devices.
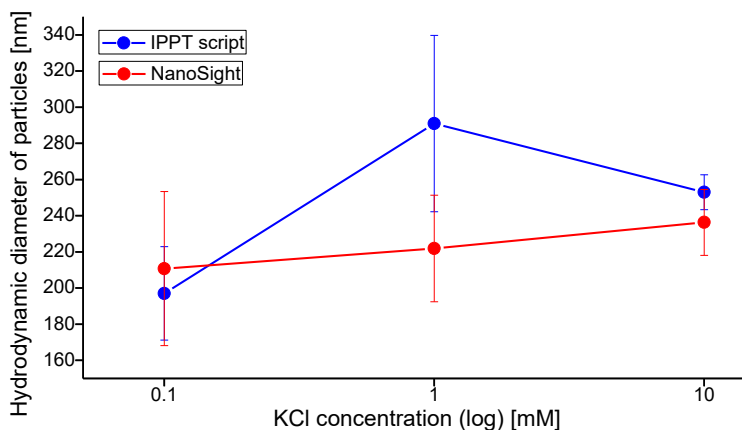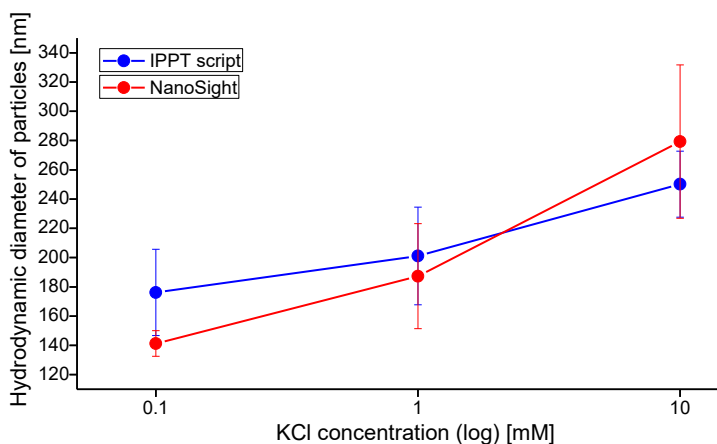
Figure 3.14. Hydrodynamic diameter of 63 nm polystyrene particles as a function of the potassium chloride concentration evaluated by IPPT script and the commercial NanoSight instrument.

3.7.4. Effect of ion size

It is worthwhile to remember that the interpretation of the diffusion coefficients (hydrodynamic diameter) measured for unknown biological particles may be very difficult, because it requires information on the ionic structure of the particle environment and details on the physical and chemical properties of an underlying biological system. For example, the difference in ionic sizes of solvent molecules can noticeably affect the measured mobility of nucleic acids [58].

For this reason an interesting factor was the effect exerted by the size of ions forming the medium on the size of the electrical double layer, and thus on the hydrodynamic size of the investigated particles. An experiment was therefore conducted in which particles were suspended in two different salt solutions with significantly different sizes of cations (KCl and LiCl). Polystyrene particles with a physical size of 100 nm were used for this experiment. The results obtained for a wide range of concentrations of both salts are shown in Fig. 3.15.
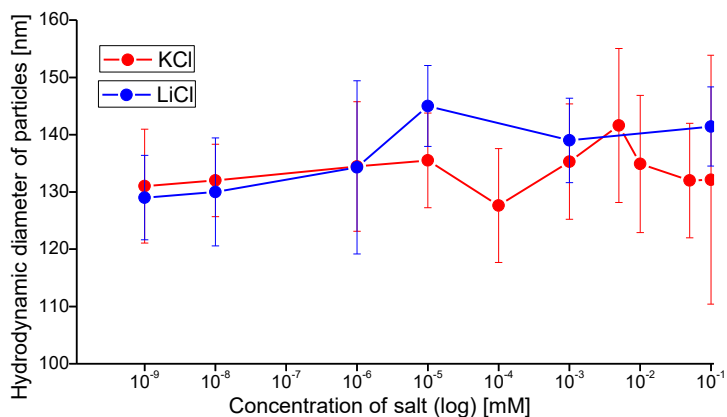
Figure 3.15. Hydrodynamic diameter of 100 nm polystyrene particles measured for different concentrations of KCl and LiCl solutions.

Since both salts have the same type of anion (Cl^-), the cation is the element that differentiates them. The Li^+ and K^+ ions have a radius of 0.06 nm and 0.133 nm, respectively. In addition to the radius of the ion the hydrated radius is also an important datum: 0.34 nm for Li^+, and 0.232 nm for K^+ [59]. The ion size translates into the thickness of the double electric layer surrounding the particle in a given medium, which in turn is reflected in the hydrodynamic diameter of the nanoparticle in question.

The two graphs in Fig. 3.15 have a very similar shape. Both have a clear maximum. The graph showing the results for KCl has a maximum of hydrodynamic size shifted towards a higher concentration (around $0.8 \ 10^{-2}$ mM). For LiCl, the maximum is 10^{-5} mM. At low salt concentrations, hydrodynamic diameter values were comparable. After reaching a salt concentration of 10^{-5} mM, the values of the hydrodynamic diameters obtained in both cases started to differ more and more. The higher salt concentration caused particles to be surrounded by a larger amount of ions. If the radius of these ions is larger, the thickness of the double electric layer also correspondingly increases. On the basis of the results obtained, we cannot confirm unambiguously that the effective thickness of the electrical double layer decreases as the counterion size decreases, as postulated by Bohinc et al. [60]. It is worthwhile to note that, according to the Poisson–Boltzmann theory, a continuously decreasing electrical double layer is observed as the surface charge density increases.

3.7.5. Wall effect

The optical tweezers system was used to analyse the interaction of 1 μm spherical particles, suspended in four different concentrations of KCl salt, with the microchannel wall (comp. Fig. 3.2). The experiment allowed us to demonstrate the possibility to obtain unperturbed measurements of the forces acting between the channel wall and the particles suspended near-by. Here, we limit our interest mainly to the electrostatic interactions of the ionic layer attached to the wall (EDL) and approaching it micro particle with its own EDL.

The experiment is conducted by stepwise approaching the trapped polystyrene particle in the wall at a constant 500 μm/s velocity (for single step equal 50 nm) and recording its displacement in the optical tweezers focus. This displacement was later calculated to be the force responsible for wall-particle interactions. In order to make the measurement as accurate as possible, first the calibration of the trap stiffness k (depending on the laser power $k(P)$) and detection system (quadrant photodiode response) were performed. The linear regression coefficients for the x and y axes were determined to be 0.0091 and 0.0093, respectively. So for 10% of the laser power, the trap stiffness was: $k_x = 0.091$ pN/nm and $k_y = 0.093$ pN/nm (comp. Fig. 3.16).
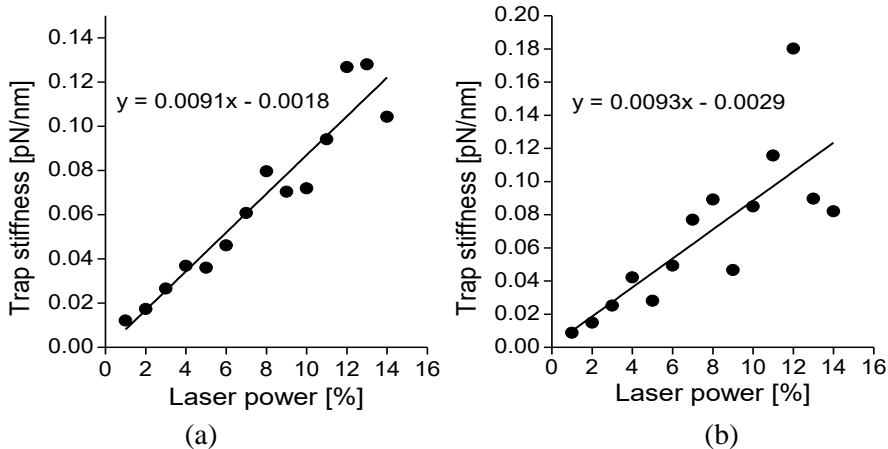
Figure 3.16. The stiffness of the optical trap in X (a) and Y (b) direction as a function of the trapping laser power.

As the output from the measurement we received values of signal power P [V] and the voltages (V_x and V_y, proportional to X and Y position of the incident beam) generated by the four photodiode amplifiers (V_1, V_2, V_3, V_4). This data were then further analysed using a special Matlab script to determine the force of particle-wall interaction , as well as effective viscosity change as a results of decreasing distance

between surface of the particle and the wall. For each measurements set, consisting of 1800 time points, we evaluated such parameters as:

- distance from the wall [nm], where 0 is the surface of the wall;
- mean force acting on particle [pN] in X (parallel) and Y (perpendicularly) direction to the wall;
- mean X and Y position of particle in trap [nm];
- mean square displacement amplitude [nm^2], calculated separately for two half of peak-to-peak distance;
- mean quadrant photodiode laser power [V] – parameter important for controlling the stability of the laser power, and thus the stability of the measurement system.

For further analysis a component perpendicular to the wall (Y) was used. The parallel component (X) was burdened with an additional error resulting from the fact that displacements are not exactly parallel to the surface of the wall. This component is very sensitive to the roughness of the wall surface and the imperfection of setting the trap in relation to the surface plane.

The results of the measurements obtained for X and Y force acting on particle are shown in Fig. 3.17. The differences between both measured force components X and Y are worth noting that strongly depends on salt concentration, with the smallest differences in the case of 1 mM KCl concentration (Fig. 3.17 (c)). The experimental runs started when particles were relatively far from the wall (about 3-8 particle diameters). At such a distance both electrostatic and molecular forces between the particle and the wall should be very small. Nevertheless, even at such a distance we recorded non-negligible particle displacements from the trap centre. The values of the particle-wall interaction forces were in the range of -8.0 pN to 7.0 pN. Depending on the salt concentration, the shapes of the force curves appeared different. At low salt concentration (from 0.1 mM to 10 mM) the interacting forces (in the Y direction) change with the distance from the wall uniformly without sudden jumps. Sudden jumps in the curves of force appear at a distance below 1500 nm from the wall. These irregularities of the force curves are shifting towards smaller distances from the wall as the salt concentration increases. Surprisingly, with the increased KCl concentration to 100 mM (Fig. 3.17 (e)), the waveform of graphs becomes more and more irregular. The smallest changes of force with the decreasing distance of the particle from the wall were observed when the particle was suspended in deionized water (Fig. 3.17 (a)). It is evidently difficult to see a clear, uniform relationship between the salt concentration and the levels of force recorded close to the wall. This puzzling behaviour recalls the observations obtained from the Brownian mobility, where several up-and-down variations in the ionic interactions are present (comp. Fig. 3.11).

(a)

(b)

(c)

(d)

(e)

Figure 3.17. The force of the interaction between 1 μm polystyrene particle and PDMS wall in deionized water (a) and different KCl concentrations: (b) 0.1 mM; (c) 1 mM; (d) 10 mM; (e) 100 mM.

Fig. 3.18 shows normalized force for particles in deionized water and three KCl concentrations. The obtained values of force components were normalized firstly to the value of force at the infinity (set as 0) and next normalized to unity, which corresponded to the highest particle-wall interaction force for all investigated salt

concentrations (in this case equal to 0.135 pN, for 1 mM KCl). The data obtained for 100 mM KCl concentration appeared difficult to be correctly interpreted for us.
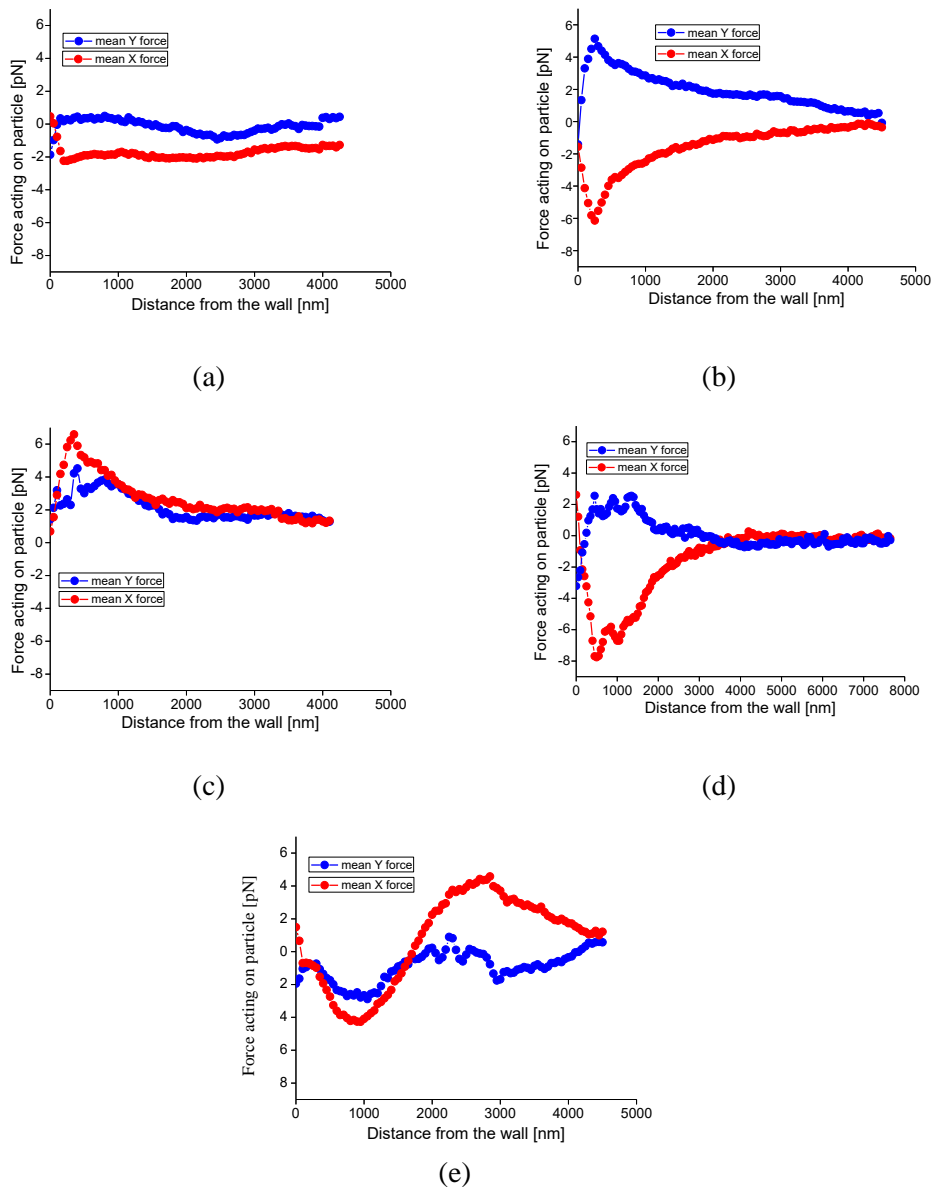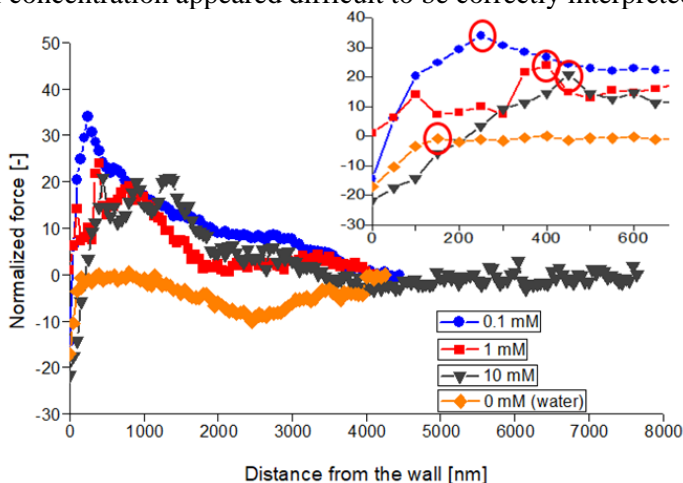

Figure 3.18. The force of the interaction between 1 μm polystyrene particle and PDMS wall in deionized water and in different KCl concentration.

For low concentrations, independently of the medium used in which the test particle was suspended, the force values only slightly deviate from the neutral value equal to 0, in the initial stage of observation (above 4 μm from the wall). As we approach the wall, the values of the forces recovered increase tendency (repulsion a particle-wall), obtaining a maximum value in the range from 100 to 500 nm from the wall. The location of this maximum is clearly dependent on the salt concentration – it is closer to the wall when the ionic strength of the medium is lower. It is 150 nm, 250 nm, 400 nm and 450 nm for deionized water, 0.1 mM, 1 mM and 10 mM KCl, respectively (Fig. 3.18, the top right section of the chart, inside red circles). This may be probably related to the thickness of the double electrical layer focused around the analysed particle and the ionic layer adjacent to the wall to which we approach the particle. We could predict that the higher the ionic strength, the stronger the layers are and then more strongly they interact. However, after crossing a certain distance limit, we observe a decrease in the particle-wall interaction force associated with the presence of attractive forces. The observed phenomenon is contrary to the DLVO theory. However, Larsen and Grier made similar observations to ours [61] and showed that the effective pair potential between two like-charged polystyrene spheres in water electrolyte includes a long-range attraction, when they put this spheres near a charged glass wall. This phenomenon is particularly visible at low salt concentration and large screening lengths. The classical DVLO theory neglects any effect that a charged sphere has on the screening ion density in the vicinity of other spheres [62].

If we look at the level of the obtained maximum of repulsive interactions (Fig. 3.18, the top right section of the chart), then we also observe its dependence with the concentration of KCl salt. The highest value of the repulsive force between the particle and the wall is observed at the lowest KCl concentration (0.1 mM). This force decreases as the concentration of ionic strength increases. For comparison, the results of Assemi et al. [63] with regard to force measurements between carboxylate-modified polystyrene sphere and glass in different NaCl concentrations using an atomic force microscope showed that the maximum repulsive force decreases as the salt concentration increases. A similar relationship was also observed in our previous investigations with KCl salts and interaction between two particles [64].

As we may see in Fig. 3.18 the lowest force values were obtained for the particle suspended in deionized water. In a distance not greater than the particle diameter (1 μm) it was close to 0, then after reaching a small maximum, it dropped to a relative value of - 17 (equal to -2.3 pN).

The data collected during the measurement also allowed to study how the relative viscosity (interpreted as the inverse of diffusion change and determined from the amplitude of vibrations) changes as the particle approaches the wall surface. The obtained effective viscosity values (component Y) were normalized to the value of viscosity in the infinity (set as 1).

We show that the relative viscosity increases with the decrease of the ionic strength of the medium. As seen in Fig. 3.19, at a distance above about 1-1.5 μm from the wall, we observe a significant decrease of the apparent viscosity as particle approaches the wall. Below this distance there is an increase, and then a sudden jump of viscosity associated with the touch of the particle to the wall, and thus the inhibition of the particle vibrations.
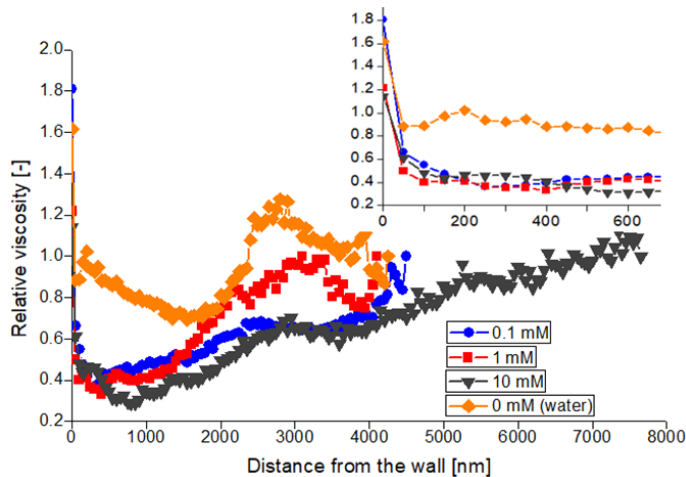

Figure 3.19. The effective viscosity as a function of distance between wall and approaching to it particle, for water and different concentrations of salt.

The present preliminary results show that using Optical Tweezers opens possibilities for detailed studies of particle-wall hydrodynamic interactions with unavailable ever before femtonewton accuracy and spatial resolution of tens of nanometer. What is also very important, is that during one such measurement we can collect information about three parameters: (i) force interaction between objects; (ii) the apparent liquid viscosity, indicated by damping of Brownian fluctuations; (iii) the flow resistance, when we collect data also when the particle moves towards the wall.

3.7.6. Lateral migration of spherical particle

The cross-flow migration of spheroidal objects such as particles, droplets, and red blood cells has been the subject of numerous studies [65-70]. This work compares the results concerning the migration of spherical particles and our experimental results obtained in the oscillating flow.

Before the experimental runs started, we observed that the distribution of the investigated particles across the whole plane of observation was rather uniform, except in the wall region (Fig. 3.20).
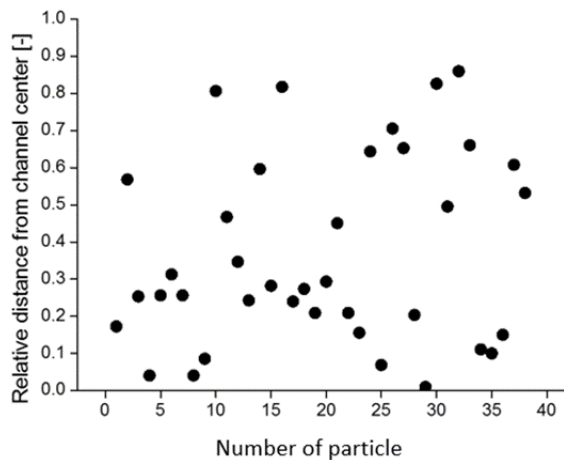
Figure 3.20. Initial position of each examined particle in the microchannel; the relative distance [0,1] denotes the microchannel centre and the wall, respectively.

During each experimental run the position of the observed fluorescent particles conveyed by the oscillating flow was recorded and analysed. Depending on the particle's initial location, its cross-flow trajectory changed, and the particles tended to move either to the side wall or in the opposite direction, into the channel axis.

(a)   (b)
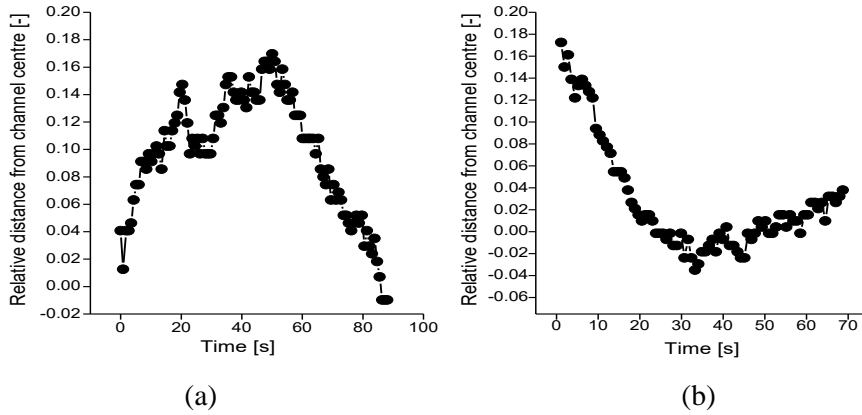
Figure 3.21. Cross-flow migration of 1 μm spherical particles in the oscillatory flow: (a) maximum flow velocity V_{max} = 259 μm/s; Reynolds number Re = 0.063; relative migration velocity V_r = 7.7 10^{-6}; (b) V_{max} = 255 μm/s; Re = 0.062; V_r = 2.2 10^{-6}.

When the particle's initial position is relatively far from the channel centre, the migration direction is clearly into the flow axis (comp. Fig. 3.21 (a)). After approaching the flow axis, the particle position fluctuates around this axis. For the particle starting its track already close to the channel axis, its final (equilibrium) position appears to continue fluctuating across the channel axis (comp. Fig. 3.21 (b)).

(a)   (b)
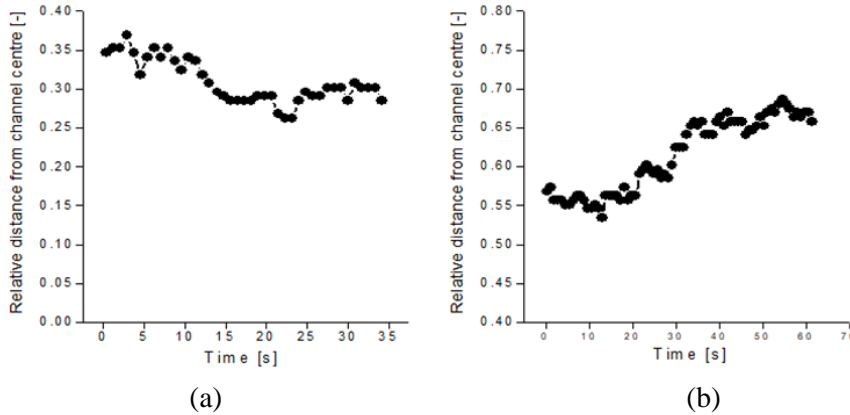
Figure 3.22. Cross-flow migration of 1 μm spherical particles in the oscillatory flow: (a) maximum flow velocity V_{max} = 252 μm/s; Reynolds number Re = 0.061; relative migration velocity V_r = 7.2 10^{-6}; (b) V_{max} = 228 μm/s; Re = 0.060; V_r = 6.5 10^{-6}.

Fig. 3.22 shows the cross flow migration of the particles located closer to the side wall. At still relatively great distances from the channel wall (Fig. 3.22 (a)), particles slowly move into the flow axis. Closer to the wall, however (Fig. 3.22 (b)), particles seem to reach a weak equilibrium position, being close to the theoretical value reported in the literature ($\underline{x}$ = 0.6).

When comparing present observations with the reported data obtained for steady, creeping flow [70], some important differences can be seen. Our particles are Brownian particles, the cross-flow velocity magnitude is comparable in magnitude with the stochastic jumps of a Brownian particle. For the oscillatory flow, this effect is magnified at periodically repeated changes in the flow direction. When the flow ceases out before changing its direction, any stochastic change in the particle position creates its new cross-flow trajectory, to be continued during the next flow oscillation period. This effect is especially evident close to the channel axis, where the amplitude of the sudden changes in the flow direction is greatest. This may induce the strong fluctuation observed of the particle position across the flow axis. We do not see such strong fluctuations at greater distances from the centre line (more than 0.2). In any case, it is worthwhile to note that even in the case of low Reynolds number flows, where one could expect the reversibility of particle tracks, there is obviously a net cross-flow particle migration.

Undoubtedly, this particle migration is influenced by many factors. To see how the flow velocity determines the direction of migration, we tested different values of the maximum velocity of the oscillating flow. The first group was characterized by an average maximum flow velocity of 251 μm/s (Fig. 3.23 (a)), while that of the second group was 90 μm/s (Fig. 3.23 (b)). Fig. 3.23 shows the frequency distribution of 1 μm polystyrene particles across the microchannel width, before the application of a hydrodynamic force (grey bars) and after around 40 oscillatory cycles (dashed-contour bars).

(a)   (b)
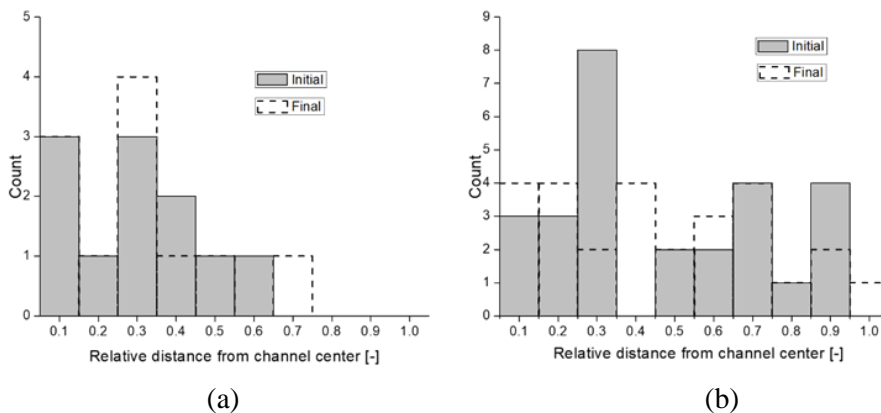
Figure 3.23. Lateral migration of spheroidal polystyrene 1 μm particles depending on flow rate: (a) average V_{max} = 251 μm/s; (b) average V_{max} = 90 μm/s.

As we can see, the results are inconclusive, even though the influence of the flow velocity on the location of the equilibrium position is small. Both oscillating flow and Brownian diffusion seem to be similar at the equilibrium position of particles.

According to the low Reynolds number model given by Ho and Leal [70] also confirmed by other researchers [71-73], this equilibrium for steady flow is close to $\underline{x} = 0.6$.

An interesting factor is the magnitude of the averaged lateral migration velocity U_r. This value referring to the maximum amplitude of the flow velocity, marked as V_r, is between $1.12 \ 10^{-6}$ and $3.48 \ 10^{-5}$. We compared this lateral migration velocity with the results calculated by Ho and Leal [70] for spherical particles in a two-dimensional Poiseuille flow. For the corresponding two-dimensional steady flow, the relative migration velocity predicted by the model is in the range of $7.40 \ 10^{-7}$ to $2.02 \ 10^{-4}$. The obtained values of experimental lateral migration velocity and those from Ho and Leal equation are not completely similar. The results obtained from the Ho and Leal model have a wider range of values. The lowest values obtained are almost three orders of magnitude lower than in the experiment described. It must be remembered, however, that the equation used in the model refers to the translational motion, whereas in our case we are referring to the oscillatory motion. Secondly, the model practically ignores any inertial effects. This is not the case of our oscillatory flow, where the velocity direction changes periodically at a relatively high frequency. The relatively high values of the migration velocity indicate that, for the investigated range of experimental conditions, the oscillating flow may be treated as the efficient method for sorting particles or directing them into desired locations in capillaries.

Mobility of highly deformable hydrogel nanofilaments

4.1. Morphology of core-shell nanofibres and hydrogel nanofilaments

The morphology of collected core-shell nanofibres was tested by SEM (Nova NanoSEM 450 model, FEI, USA). Before the analysis, nanofibres were sputtered with gold (using a Polaron model SC7620 mini sputter coater, Quorum Technologies Ltd., Ashford, UK). ImageJ [74] software was used for the calculation of the nanofibre average diameter using about 100 manually selected nanofibres. The hydrogel nanofilaments extracted from nanofibres were examined by fluorescent microscopy and AFM. AFM (Ntegra, NT-MDT), equipped with a closed liquid cell. A rectangular silicon cantilever (CSG01, NT-MDT) was used to evaluate sample surface topography. The mechanical resonance and cantilever spring constant were in the range of 4-17 kHz and 0.003–0.13 N/m, respectively. Measurements were carried out in aqueous solutions at 25°C, in the contact mode.

4.2. Experiments on diffusion and channel flow

4.2.1. Brownian motion experiment

Extracted from nanofibres, the suspension of hydrogel nanofilaments in DMF solution was prepared and placed between two sealed microscope slides, at a distance of about 50 µm from each other (Fig. 4.1).

The Brownian motion of nanofilaments was recorded by an electronic camera (C9100-2, Hamamatsu, Japan) coupled with a Leica AM TIRF MC epifluorescence microscope. For observing single nanofilaments, a 63x 0.70 NA objective lens were used. The sampling was at approximately 10 frames per second, with 1,000 frames recorded in one experimental sequence.
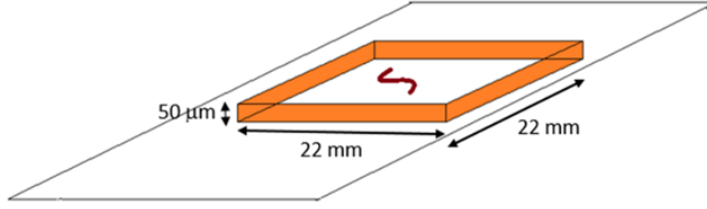
Figure 4.1. Scheme of the experimental microchannel.

A Matlab [75] script was developed to evaluate filament displacements; it was used to locate the filament centre in frame coordinates [*x(t)*; *y(t)*], as well as the orientation of filaments *θ(t)* with respect to the *x* axis of the frame. The rotation matrix was used to calculate the incremental displacement of every analysed nanofilament. This displacement was observed between two time steps in the object frame (δa_n; δb_n) longitudinally and perpendicularly to the long axis of the fibre. Resulting displacements were evaluated from the laboratory frame incremental displacement (δx_n, δy_n) using a rotation matrix [76]:

$$\begin{pmatrix} \delta a_n \\ \delta b_n \end{pmatrix} = \begin{pmatrix} cos\theta_n & sin\theta_n \\ -sin\theta_n & cos\theta_n \end{pmatrix} \begin{pmatrix} \delta x_n \\ \delta y_n \end{pmatrix} \tag{4.1}$$

To obtain translational diffusion coefficients along the *a* and *b* axes of the fibre, long sequences of images (~1000) were evaluated. Diffusion coefficients were calculated using the mean square displacement related to the known time interval *t* between frames [76]:

$$\langle [\Delta a(t)]^2 \rangle = 2D_a t \tag{4.2}$$

$$\langle [\Delta b(t)]^2 \rangle = 2D_b t \tag{4.3}$$

To calculate the rotational diffusion coefficient, the mean square angular displacement was evaluated [76]:

$$\langle [\Delta \theta(t)]^2 \rangle = 2D_\theta t \tag{4.4}$$

We compared the results of our experimental diffusion coefficients of short filaments and the theoretical diffusion coefficients obtained for long, thin spheroids, where *a* >> *b* [21, 76]:

$$D_a = \frac{k_b T [ln\left(\frac{L}{R}\right) - 0.5)]}{2\pi \eta L} \tag{4.5}$$

$$D_b = \frac{k_b T [ln\left(\frac{L}{R}\right) - 0.5]}{4\pi \eta L} \tag{4.6}$$

$$D_\theta = \frac{3k_bT[ln\left(\frac{L}{R}\right) - 0.5]}{\pi \eta L^3} \tag{4.7}$$

where: k_b – Boltzmann's constant, T – absolute temperature, η – the water viscosity, and R and L – filaments' radius and length.

4.2.2. Filament flexibility measurements

4.2.2.1. Atomic Force Microscopy nanoindentation method

AFM nanoindentation analysis is a helpful method for directly measuring the Young modulus of hydrogel nanofilaments immersed in water. Stiffness was measured at 302 K in a closed liquid cell. This procedure was necessary in order to keep the hydrogel hydrated, minimise the thermal drift influence, and prevent contamination. We used a silicon nitride cantilever (CSG01, NT-MDT) with nominal 6 nm tip radius. The cantilever with spring constant equal to 0.040 N/m was calibrated by the thermal method [77]. We selected and then analysed different zones of a few hydrogel nanofilaments collecting several series of force curves (Fig. 4.2) [77]. By fitting the Hertz model into the collected data, the filament Young's modulus was calculated using the following equation:

$$E = E_r\left(1 - v_f^2\right) \tag{4.8}$$

where v_f is the Poisson's ratio of hydrogel and E_r is relative elastic modulus. The swollen hydrogel material v_f may be considered similar to rubber-like materials, which have a Poisson ratio of around 0.5 [78]. The relative elastic modulus is evaluated using the following formula [77]:

$$E_r = \sqrt{\frac{9P^2}{16R_e\delta^3}} \tag{4.9}$$

where P is the force applied, δ is the indentation depth, and R_e is the equivalent radius for a spherical intender, defined as [77]:

$$R_e = \sqrt{\frac{R_t^2R}{R_t + R}} \tag{4.10}$$

where R_t is the tip radius of curvature and R is the radius of the nanofilament.
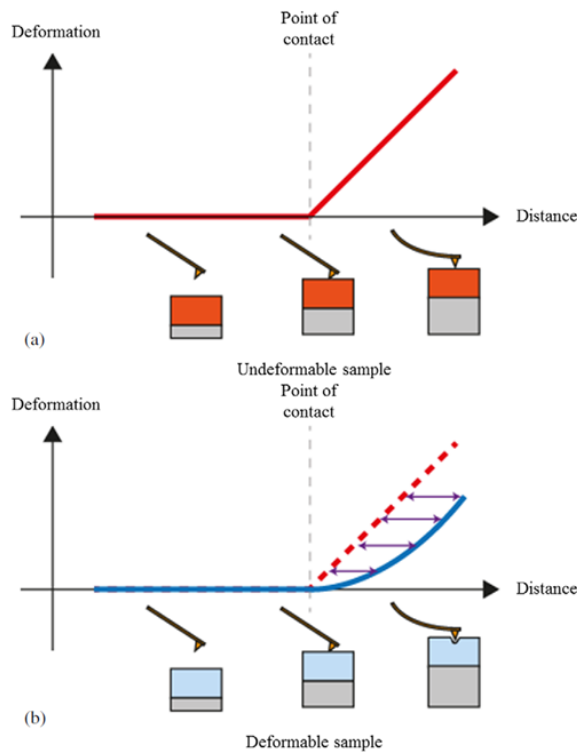
Figure 4.2. Scheme of force-distance evaluation for AFM indentation of a hard sample (a) and a soft sample (b). The curve of indentation can be obtained by subtracting one curve from the other, as indicated by the violet arrows [79].

The method has its limitations. It may be expected that when a surface is pushed by a conventional AFM probe, the cantilever bending and applied force will be linearly dependent. This is true when the sample is hard and the probe does not deform it.

4.2.2.2. Thermal fluctuation method

The second method used to evaluate the mechanical properties of flexible nanofilaments is based on the observation of the shape dynamics due to their thermal fluctuations [80-82]. Using this method, the mechanical properties of polymers such as microtubules or DNA can be evaluated in terms of persistence length. This method is based on the analysis of the two-dimensional cosine correlation of the tangent angle (Θ) along segments (s) of the long object with a contour length L. It uses the fitting function:

$$cos\,\Theta(s) = \; < cos[\Theta(s) - \; \Theta(0)] > = e^{-L/2L_p} \qquad (4.11)$$

where $\Theta(0)$ is an initial reference angle. The symmetry of cosine function ($\pm\,\Theta(s)$ - $\Theta(0)$) is not convenient for fitting it to the experimental data. Thus, for the evaluation of the persistence length, data are fitted to an exponential function [83-85].

In the procedure for determining the persistence length, the prepared hydrogel nanofilaments were injected into a chamber formed by microscope slides sealed with a grease and observed using a fluorescent microscope. Only nanofilaments longer than 1 μm were analysed. The images of the nanofilaments to be analysed were prepared according to the recommendations of Ott et al. [81, 83]. Briefly, grayscale images were cleaned from short objects and smoothed. Nanofilament positions were enhanced and the conversion to binary images was performed. A Matlab script was written to connect the filament structure gaps caused by the low fluorescence intensity and to process these images. About 500 to 700 images of skeletonised filaments were analysed with the cosine correlation method implemented in Matlab. For the calculation of the flexural Young modulus E below equation was used:

$$L_p = \frac{\kappa}{k_b T} = \frac{EI}{k_b T} \qquad (4.12)$$

where $I = \pi R^4/4$. T is the absolute temperature, k_b is the Boltzmann's constant, and R is the radius of the filament.

To verify our methodology, several of our calculation results were compared with the persistence length obtained using the software developed by the De La Cruz group [83].

4.2.2.3. Hydrodynamic interactions method

The last method we used to determine the filament Young modulus is based on the interaction of the fluid flow with the filament fixed to the channel wall at one end. This technique is based on the analysis of the nanofilament bending as a result of the fluid force exerted on a deformable cylinder [82]. As a first step, fibres were electrospun on a piece of PDMS with an elongated structure of 5 mm width and 3 mm depth. We were able to obtain a perpendicular arrangement of the fibres relative to the wall of this structure. Two identical pieces of PDMS (one with and one without fibres) were then glued together to form the channel. The attached fibres were placed in the middle of the channel. Then the PDMS channel was placed under an epifluorescence microscope and connected at one end by a PTFE tube to a syringe pump (neMESYS, Cetoni GmbH). After gradually filling the channel with DMF solvent, nanofibre shells dissolved, revealing hydrogel filaments in the form of short rods. After initiating the

fluid flow, the hydrogel rod started to bend due to exerted hydrodynamic drag force. Once the flow stopped, the bending elasticity of the nanorod returned it to its original position. The evaluation of its deformation rate and exerted hydrodynamic forces allowed us determine the elastic properties of the rod. To minimise the uncertainties of estimating the magnitude of very low flow rates applied, the nanorod elasticity was determined during the return phase of the bending process. Hence, the rod displacement in time (velocity) determined the hydrodynamic drag balancing the elastic force of returning it back to the initial position (Fig. 4.3).

The balance of elasticity force and hydrodynamic drag force is equal:

$$F_e - F_d = m\, a_c \qquad (4.13)$$

where a_c and m are the acceleration and mass of the rod, respectively. Elasticity force is described by:

$$F_e = k_e\, \Delta x \qquad (4.14)$$

where: k_e – elasticity constant, and Δx – displacement. Generally speaking, the hydrodynamic drag force for the rod moving with velocity V relative to a fluid is given by:

$$F_d = C_D \frac{\rho V^2}{2} A_s \qquad (4.15)$$

where ρ – density of the fluid, V – speed of the filament relative to the fluid velocity, A_s – cross-section area of the rod, and C_D – drag coefficient for the rod.
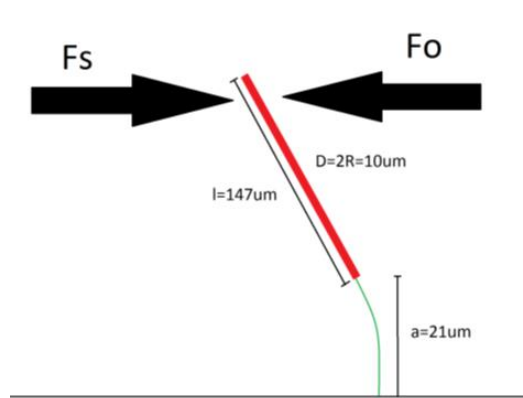

Figure 4.3. Scheme presenting forces acting on the deformed hydrogel rod.

At a low Reynolds number regime, neglecting inertial effects, the hydrodynamic drag force is given by the simplified formula obtained for an elongated ellipsoidal obstacle, characterized by a radius R and length L [20]:

4.2 Experiments on diffusion and channel flow

$$F_d = \frac{4\pi\eta VL}{ln(L/R)} \tag{4.16}$$

where η is fluid viscosity.

Recording the speed of the returning rod attached to the channel wall, this formula enabled us to calculate the bending Young modulus of the hydrogel filament.

4.2.3. Channel flow analysis

For experiments with hydrogel nanofilaments in a flow, the same measurement setup as for the lateral migration of spherical particles was used (Chapter 3.5). Before each experimental run, a suspension of fluorescently labelled hydrogel nanofilaments was manually injected into the PDMS microchannel. Then the solution was subjected to an oscillatory shear flow using a pulsatile pump. Very short hydrogel debris ($L \sim 1$ μm), always present in the solution after the removal of the polymer shell, were used to estimate the local flow velocity around the nanofilaments. The maximum amplitude of the flow velocity (V_{max}) used during the experiments varied between 0.05 mm/s and 0.95 mm/s, while the range of the forcing frequency was between 0.12 Hz and 0.64 Hz. We considered a flow of Newtonian liquid through the microchannel with a rectangular cross-section. The flow was characterized by a small Reynolds number ($Re = V_{max}\,W\rho/\eta$) based on the channel width W. It varied from 0.01 to 0.18.

Nanofilaments were observed by using an inverted epifluorescence microscope (Leica AM TIRF MC) with a 20x/0.40 NA microscopic lens, and an appropriate set of filters for fluorescence imaging. As a source for fluorescence excitation, a mercury lamp (Leica EL6000) was used. The high-gain EM-CCD camera (C9100-2, Hamamatsu) was used to record nanofilament displacements, with a typical frame rate of 10 Hz. Each series consisted of 500 to 2,000 individual images. Nanofilaments were observed and recorded at 15 mm from the channel inlet within the 500 µm-long and 200 µm-wide section of the horizontal central plane located 30 µm above the bottom wall of the microchannel. If filaments were above or below the focal plane of the microscope they were not used in further analyses. Moreover, filaments were also excluded from the analysis if they clearly changed their contour length during an experimental run, i.e. when its variations exceeded 10%. Such apparent length changes indicated their out-of-plane shape deformations. All experiments were conducted by using the microscope environmental chamber at a stable temperature of 302 K. The working liquid density ρ and dynamic viscosity η measured at that temperature were 984 kg/m^3 and 7.5 10-4 kg m/s, respectively.

4.3.   Filament mechanical properties evaluation

The hydrogel nanofilaments obtained by the electrospinning technique had a typical contour length in the range from 1 μm to over 500 μm. In this experiment, we used nanofilaments with a contour length of 20 μm to 90 μm, which was evaluated using microscopic images and the ImageJ program [74]. The long sequences of filament images taken in the channel before the oscillating flow started provided the opportunity to obtain their average value of contour length along with the corresponding persistence length.

Before each experimental run, the geometry of the selected nanofilaments was evaluated. For this purpose, the selected object was conveyed by a micro-pump into the observation area of the microscope and its fluorescent images were analysed in stop-flow conditions with the help of the image processing Matlab software.

The dynamics of the filaments carried by the flow depends both on their mechanical properties (flexural and extensional modules, E, E_x) and on their geometry (diameter and contour length). The mechanical properties of a hydrogel material depend on its composition. As described before, the fabricated nanomaterials were characterized by nanoindentation, hydrodynamic bending, and thermal fluctuation analysis. The obtained mean value of the flexural Young modulus (E) was equal to 2 kPa. Its approximate result was obtained by the method of the direct bending of the sample filament in a shear flow (hydrodynamic interaction method) and the AFM indentation method. The accuracy of this estimation depends significantly on the proper evaluation of the filament geometry.

The extensional Young modulus (E_x) was obtained from macro-scale stretching experiments with a hydrogel beam of 4 mm diameter and 1.8 cm length. The asymptotic value of E_x obtained at the limit of small stretching forces was equal to 20 kPa. This value appears to be an order of magnitude higher than flexural rigidity, thus confirming the relatively high extensional stiffness of our filaments.

Young modulus, once established for the sample material, is used to obtain the filament diameter d from the evaluated persistence length L_p, according to the formula:

$$E = (64k_b T L_p)/(\pi d^4) \tag{4.17}$$

This procedure provides better results than the analysis of microscopic images. Determined that way diameter of filaments used in the experiment are in the range of 110 nm to 180 nm, which is in agreement with the AFM measurements of single samples.

 For analysis of the filament deformations, we determined two non-dimensional parameters to characterize the mechanical properties of our hydrogel filaments:

4.3 Filament mechanical properties evaluation

relative flexural stiffness (*A*), and relative extensional (Hookonean) stiffness (*K*). Relative flexural stiffness describes the ratio of filament bending stiffness related to the hydrodynamic force. A high value of *A* indicates a stiffer (less flexible) filament. For *A* = 0, the fibre bends freely without recovering its initial shape. The definition used to evaluate the relative flexural stiffness is [93]:

$$A = Ed/(32\,\eta V_{max}) \tag{4.18}$$

where: V_{max} is the absolute maximum flow velocity in the centre of the microchannel, and η is the dynamic viscosity of the carrier fluid.

The relative extensional stiffness describes the ratio of the extensional filament deformation force related to the hydrodynamic force of the flow amplitude. It is defined as:

$$K = E_x d^2/(4L\eta V_{max}) \tag{4.19}$$

For our highly deformable objects suspended in a fluid flow, one of the significant degrees of deformational freedom is bending/buckling. This behaviour is due to the flow-induced viscous forces characterized by the local flow shear rate, and to the thermal fluctuations characterized by persistence length. Following the approach of Kanstler and Goldstein [86], and Li et al. [87], we introduced two additional non-dimensional numbers characterizing the dynamics of the analysed filaments. The first parameter, Sperm number (*Sp*), characterizes the relative magnitudes of viscous and elastic forces for deformable objects conveyed by a steady flow [88]. It is given as:

$$Sp = 32\pi\eta V_{max}\underline{L}^4/(EW) \tag{4.20}$$

where: *W* is the channel width, and $\underline{L}$ is the length-to-diameter ratio (= *L/d*).

For *Sp* ≤ 1, thermal modes dominate over the flow-induced viscous friction, and a flexible filament oscillates transversely and symmetrically. For *Sp* >>1, thermal bending shape fluctuations are damped by the flow-induced viscous stresses, while the free filament ends are motionless [89]. We must remember, however, that at each oscillating cycle there is a short dwell time. At that moment, thermal fluctuations are dominant and could slightly modify the position and deformation of tangled filaments. For the analysed configuration this effect appears to be residual, as the elastic relaxation time of filaments is over 100 s, much longer then the stopped flow time.

As the position of the filaments conveyed by the flow is perturbed by thermal fluctuations, the significance of this effect can be evaluated by correlating the flow-induced convection time to the characteristic time of Brownian diffusion. The latter depends on the shape, configuration, and local deformations of filaments, something that is generally difficult or impossible to describe by a simple formula. Hence, we estimated the diffusion relaxation time from our experimental data collected for the

measured translational displacements. The corresponding Peclet number (*Pe*) becomes:

$$Pe = LV_{max}/D \tag{4.21}$$

where *D* is the longitudinal diffusion.

For Peclet numbers lower than 1, we have to assume the dominating Brownian diffusion over the flow-induced longitudinal translation of the filament. However, for typical values in our experiments, with the Peclet number over 10^2, we may conclude that the Brownian diffusion has negligible effects, again except the short time intervals of stop flow of oscillating periods.

4.4. Orientation, elongation, and bending analysis methods

Because of the large number of degrees of freedom, the problem of characterizing the mobility of flexible objects, such as nanofilaments or long molecular chains, can be solved only on a statistical basis. It is not only that the translational and rotational motions of objects must be analysed. The main response to thermal fluctuations and shear stresses is transformed into a multifunctional shape variation. There is no single method of characterizing the dynamics of such objects, because they depend on geometry and shape, as well as on a large number of parameters characterizing the constraints of the filaments the internal and external mechanical interactions.

To quantify the deformation properties of filaments during several periods of the oscillating flow, we define four basic parameters. The first is the degree of buckling or looping (BU) measured as the ratio of the smallest circle diameter (d_c) binding an object to the filament contour length (Fig. 4.4). Hence BU $\leq$ 1, where BU = 1 corresponds to a straight rod.

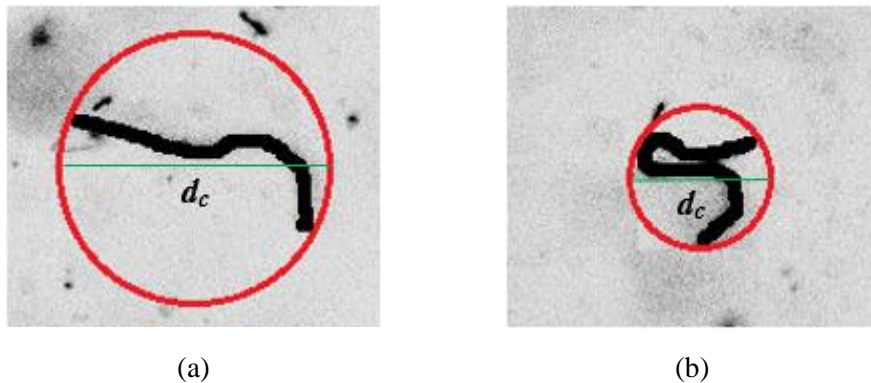| (a)   (b) |

Figure 4.4. Degree of buckling, example of BU evaluation: (a) BU = 0.84; (b) BU = 0.42.

The second shape parameter is the degree of elongation (EL), which is quantified by relating the short (d_e) to the long (L_e) axis of the ellipse encircling filament (Fig. 4.5). Obviously, for rod-like objects EL << 1, while for regularly coiled filaments it approaches 1.

(a)   (b)

Figure 4.5. Degree of elongation, example of EL evaluation: (a) EL = 0.42; (b) EL = 0.60.

For the same encircling ellipse the third quantifier is defined, namely the inclination angle IA of the long ellipse axis in relation to the channel axis (Fig. 4.6). It changes from $-\pi/2$ to $+\pi/2$ for object orientation directed either into the channel inlet or from the inlet.

(a)   (b)

Figure 4.6. Inclination angle, example of IA evaluation: (a) IA = -24.25º; (b) IA = -73.84º.

The end-to-end distance (EE) related to the filament contour length is selected as the fourth shape characteristic (Fig. 4.7). It depicts the bending degree for relatively short filaments.

(a)   (b)

Figure 4.7. End-to-end distance, example of EE evaluation: (a) EE = 0.84; (b) EE = 0.38.

4.5. Cross-flow migration analysis

The observation of hydrogel nanofilaments during the oscillatory flow allowed us to analyse their cross-flow migration. The distance of the centre of mass of the

observed filament from the microchannel centre was chosen. This distance changed during every cycle of the oscillatory flow. The absolute value of the migration velocity U_r was defined as the ratio of the averaged total lateral displacement of the filament mass centre to the time in which the filament oscillated. Due to the hydrodynamic interactions and deformations observed, the filament longitudinal velocity lags slightly behind the fluid flow velocity. Its value related to the local fluid velocity is marked as a *slip* velocity U_s.

4.6.   Results and discussion

4.6.1.   Nanofilament morphology

Fig. 4.8 confirms the presence of a core structure in electrospun fibres. Micrographs indicate core segments in fibres, although the dissolution of the PLCL shell showed that many short nanofilament objects were released together with long hydrogel nanofilaments.

(a)   (b)
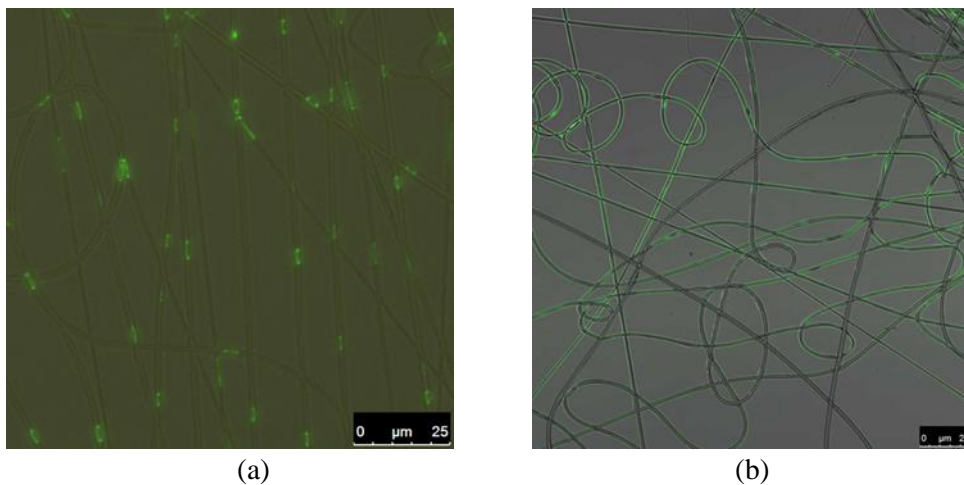
Figure 4.8. Images of core-shell nanofibres from fluorescence microscope (TIRF). Fluorescent parts (core) of fibres indicate (a) short and (b) long hydrogel nanofilaments inside a shell (PLCL) structure.

We found that the hydrogel core pieces differed in length. Depending on the changes in the parameters of the electrospinning process, they formed short (Fig. 4.8 (a)) or long (Fig. 4.8 (b)) hydrogel filaments.

The nanofilaments of AAm:Bis-AAm with a mass ratio (w/w): 37.5:1, 20:1 and 4:1 were labelled as EA1, EA2, and EA3, respectively. The nanofilaments of

4.6 Results and discussion

NIPAAm:BIS-AAm with a mass ratio (w/w): 37.5:1, 20:1 and 4:1 were labelled as EN1, EN2, and EN3, respectively.

The averaged diameters obtained from the SEM images of PLCL/PNIPAm and PLCL/AAm core-shell nanofibres with a hydrogel core of NIPAm:Bis-AAm with a mass ratio of 37.5:1, 20:1, and 4:1 are shown in Table 4.1. The corresponding diameters of the extracted hydrogel filaments are also shown.

Table 4.1. Diameter of core-shell fibres and extracted hydrogel nanofilaments.

AAm/NIPAm : BIS mass ratio	Diameter of PLCL core-shell fibres and extracted hydrogel filaments			
	PLCL/AAm:Bis-AAm	PLCL/NIPAm:Bis-AAm	AAm:Bis-AAm	NIPAm:Bis-AAm
37.5:1	1980 ± 210 nm	1350 ± 380 nm	96 ± 24 nm	126 ± 36 nm
20:1	2100 ± 450 nm	710 ± 310 nm	112 ± 47 nm	170 ± 65 nm
4:1	1270 ± 180 nm	790 ± 150 nm	290 ± 209 nm	257 ± 207 nm

It is rather difficult to control the nanofilament diameter in experiments. This may be achieved by changing the monomer ratio. An increase in the filament diameter was observed when the amount of BIS-AAm was increased. During electrospinning, nanofibres falling onto the collector are thicker as result of the fast core polymerization, which prevents further fibre elongation.

(a)   (b)
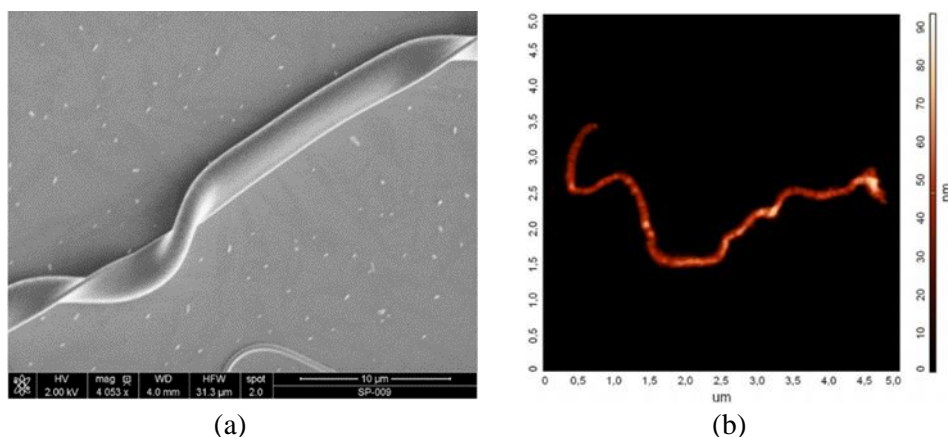
Figure 4.9. (a) Micrograph of a ribbon-like core-shell PLCL/PAAm nanofibre (EA3) observed under SEM; (b) Topography of a ribbon-like nanofilament (EA1) observed by AFM (width 128 nm, contour length 7 μm, height 39 nm, equivalent diameter 80 nm).

We also observed ribbon-like nanofilaments (Fig. 4.9 (a)). The ratio of height to width for the investigated nanofilaments varied from about 5 to over 20 (Fig. 4.10).

We may find some correlation between this size variation and crosslinker concentration. Additionally, it is very likely that the faster polymerization cause

nanofibres not to have enough time for the relaxation of their shape when they leave the nozzle.

Figure 4.10. Average width (a) and height (b) of the analysed hydrogel nanofilaments.

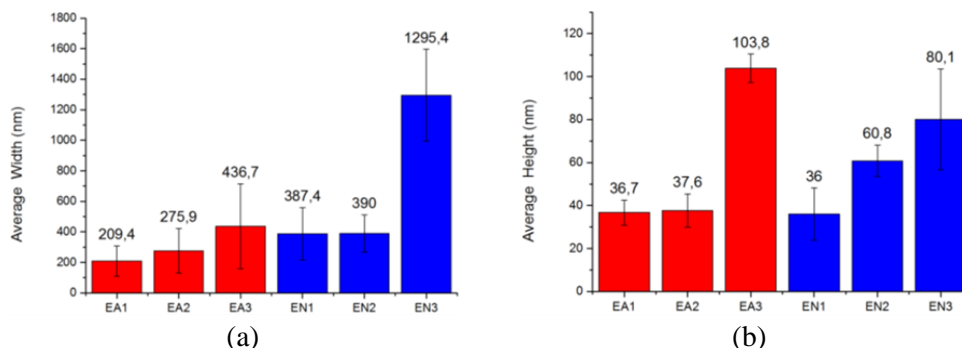It is worthwhile to note that the hydrogel nanofilaments observed under AFM have a typical height in the range of 30 nm to 60 nm, therefore their expected bending direction is most likely anisotropic. A proper diameter evaluation is necessary for the proper estimation of the elasticity. Furthermore, the quantitative theoretical analysis of nanofilament flow-induced deformations is challenging, due to the possible non-uniformity of their shape. Such a non-uniform shape, however, is typical in the case of biological objects such as proteins.

4.6.2. Brownian motion of flexible nanofilaments

The Brownian motion of hydrogel nanofilaments was measured in DMF solution at temperature T = 302 K and viscosity $\eta = 1.02 \cdot 10^{-3}$ Pa s. The typical traced path of a short nanofilament suspended in a fluid, the resulted displacements, and the rotation due to collisions with fluid molecules are shown in Fig. 4.11.
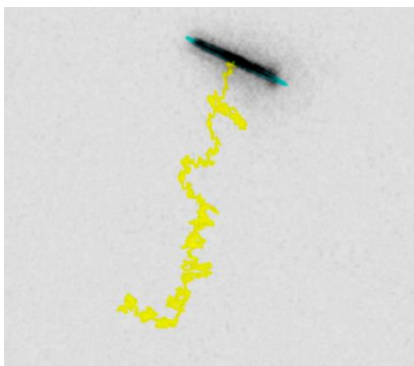

Figure 4.11. Diffusion path (yellow) of a filament with contour length 15.6 μm (Table 4.2, nanofilament no 5). The ellipse outlines the filament and indicates the rotation angle of the filament.

4.6 Results and discussion

Table 4.2. Comparison between experimental and theoretical diffusion coefficients of highly deformable hydrogel nanofilaments suspended in DMF. D_f – flexural diffusion (from persistence length L_p).

No		L/d	D_f [$\mu m^2/s$]	D_a [$\mu m^2/s$]	D_b [$\mu m^2/s$]	D_θ [rad^2/s]	L [μm]	L_p [μm]	Motion	Shape
1	exper.	43.0	0.0018	0.052	0.035	0.0006	21.5	93	Bending	
	theor.	43.0		0.144	0.090	0.0019				
2	exper.	31.2	0.0056	0.093	0.067	0.0025	15.6	29	Rotation	
	theor.	31.2		0.182	0.116	0.0045				
3	exper.	29.8	0.0005	0.059	0.140	0.0029	14.9	339	Rotation	
	theor.	29.8		0.189	0.121	0.0051				
4	exper.	47.8	0.0008	0.231	0.053	0.0005	23.9	211	Bending	
	theor.	47.8		0.133	0.083	0.0014				
5	exper.	31.4	0.0003	0.266	0.070	0.0023	15.6	598	Rotation	
	theor.	31.4		0.182	0.116	0.0044				
6	exper.	48.4	0.0326	0.112	0.105	0.0026	24.2	5	Bending	
	theor.	48.4		0.132	0.082	0.0013				
7	exper.	104.8	0.0326	0.054	0.070	0.0005	52.4	5	Bending	
	theor.	104.8		0.072	0.044	0.0002				
8	exper.	171.0	0.0053	0.039	0.150	0.00005	85.5	31	Bending	
	theor.	171.0		0.049	0.029	0.00004				
9	exper.	105.6	0.0109	0.029	0.087	0.0002	52.8	15	Bending	
	theor.	105.6		0.072	0.043	0.0002				

The diffusion coefficients for hydrogel nanofilaments shown in Table 4.2, were calculated as mean square displacements (eqs. 4.5-4.7). We analysed only

nanofilaments which were far away from the surface of the cover glass (more than 10 μm). The surface proximity could constrain one end of the hydrogel and yield unrealistic results. Diffusion coefficients were measured by tracking analysis.

In the case of short nanofilaments (no 1-5, Table 4.2) we observed that diffusion coefficients are, on average, two times smaller than the theoretical ones calculated for the oblate ellipsoid (eqs. 4.5-4.7). For long nanofilaments (no 6-9, Table 4.2), average diffusion coefficients are two times larger than the theoretical values for an ellipsoid. Theoretical diffusion coefficients are obtained using the length and radius of the observed filaments as a virtual ellipsoid. Obviously these theoretical values should be used only as a reference for the very simplified model of filaments shape.

The figures in Table 4.2 show the typical shapes of the examined nanofilaments. In the first nanofilament there is possibly some narrowing, which could affect the bending dynamics results. In the second flexible filament, we mainly observed a rotation along its main axis (no 2, Table 4.2). All three diffusion coefficients were about two times smaller than the theoretical values for a long, thin prolate spheroid. The third filament was moving along the main (*a*) axis at a slower rate than in the perpendicular direction (along the *b* axis). In contrast to the two previous cases, the diffusion coefficient along the b axis was even greater than the model value for a straight, non-deformable ellipsoid. This may suggest the presence of an additional factor affecting the diffusion between parallel microscope slides. As in previous experiments, the rotational diffusion was lower than its theoretical value.

The fourth filament analysed showed a detectable bending of its arms, and had a higher diffusion coefficient along the *a* axis compared to the theoretical model, but we found a comparable diffusion coefficient along the *b* axis. As in the previous cases, its rotational diffusion was about half that predicted by the equation (4.5-4.7). The fifth nanofilament had the same contour length as nanofilament no 2. The two nanofilaments discussed differ in shape, as shown by the figures in Table 4.2. The experimental diffusion coefficient along the main axis *a* is one and half times higher than the theoretical value. The diffusion path of this nanofilament is shown in Fig. 4.11, where we can see its translational dominated motion. The sixth filament had a contour length comparable to that of the fourth nanofilament but with a different shape, and was observed to bend during the experiment. Both translational diffusion coefficients in the *a* and *b* axis direction were comparable with theoretical values, but its rotational diffusion coefficient was two times greater than in the straight ellipsoid model. This observation may be associated with the shape of nanofilaments. The seventh nanofilament had a contour length of 52.4 μm. It has a much smaller diffusion coefficient than the preceding shorter nanofilaments. The experimental diffusion coefficient in the main axis direction is smaller than to its theoretical value, and – at the same time – the diffusion coefficient along the *b* axis is higher than its theoretical

value. As in the preceding C-shaped nanofilament, the rotational diffusion coefficient was approximately two times higher than the theoretical value for the equivalent ellipsoid. The longest nanofilament (no 8), with a contour length of 85.5 μm, showed a rotational diffusion closer to the theoretical value as compared to other nanofilaments. The diffusion coefficient along the *b* axis, however, is nearly five times greater than the theoretical value for the ellipsoid. For the last, ninth, L-shaped nanofilament, we observed smaller experimental diffusion coefficients in both directions, compared to its theoretical model values. Its translational diffusion was almost in agreement with the rotational diffusion coefficient for the equivalent ellipsoid. The typical frames of these filaments exhibiting bending dynamics are shown in Fig. 4.12.

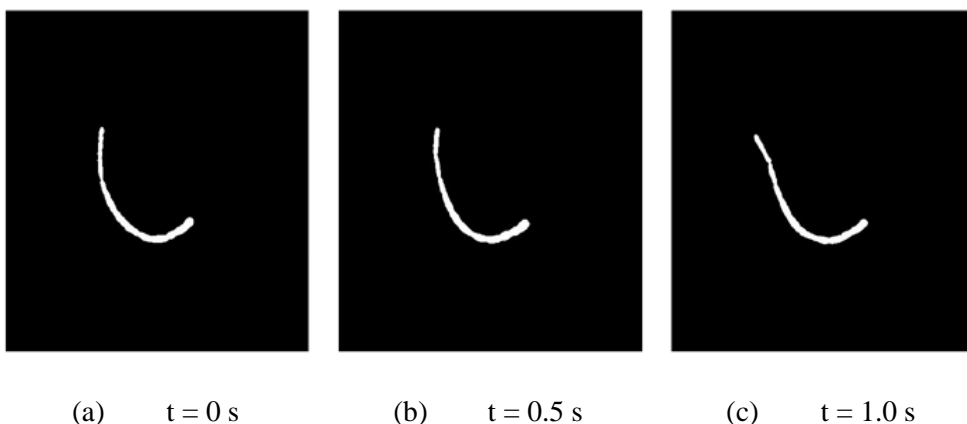(a)   t = 0 s   (b)   t = 0.5 s   (c)   t = 1.0 s

Figure 4.12. Binary images demonstrating the filament bending. These images were used for the calculation of the persistence length. The contour length of the nanofilament was equal to 52.8 μm (Table 4.2, no 9).

Fig. 4.13 (a) shows the nanofilament mean square displacement for translational (along *a* and *b* axes) and rotational diffusion. We can see the more or less linear passage of the curves obtained. Each filament was divided into two segments, and three main points were marked on the object analysed.

The evaluation of bending dynamics as a result of thermal fluctuations was possible thanks to the analysis of the angle between the two arms of the nanofilament (Fig. 4.13 (b)). The nanofilament arms were in the range of 11.8°. Additionally, we measured the distance between arm ends and arm lengths to confirm bending and exclude rotation. For C-shaped nanofilaments, the rotation of the nanofilaments would cause filament ends to go out of focus and, apparently the length of the arms will be shorten. This effect was used to rule out such cases during the bending evaluation. This meant that filaments whose length varied more than 10% during observation were eliminated from further analyses. In the case of the data shown (Fig. 4.13 (c)),

we can see that the distance between the arm ends and the variation in their length is around 3%, thus proving the bending of the filaments.

(a)

(b)

(c)
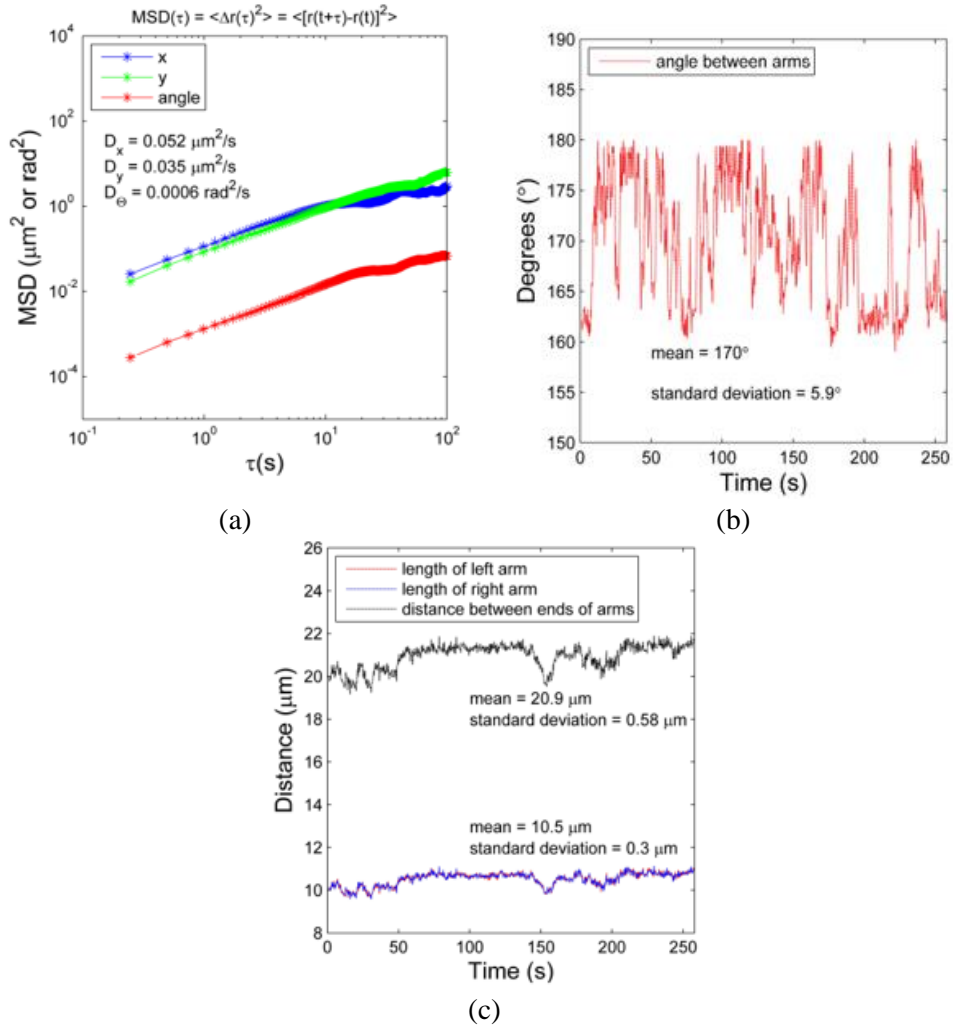
Figure 4.13. (a) Plot of the mean square displacement of filaments with a 21.5 μm contour length in function of lag time. The upper two plots are MSDs along axes *a* and *b* in terms of μm^2, whereas the bottom one is the angular MSD in terms of rad^2. (b) Angle between arms of the bending filament based on time. (c) Length of left and right arms of the bending filament and length of distance between the arm ends. All plots show calculations for the nanofilament no. 1 from Table 4.2.

An example of frames captured during the bending of the nanofilament is shown in Fig. 4.14.

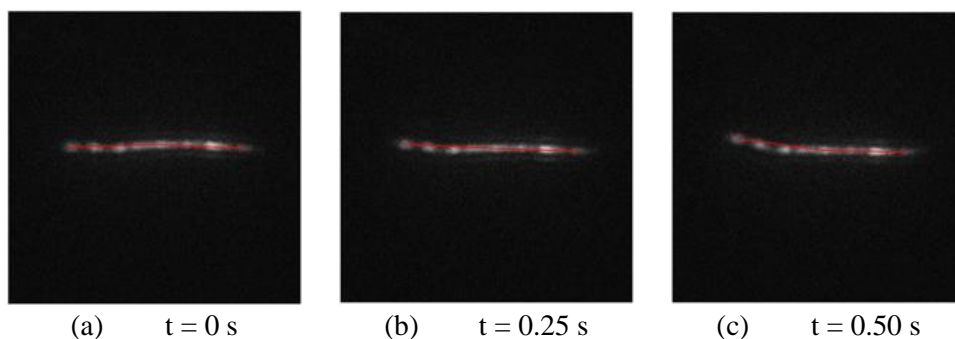(a)   t = 0 s   (b)   t = 0.25 s   (c)   t = 0.50 s

Figure 4.14. Bending dynamics of a nanofilament (Table 4.2, nanofilament no. 1). Red lines indicate the fibre arms starting from its centre of mass. The angle between the red lines was measured to assess flexibility.

4.6.3. Evaluation of mechanical properties of hydrogel nanofilaments

In Table 4.3 we summarized the results of three experimental methods aiming to estimate the bending Young modulus of selected samples of the nanofilaments obtained using six different compositions of hydrogels. The three experimental methods used are described in the following subsections. As previously mentioned, each experimental method applied has its pros and cons. Therefore, before selecting the proper hydrogel samples for forthcoming experiments in the channel flow, we found it necessary to gain some fundamental knowledge on the possibility of evaluating their mechanical properties.

Table 4.3. Young modulus evaluated by AFM nanoindentation, cosine correlation, and hydrodynamic interactions methods. We analysed three types of nanofilaments with different AAm:BIS-AAm and NIPAAm:BIS-AAm mass ratios. Only one experiment performed for EN1 material was successfully accomplished for evaluating Young modulus by the hydrodynamic interaction method.

Experiment	Young modulus E (kPa)		
	AFM nanoindentation	**Cosine correlation (Thermal fluctuations)**	**Flow hydrodynamic interactions**
EN1	-	4.5 ± 0.4	2.3
EN2	8.50 ± 1.19	3.1 ± 1.7	-
EN3	18.11 ± 4.85	3.8 ± 1.1	-
EA1	4.06 ± 1.18	6.1 ± 2.6	-
EA2	15.80 ± 2.77	5.0 ± 1.1	-
EA3	55.82 ± 5.64	5.8 ± 0.8	-

4.6.3.1. Evaluation by AFM nanoindentation

Table 4.3 shows the result of hydrogel filaments Young modulus obtained by several AFM measurements. The average Young modulus obtained for three different nanofilaments was given. It should be noted that the applicability of the AFM nanoindentation method must be limited to extremely soft objects. This is mostly due to the fact that the stiffness of the cantilever is relatively higher, compared to the fluid-like behaviour of the hydrogel. Results were averaged over all recorded measurements. In most cases, the values obtained overlap the data already available for such materials [90]. The wide range of results obtained is a consequence of the non-uniform nanofilament geometry, their environmental interactions, and a problematic procedure for catching the proper part of the filaments. The main problem with AFM nanoindentation is that the stiff substrate contributes a great deal to soft and thin materials. Because of this, nanoindentation outcomes may differ from the actual sample stiffness; therefore, it was decided to compare them with the Young module values obtained using two other methods.

4.6.3.2. Evaluation from thermal fluctuations

For the Young modulus evaluation of nanofilaments made by different monomer ratios, the persistence length with the cosine correlation was found to be the easiest, most direct method. For this method, around 500–700 images were analysed per single nanofilament. The time interval of the image sequence was 0.25 s. All experiments were conducted under the same experimental conditions for the different samples. As we can see in Table 4.3, the results of the Young modulus evaluated by the cosine correlation method do not show an increasing trend with increased crosslinker amounts, in contrast to the AFM nanoindentation results. We also observed that PAAm filaments are slightly less flexible than PNIPAAm filaments. This is consistent with the results presented in the literature.

We compared the data obtained by the persistence length method with the diffusion coefficients of analysed nanofilaments and show them in Fig. 4.15. The relation between persistence length (flexibility) and diffusion is very weak. But if we look at filaments no. 4 and no. 5 we can see that a straight filament shape and higher stiffness are correlated with a relatively high longitudinal diffusion. For this reason, it is necessary to include the shape parameterisation in order to find any possible correlation between persistence length and diffusion.

We should also remember that Young modulus measurements based on the persistence length are evaluated using a theoretical formulation neglecting any hydrodynamic interactions with the environment. It would be interesting to know the

damping effect of liquid viscosity on the evaluated persistence length. In Table 4.2 we show flexural diffusivity, a parameter taking into account the viscous damping exerted by the surrounding filament liquid. In the case of bending fluctuations (cases 6 and 7 in Table 4.2), the contribution of flexural diffusivity is evidently dominant over translational or rotational diffusion. This illustrates the difficulty in formulating a single interpretation of the dynamics of long, deformable molecules suspended in a complex, viscous biological environment.
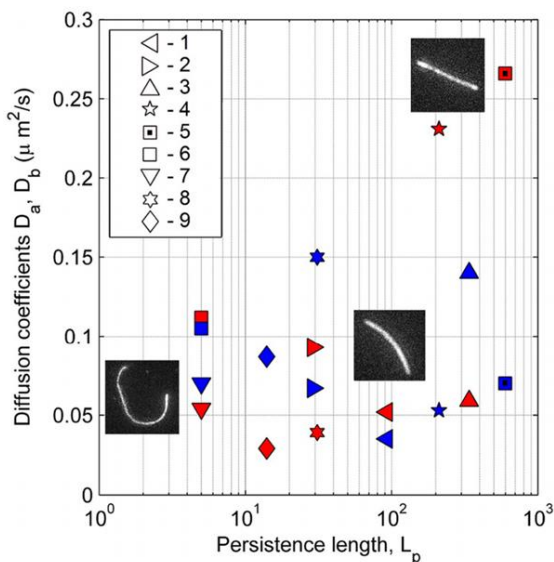

Figure 4.15. Translational diffusion coefficient D_a (red symbols) and D_b (blue symbols) as a function of persistence length for the analysed filaments shown in Table 4.2.

4.6.3.3. Evaluation from hydrodynamic interactions

Data acquired during the recovery of the bent filament five seconds after stopping the flow were used for the Young modulus calculation. Fig. 4.16 shows three images of our experimental procedure.

The flow applied deformed the filament attached to the wall. Only the part attached to the wall seems to be bent, with the upper part responsible for the acting drag force. The phase of recovery of the initial position was analysed to evaluate the mechanical properties of the filament. To calculate the Young modulus of the filament, we used the data on the varying filament position taken during time intervals of about three seconds and recorded five seconds after the flow was paused. During this three-second observation time, the filament was moving back to its original position at an apparently constant angular velocity. Its linear velocity at any point on the filament was equal to $V = 1.34$ μm/s. The drag force acting on a stiff fibre part

(L_1 = 145.38 μm) was equal to $4.53 \cdot 10^{-13}$ N. Thus the Young modulus calculated for the flexible part (L_2 = 39.14 μm) was found to be equal to 2.34 kPa.

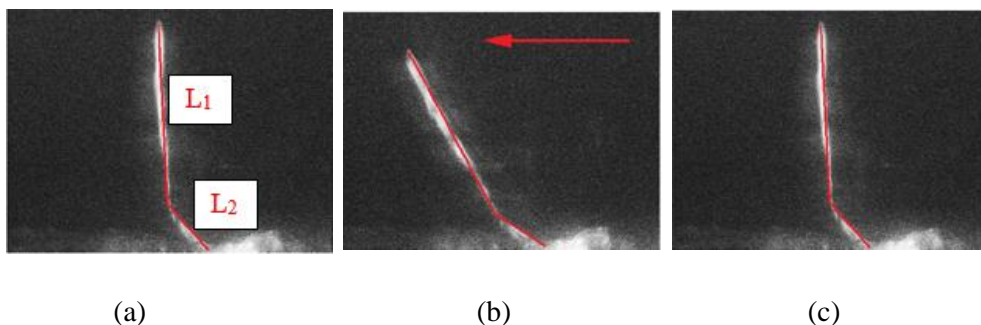(a)   (b)   (c)

Figure 4.16. Bending of a filament in a flow recorded by fluorescence microscopy; (a) – initial position, (b) – bending of the filament triggered by the flow, (c) – returning phase of the filament after the flow was stopped. L_1 – stiff part of the filament, L_2 – flexible part of the filament attached to the wall.

The Young modulus value calculated by the hydrodynamic method appeared to be comparable to that obtained by the persistence length method (Table 4.3). The hydrodynamic method appeared to be the most reliable method for evaluating elastic interactions with the environment. On the other hand, it also appeared to be the most difficult to carry out, and not accurate enough to be evaluated. Due to the difficulties encountered in finding additional filaments perpendicular to the channel wall after the dissolution of the fibre shell, only one such experiment was reliable enough to be evaluated. It was difficult to repeat this experiment with other filaments. For this reason, we evaluated the Young modulus by the flow method only for one hydrogel formulation EN1.

4.6.4. Filament shape variation under flow interactions

The configuration of the oscillating flow proposed in this study resembles in vivo conditions. Bio-objects are transported by inter-tissue and time-dependent fluctuations of the flow field. It is also important to point out that, the oscillatory flow makes it possible for us to visualize the dynamics of nanofilaments in one detection regime over a relatively long recording time.

Our pulsate pump allowed to maintain the maximum amplitude of the flow oscillations imposed to remain constant throughout the entire observation period, in the first and in the second half of the cycle, where we applied a reverse flow (Fig. 4.17). The flow velocity gained its maximum value at oscillatory phases $\pm n\pi/2$, where n = 1, 3, 5, etc. Numerical and experimental data evidenced that the flow generated in the microchannel was not characterized by any phase lags, thus

confirming the low Reynolds number (*Re* < 0.2) almost purely sinusoidal flow characteristics. Therefore, we may assume that the flow we applied was in a quasi-steady creeping flow regime.
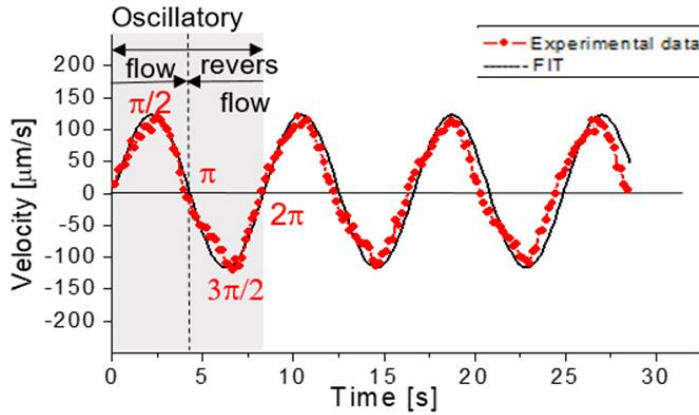

Figure 4.17. Oscillatory flow waveform generated by our home-built pulsatile pump. The horizontal solid line at *V* = 0 (for *nπ* = 0, 1, 2, etc.) marks cross-points of short stop-flow intervals at which some changes in nanofilament conformation and migration were recorded for each constitutive oscillatory cycle. At *V* = *nπ*/2 (for *n* = 1, 3, 5, etc.), hydrogel nanofilaments experienced the maximum flow velocity, which was used to define nondimensional flow characteristics. Empirical data are compared with the sinusoidal fit function.

In microchannels with rectangular cross-section, and especially in those with a high aspect ratio (e.g. Hele-Shaw configuration), the flow pattern along two main axes is substantially different. In addition, the presence of sharp corner edges generates relatively high local shear stresses that may affect the dynamics and migration behaviour of nanoobjects conveyed into such microchannels. Therefore, to obtain reliable information on local shear rates and velocity flow profile, we performed a finite element simulation of the oscillatory flow inside a rectangular microchannel. As expected, the shape of the velocity profile takes a plug-like shape already at the beginning of the oscillatory cycle (Fig. 4.18, red line), and not a truly parabolic shape, as in a microchannel with a circular (or squared) cross-section.

Experimental data were obtained by calculating the velocity of individual hydrogel debris located at a given distance from the microchannel wall, where 0 and 100 μm denote the microchannel centreline and wall, respectively. They were fitted with a higher order parabola, which offered an easy way to evaluate the local velocity at each position inside the microchannel:

$$V(x,t) = V_{max}\left[1 - \left|\left(\frac{x}{0.5W}\right)^{4.5}\right|\right]sin(\omega t) \tag{4.22}$$
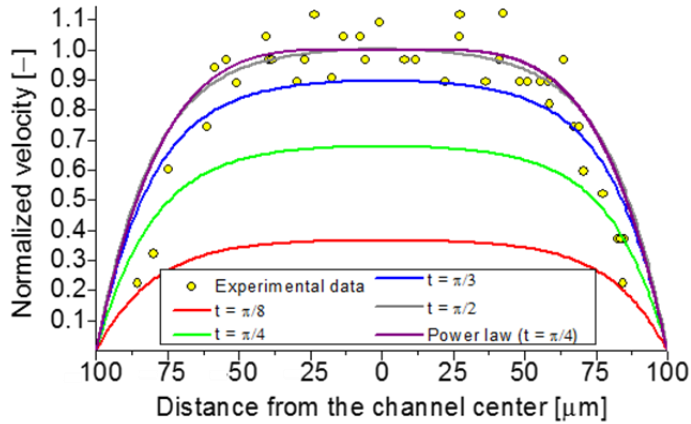
Figure 4.18. Velocity flow field from finite element method simulations of the oscillatory flow. Yellow dots represent experimental data; the violet line signifies fit by higher order parabola; red, green, blue, and grey lines represent the results of numerical simulations obtained for different time steps.

Since the velocity profile in a rectangular geometry is blunted compared to the parabolic distribution in a circular cross-section, shear rates in the centre of rectangular microchannels are expected to be smaller than those in circular tubes (comp. Fig. 4.19).
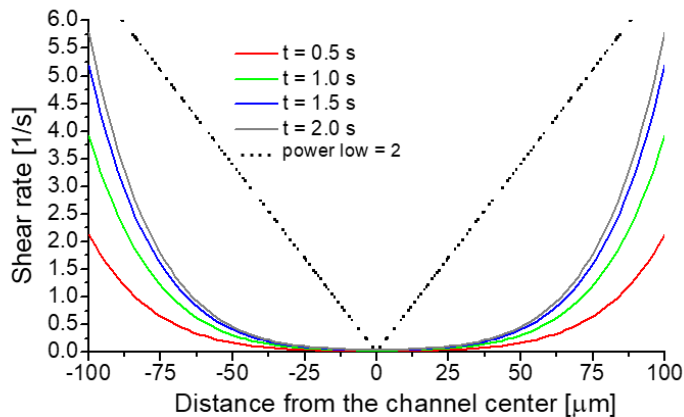

Figure 4.19. The shear rate distribution across the rectangular microchannel was calculated in a few stages of the oscillatory cycle and compared with theoretical values for parabolic flow profile (dots).

Our computational analysis of the velocity profile inside a rectangular geometry revealed that its plug-like shape in the x-y dimensions is purely defined by the

microchannel aspect ratio. Such a blunted distribution is very similar to the velocity profile typically found in large arteries or arterial tree networks [91].
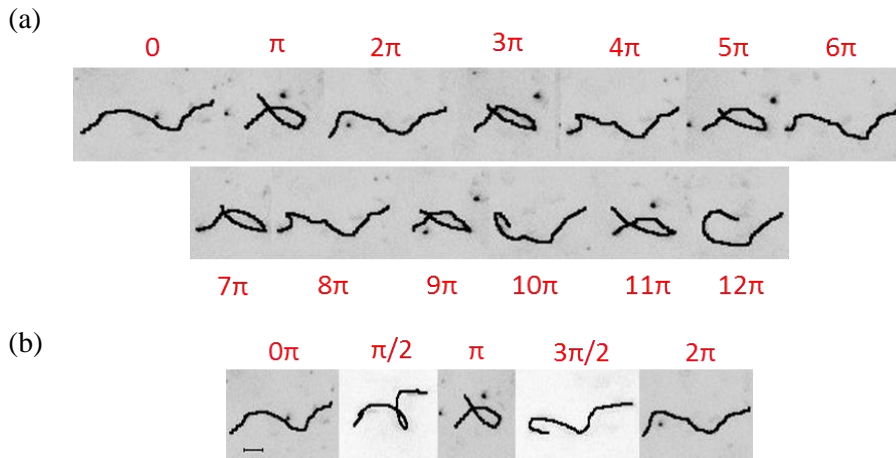

Figure 4.20. Characteristic bent-like configurations of long hydrogel nanofilaments ($\underline{L} = 500$) at different time points over the course of an experiment (a) and during one oscillatory cycle (b).

The observation of hydrogel nanofilaments under the influence of an oscillatory flow helps us understand how this type of flow affects the conformation of elongated objects [92]. For this purpose, we followed the filaments' motion and evaluated the changes in their shape based on time. The behaviour of the nanofilaments during the oscillatory flow helped us select two groups: bent-like filaments and U-shaped filaments. They are represented by different ratios between contour length and diameter ($\underline{L} = L/d$). Long chain nanofilaments ($\underline{L} = 500$ bent-like) change their shape continuously between uncoiled (bent) and coiled conformations (Fig. 4.20 (a)). The chain coiling always takes place during the first half of the oscillatory cycle. The chain returns to its original uncoiled configuration when the direction of the flow reverses in the second half of the cycle (Fig. 4.20 (b)). These changes in nanofilament shape are not related to any sudden motility changes such as rotation or tumbling. Overall, the degree of chain entanglement progresses with an increasing number of oscillatory cycles over time. At each consecutive forward flow (at $n\pi$, where $n = 2, 4, 6$, etc.) and reverse flow (at $n\pi$, where $n = 1, 3, 5$, etc.), the nanofilaments become more compressed.

Within the limit of short chains ($\underline{L} = 250$), hydrogel nanofilaments originally show a U-shaped contour (Fig. 4.21 (a)).
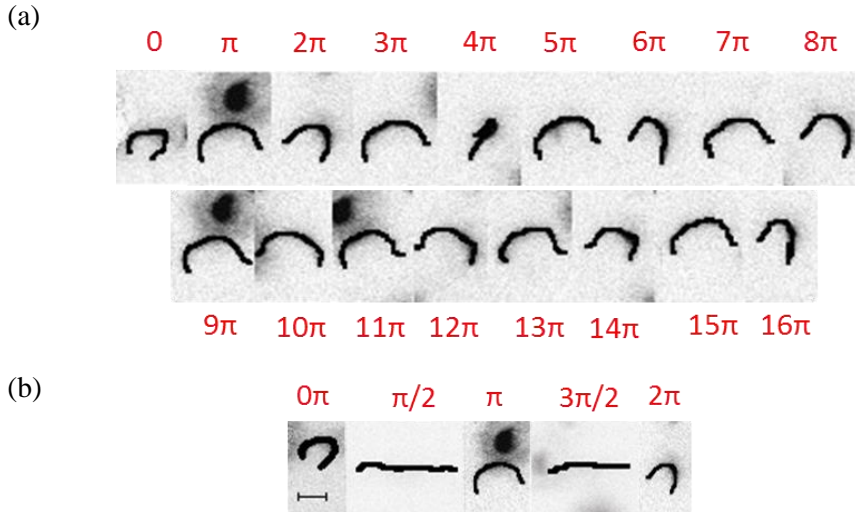
(a)

(b)

Figure 4.21. Characteristic U-shaped configurations of short hydrogel nanofilaments ($L = 250$) at different time points over the course of an experiment (a) and during one oscillatory cycle (b).

In each oscillatory cycle, we can find two distinct phases which reach the chain: (i) a straightening period, and then the rotation within x-y planes that results in bending in the other direction (at $n\pi$, where $n = 1, 3, 5$, etc.); (ii) a reverse straightening and rotation period, when the chain goes back to its original conformation (at $n\pi$, where $n = 2, 4, 6$, etc.). Over time, at each forward and reverse cycle, the chain straightens slightly with respect to its original configuration (Fig. 4.21 (b)). Consequently, they behave as flexible polymer chains (e.g. DNA), while U-shaped filaments behave as semiflexible objects (e.g. actin) [93-96].

4.6.5. Characteristic parameters of nanofilaments in a flow

Relative extensional (Hookean) stiffness $K \sim 120$ and relative flexural stiffness $A \sim 70$ are typical values characterizing hydrogel nanofilaments of high slenderness L (Table 4.4). This means that such objects (in our experimental conditions) are characterized by low extensibility and very high bending flexibility. At the same time, the capability of nanofilaments to undergo thermal fluctuations is determined by a very limited bending stiffness of $\kappa = 4 \cdot 10^{-26}$ Nm^2 and short persistence length (< 10 μm). We find that the mechanical properties of nanofilaments with a contour length of less than 40 μm and $L \sim 250$ are similar (Table 4.4). To compare them with elongated biological molecules, the same table also includes some basic parameters from literature data for actin [80] and short DNA [97]. For the evaluation of A and K as non-dimensional mechanical characteristics for actin and DNA biomolecules, the

corresponding values were scaled to our experimental parameters, i.e. the channel width (*200 μm*) and flow velocity (*100 μm/s*).

Table 4.4. Comparison of the mechanical properties of highly deformable hydrogel nanofilaments, (semi)flexible actin filaments, and DNA molecules.

	Hydrogel nanofilaments		Actin[80] $\underline{L} \sim 7 \cdot 10^{3}$	(λ) DNA[97] $\underline{L} \sim 10^{4}$
	$\underline{L} \sim 500$	$\underline{L} \sim 250$		
d	109 – 165 nm	105 – 181 nm	7 nm	2 nm
L	40 – 83 μm	26 – 41 μm	< 50 μm	~ 20 μm
E	2 kPa	2 kPa	2.6 GPa	0.3 – 1 GPa
L_p	3 – 18 μm	3 – 25 μm	17 μm	50 nm
κ	$1 \cdot 10^{-26} - 7 \cdot 10^{-26}$ Nm^2	$1 \cdot 10^{-26} - 10 \cdot 10^{-26}$ Nm^2	$7 \cdot 10^{-26}$ Nm^2	$2 \cdot 10^{-28}$ Nm^2
L_p/L	0.08 – 0.22	0.09 – 0.79	0.34	$2.5 \cdot 10^{-3}$
A	13 – 124	35 – 161	$7 \cdot 10^{5}$	$9 \cdot 10^{4}$
K	16 – 343	33 – 369	$6 \cdot 10^{3}$	95

Our hydrogel nanofilaments have a very high water content (~ 90%) Therefore, they should be treated as highly flexible and inextensible objects ($L_p / L << 1$). In our flow experiment we analysed their shape deformations. The shape deformations observed seem to mimic the behaviour of long biopolymers (e.g. actin filaments and DNA chains). It can be seen, however, that both the extensional stiffness K and the relative flexural stiffness A of hydrogel filaments are much lesser than those of biomolecules (Table 4.4). This indicates an extraordinary deformability of such objects when compared with biopolymers, and – in a similar flow configuration – the expected deformations of DNA and actin filaments would be much smaller.

On the basis of the data showing the similarity of bent-like and U-shaped nanofilaments characterized by a similar diameter and Young modulus, it can be stated that their shape deformations are determined mainly by their length. Additionally, it was found that the Peclet numbers *Pe* of all the investigated configurations showed relatively high values. The approximate values of the Peclet number for bent-like (7000), U-shaped stretched (800), and U-shaped buckled (1600) nanofilaments are shown in Table 4.5. This indicates that the effects of nanofilament translational thermal fluctuations are small compared to hydrodynamic forces. Only during relatively short stop-flow time intervals, when flow reversal takes place, is there a possibility for thermal fluctuations to dominate flow-induced filament deformations, while slight stochastic displacements of their position may occur [98].

At the same time, similar persistence length and bending stiffness of hydrogel nanofilaments rule out the influence of different mechanical properties on the chain shape. This is demonstrated by the great differences in the Sperm number (*Sp*) [88], which has an approximate value of 160 for the bent filaments versus 9 and 6 for U-shaped stretched and U-shaped buckled filaments, respectively. These data may suggest that the viscosity-induced strain plays a dominant role in nanofilament conformations.

Table 4.5. Comparison of the nondimensional numbers for electrospun hydrogel nanofilaments, the bead-spring model of flexible polymers, and biodegradable polymers used in early experiments by Sadlej et al. [93].

	Hydrogel nanofilaments			Bead-spring model[56, 99, 100] $(\underline{L} = 20)$	Polymer fibres[93]	
	Bent-like $(\underline{L} \sim 500)$	U-shaped buckled $(\underline{L} \sim 200)$	U-shaped stretched $(\underline{L} \sim 250)$		PCL $(\underline{L} \sim 50)$	PLLA (~ 50)
Sp	16 – 674	3 – 10	1 – 20	$2.4 \cdot 10^3$	$3 \cdot 10^{-8}$	$2 \cdot 10^{-8}$
Pe	2080 – 23056	1498 – 1844	485 – 1240	-	22	22
K	16 – 343	33 – 114	77 – 369	10	$2 \cdot 10^7$	$5 \cdot 10^7$
A	13 – 124	35 – 54	62 – 161	0.5	$7 \cdot 10^7$	$2 \cdot 10^8$
U_r	$5 \cdot 10^{-6} - 1 \cdot 10^{-3}$	$2 \cdot 10^{-5} - 1 \cdot 10^{-3}$	$7 \cdot 10^{-5} - 2 \cdot 10^{-3}$	$5 \cdot 10^{-4}$ *	-	-
U_s	0.7 – 1	0.93 – 0.96	0.82 – 0.99	0.999 *	-	-

* mean value for initial fibre position $\underline{x} = 0.6$. [93]

In the presence of the oscillatory flow, hydrogel nanofilament thermal bending fluctuations are very small (*Pe* >>1). Filament conformations are subjected to some periodic coiling/uncoiling or rotations, depending on their length. At a high Peclet number, the bending of an elastic chain is promoted by hydrodynamic forces. Therefore, the bending probability is expected to be higher for chains of polymers with very high flexibility. The Sperm number *(Sp)* controls the threshold of the flow-induced flexible bending. Filaments with high *Sp* values [86, 101, 102] are easily deformed by the flow. Consistently, U-shaped nanofilaments feature a 17- to 27-times lower Sperm number than bent-like nanofilaments (Table 4.5). The coiling/uncoiling conformations of bent-like nanofilaments are assisted by the compression of length during each next oscillatory cycle. In U-shaped nanofilaments, low values of *Sp* indicate that their conformation is more rigid. This is also visible in a greater L_p/L ratio.

The stretching and coiling of longer nanofilaments resemble the DNA chain flexibility [94, 103]. Such flexibility is believed to be crucial in the formation of gene

regulatory complexes [104] and in the transport of macromolecules through nuclear pores [105]. Nanofilament elastic mechanical properties are more similar to those of semiflexible actin filaments than DNA chains (Table 4.4), but hydrogel nanofilaments can mimic the behaviour of both types of biopolymers in response to hydrodynamic forces.

The worm-like chain (WLC) model is commonly used to describe the elastic properties of inextensible and flexible chains of biopolymer [106]. The hydrodynamic interactions of long polymer chains are evaluated mostly on the basis of the WLC bead-spring chain models [22, 23, 93, 107, 108]. Two already-mentioned model parameters, i.e. relative extensional stiffness (K) and relative flexural stiffness (A), are useful for the characterization of the polymer chain mechanical properties in response to the shear stresses of a viscous flow. In Table 4.5, these model parameters for hydrogel nanofilaments are presented and compared with those for the fibres produced from elastomeric polymers (polycaprolactone (PCL) and polylactic acid (PLLA)), which were used in the experiment of Sadlej et al. [93]. Due to their very low bending probability (low Sp values), low extensibility, and bending deformability (high K and A values), their dynamics may show a lack of compliance with the predictions of the WLC model applied there [93] (comp. with bead-spring model in Table 4.5).

4.6.6. Elongation and bending analysis

The analysis of the degree of buckling (BU) and degree of elongations (EL) parameters confirmed the division of hydrogel nanofilaments into two groups, while a more detailed observation of migration direction and flow velocity made it possible to divide the U-shaped group of buckled filaments into two sub-groups.

Examining the changes in BU and EL values over time (subsequent cycles) for these three classes of filaments (Fig. 4.22 (a), (c), (e)), the different characters of the waveforms were visible. The first group, referred to as bent-like, is particularly distinguishable. The graphs of BU and EL variations show an approximately sinusoidal nature (Fig. 4.22 (a)). When comparing the graphs for bent-like filaments and U-shaped buckling filaments, it is important to note the differences in the parameter values between the two phases of flow oscillation (0 and π).

(a)

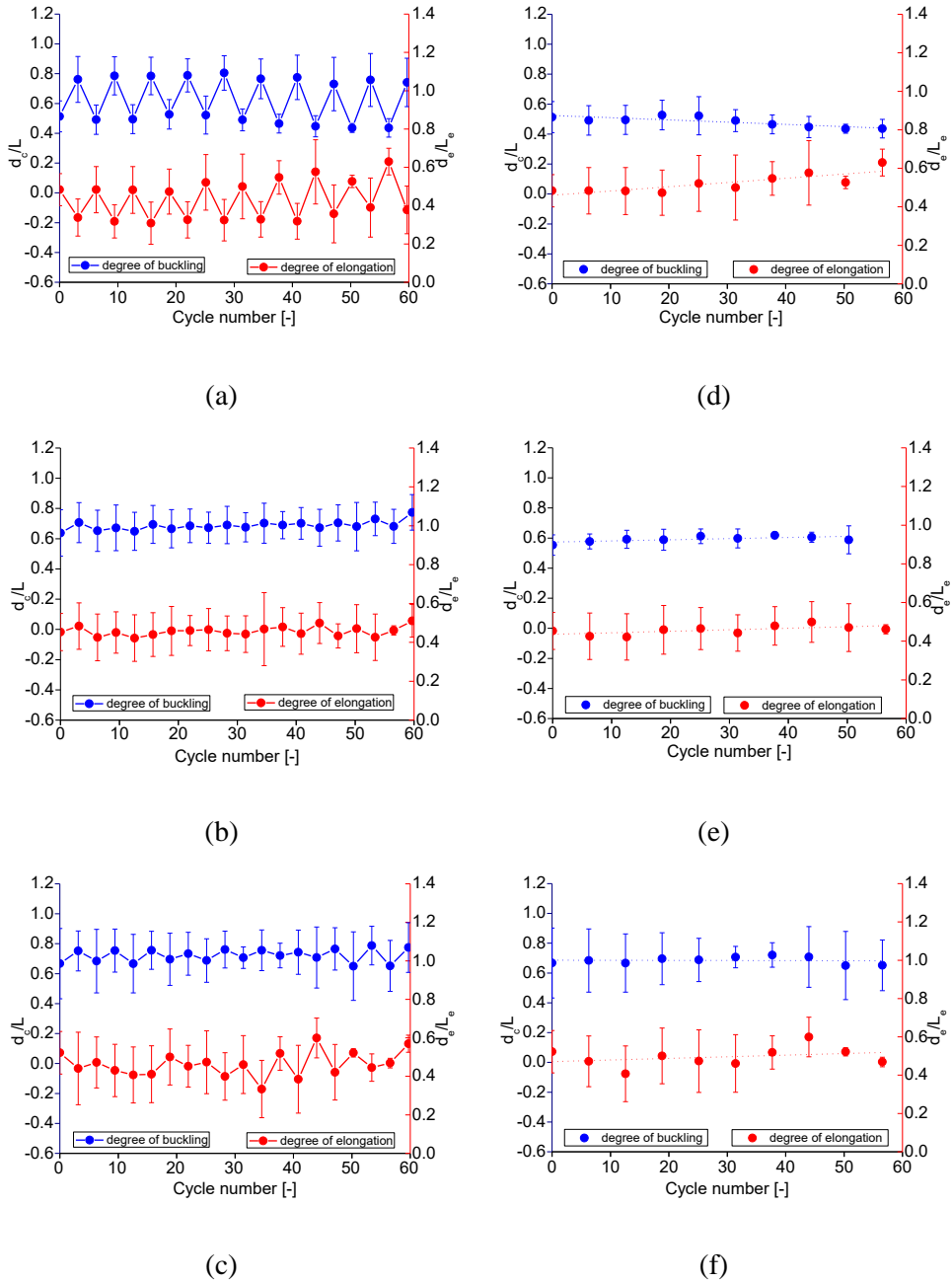
(d)

(b)

(e)

(c)

(f)

Figure 4.22. Changes in the degree of buckling and elongation parameters for (a) bent-like filaments, (b) U-shaped stretched filaments, (c) U-shaped buckled filaments in each phase; (d, e, f) – in 2π phase. Left axis – BU, right axis – EL.

For bent-like filaments, the differences are around 0.2. For the filaments of the second group (Fig. 4.22 (c) and (d)), differences are halved. This can be explained by the shape changes in the first group of filaments over a single oscillatory cycle. For example, at 0 phase the filament is coiling (smallest value of d_c/L), but at π phase the same filament is uncoiling (increased value of d_c/L). Filaments from the second group (Fig. 4.22 (c), (d)) change their shape only slightly with the change of the cycle phase during the oscillatory flow. They mainly rotate or tumble. Consequently, d_c/L and d_e/L_e changes are smaller, and the waveforms of these changes are more regular.

When we look at the changes in the buckling parameter recorded in the same oscillatory phase (0), we can see how the shape of the filaments changes during the oscillatory flow. In the case of bent-like filaments, the d_c/L values are continuously decreasing, i.e. oscillations cause a constantly increasing coiling up of the filament (Fig. 4.22 (b)). The same situation occurs in the π phase of oscillations for uncoiling filaments. In the U-shaped buckling group of filaments, there are two types of behaviour. In the first sub-group, changes recorded in the same phase of each cycle are small, but we see a tendency to increase the d_c/L coiling parameter when the oscillatory time progresses (Fig. 4.22 (e)).

The mean velocity value of these U-shaped stretched filaments (145 μm/s) determines their straightening (from U shape to C shape). U-shaped buckled filaments moving at a higher flow velocity (250 μm/s) are only conveyed by the fluid flow. Filament shapes do not significantly change during the oscillatory flow, and the graph of the changes in d_c/L values recorded for each cycle at a phase equal to 0 is flat (Fig. 4.22 (f)).

Bent-like nanofilaments are characterized by an increased compression at each consecutive phase of forward (at $n\pi$, where $n = 2, 4, 6$, etc.) and reverse (at $n\pi$, where $n = 1, 3, 5$, etc.) flow cycles (Fig. 4.23 (a), (b)). If we look at the changes in the end-to-end parameters of bent-like filaments over full observation time, we can see that in this type of filaments there was a 2-fold decrease in this distance (Fig. 4.24 left). What is very interesting and worth noting is that – configuration-wise – hydrogel bent-like nanofilaments greatly resemble flexible polymer chains [86, 94-96]. Conversely, the U-shaped stretched nanofilaments are characterized by a slight straightening of the chain with respect to its original configuration in each phase of the cycles (forward and reverse) (Fig. 4.23 (c), (d)). In this case, the end-to-end distance increased (Fig. 4.24 middle). In the U-shaped nanofilaments group, there was a chain population that did not change their elongation during the oscillatory flow (Fig. 4.23 (e), (f)). These nanofilaments, called U-shaped buckled, did not change their configuration during entire observation period (Fig. 4.24 right), and responded to the flow by preserving their bulk rotational movement [98]. This type of hydrogel nanofilaments is similar to semiflexible chains of polymers, such as actin filaments [80, 95, 109, 110].
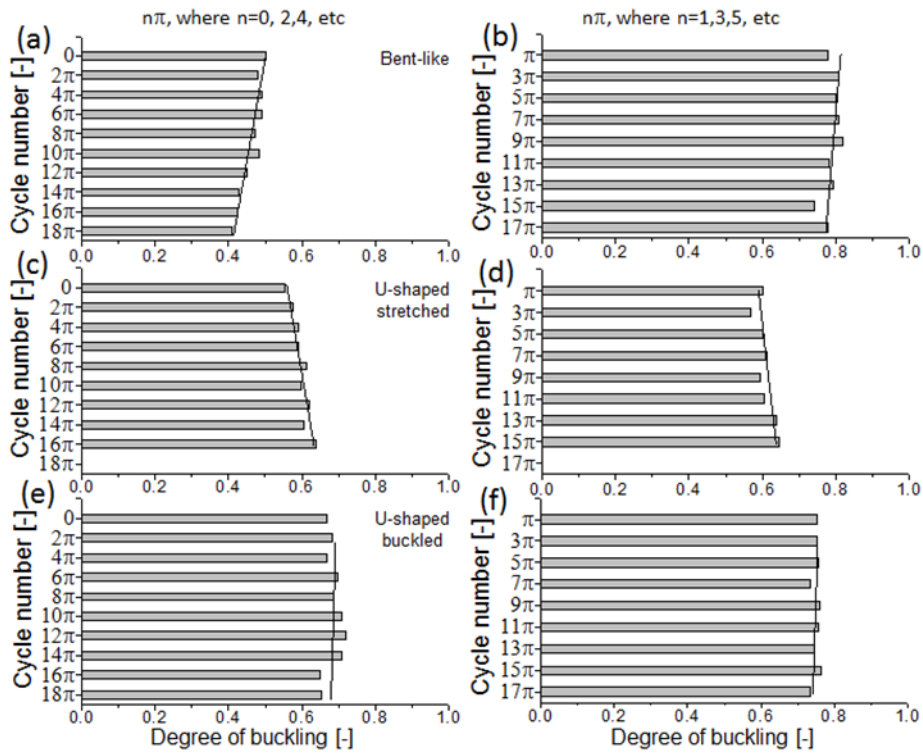
Figure 4.23. Time-dependent changes in the degree of buckling for bent-like (a, b), U-shaped stretched (c, d) and U-shaped buckled (e, f) hydrogel nanofilaments at each individual forward (left column) and reverse (right column) oscillatory cycle. Nanofilaments were subjected to a maximum of 9-10 consecutive oscillatory runs. Solid lines mark the data trend.
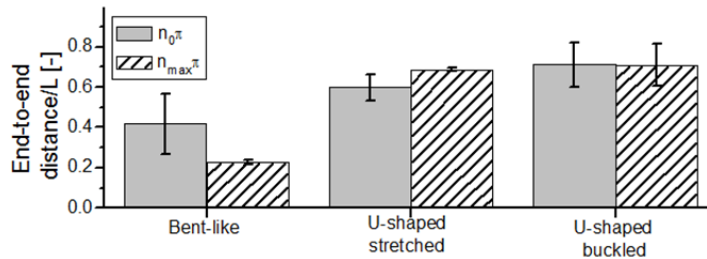

Figure 4.24. Changes in the end-to-end contour length distribution for the three groups of hydrogel nanofilaments, before the application of a hydrodynamic force (*grey bars*) and after the final 10th oscillatory cycle (*dashed-patterned bars*).

4.6.7. Orientation – inclination angle

Differences in the behaviour of two types of filaments and between two groups of filaments classified as U-shaped were also observed when we analysed the change in the filament angle of inclination to the fluid flow in the direction of the x-axis.
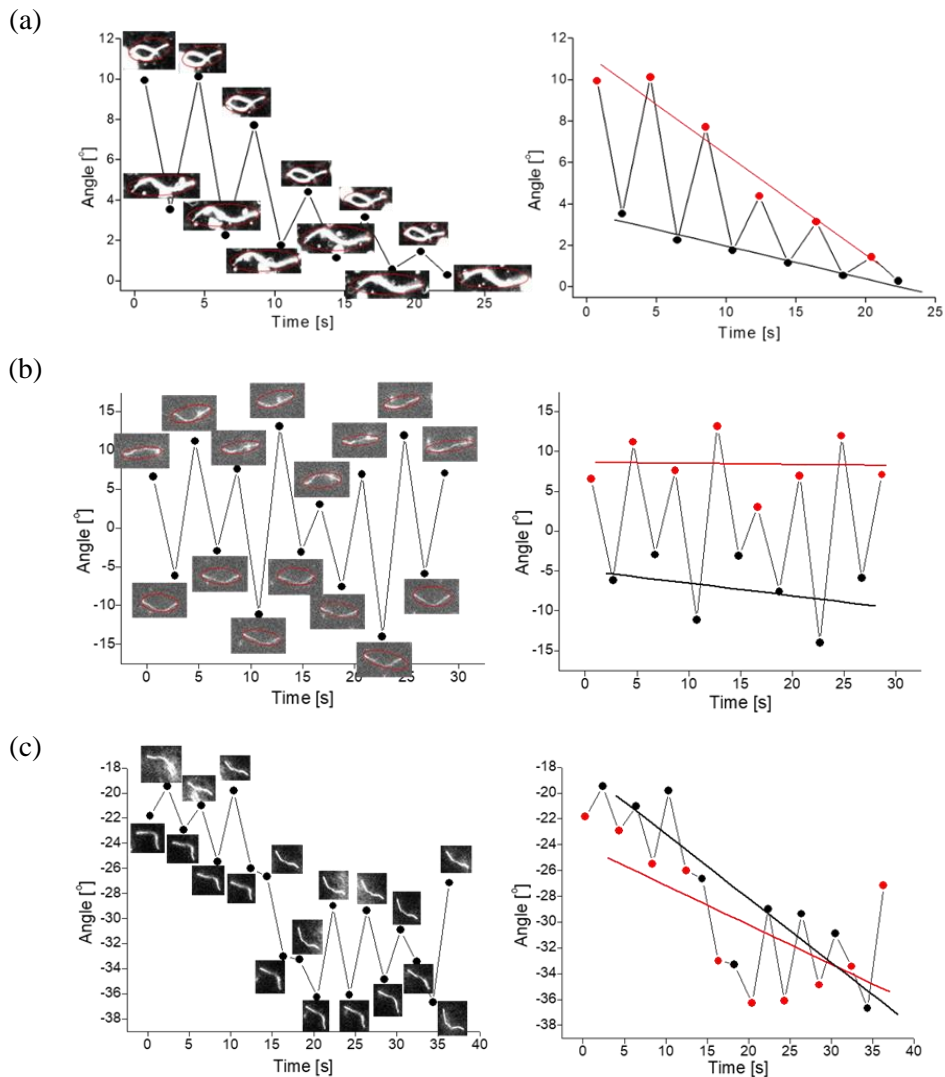
(a)

(b)

(c)

Figure 4.25. Changes in the inclination angle over time during the oscillatory flow; representative examples for bent-like (a), U-shaped buckled (b), and U-shaped stretched nanofilaments (c).

Fig. 4.25 (a) shows typical changes in the inclination angle of filaments from the bent-like filament group, characterized by coiling and uncoiling depending on the phase of the cycle. The values of the inclination angle corresponding to the same phase (0 or π) are clearly synchronized. In addition, the filaments in this group tend to be orientated along the flow.

Fig. 4.25 (b) shows the typical behaviour of U-shaped buckling filaments. These filaments are characterized by a lower inclination angle values in each phase. Looking at the trend line set for both phases of the cycle we can see (especially in phase 0) that it is parallel to the flow axis. This means that despite the oscillatory flow, this subgroup of filaments do not change their relative orientation, oscillating around the flow axis. We concluded that such filaments, moving with a high average velocity (250 μm/s), are carried by the fluid, without large shape changes and with small changes in the inclination angle.

A different behaviour can be seen in the U-shaped stretched filaments (Fig. 4.25 (c)). Their change in inclination angle is highly stochastic. We were also able to see that the observed filament deviated from the flow axis during the flow time. The main cause for this behaviour is the velocity with which the filaments in this group move (145 μm/s); as we showed in Fig. 4.23 (e), there is a progressive straightening of filaments over time.

During the experiment, the U-shaped stretched nanofilaments moved away from their alignment along the flow (Fig. 4.26, centre). At the same time, the orientation angle of the U-shaped buckled nanofilaments decreased over time (Fig. 4.26, right). The bent-like nanofilaments also aligned along the flow (Fig. 4.26, left), even though we applied a flow velocity lower than that of U-shaped buckled nanofilaments.

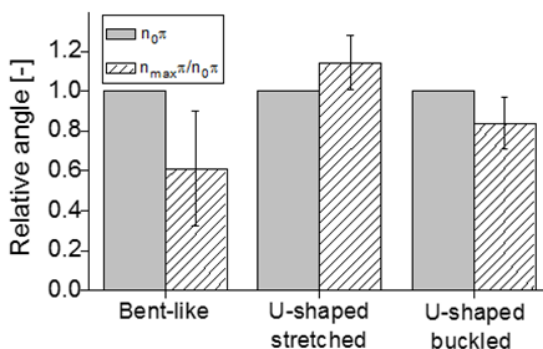Figure 4.26. Relative changes of the filament inclination angle after applying a flow: initial status (*grey bars*) and after the final oscillatory cycle (*dashed-patterned bars*). Data are normalized to the initial inclination angle.

Bent-like nanofilaments move to the regions where the value of the local shear rate is minimizing (channel centre). As the velocity of the oscillatory flow in the

microchannel centre reaches its maximum value, it can help increase the chain alignment. In the case of U-shaped buckled nanofilaments, the higher flow velocity helps to align filaments, but at the same time it prevents their straightening. In short, a higher flow velocity contributes to increasing the polymer chain orientation along the direction of the flow, and directs the chains closer to the microchannel centre, in accordance with the predictions of the model by Sadlej et al. [93].

4.6.8. Lateral migration of highly deformable nanofilaments

Our analysis of the objects suspended in the oscillatory flow also indicates their migratory behaviour across the channel. In the case of elongated objects such as filaments, this behaviour is quite complex and depends on several factors. Initially, the distribution of filaments across the channel geometry was rather uniform (Fig. 4.27), and the typical depletion layer was only observed close to the wall.
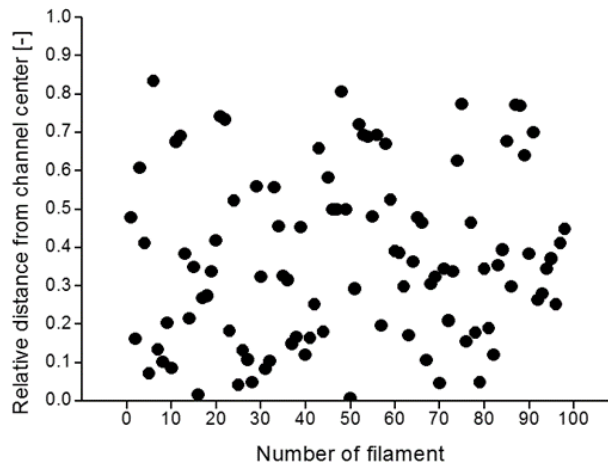

Figure 4.27. Initial distribution of 100 experimental sequences of investigated nanofilaments across the whole plane of the microchannel.

One of the most important parameters affecting the lateral migration and diffusivity of long polymers is the filament conformation. For this reason, the distribution of the centre-of-mass position for bent and U-shaped hydrogels was observed over time; it was characterized as a change in the relative distance from the channel centre (x), where 0 and 1 denote the microchannel centreline and wall, respectively. The aim of this investigation was to evaluate how the contour length of a nanofilament and its shape determine the cross-flow migration inside the microchannel. Both bent-like and U-shaped nanofilaments show in-phase fluctuations of their centre-of-mass position along the applied flow direction (Fig. 4.28 (a)). When we analysed the slip velocity, we observed that – due to changes in the filament's

orientation and shape – the variation of the slip velocity is outside of the oscillation flow phase (Fig. 4.28 (b)).

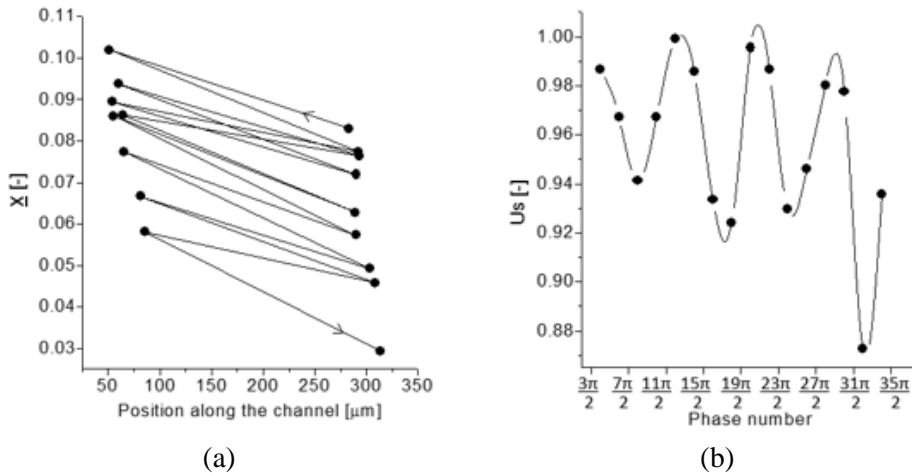(a)   (b)

Figure 4.28. Path of the cross-flow migration of nanofilament centre-of-mass position towards the axis of the microchannel in each phase of the oscillatory flow ($n\pi$, n = 1,2,3...); (b) Relative longitudinal slip velocity U_s of the nanofilament during each oscillating flow maximum ($n\pi/2$, n = 1,3,5...).

(a)   (b)
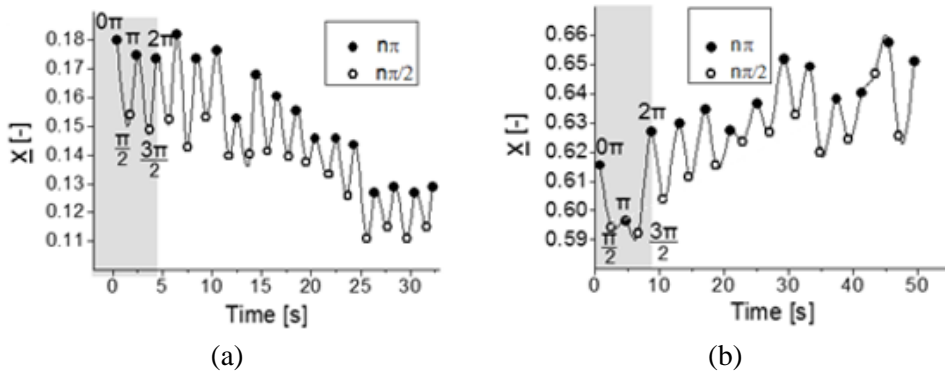
Figure 4.29. Trajectories of the centre-of-mass position of nanofilaments in the function of time: (a) towards the channel centre ($d = 105\ nm$, $L = 41\ \mu m$, $V_{max} = 250\ \mu m/s$, $U_r = 0.85\ 10^{-3}$; (b) towards the wall ($d = 134\ nm$, $L = 54\ \mu m$, $V_{max} = 132\ \mu m/s$, $U_r = 0.6\ 10^{-3}$.

Fig. 4.29 shows two examples of hydrogel nanofilament lateral migration trajectories.

As shown in Fig. 4.27, the initial distribution of filaments across the width of the microchannel was roughly uniform. However, in order to provide comparable conditions for analysing how the flow affected on the behaviour of the filaments, most of the experimental data were collected in a central part of the channel at a relative distance from the channel centre of 0.6, where shear forces are relatively uniform and

close to zero. Of course, the filaments closer to the wall were also analysed. Fig. 4.30 provides examples of graphs showing the cross-flow migration of the filaments observed near the microchannel wall, with an apparent net cross-flow migration of filaments from the wall.

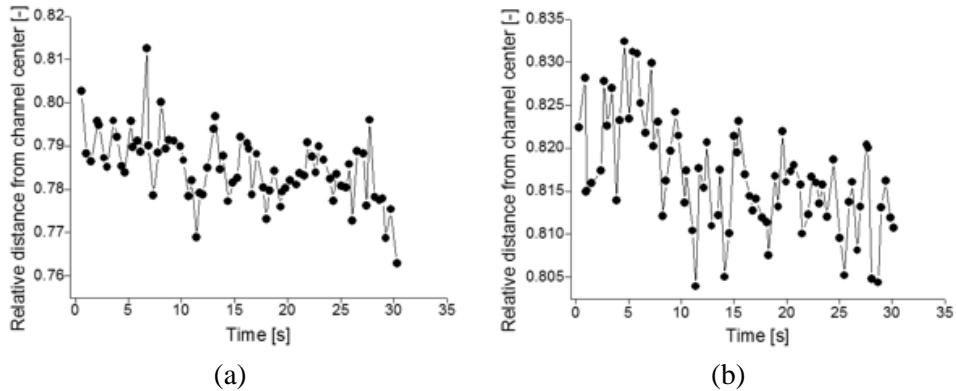(a)   (b)

Figure 4.30. Lateral migration of nanofilaments conveyed by the oscillating flow, observed close to the microchannel wall. Dots indicate the position of the centre of mass recorded at zero flow velocity ($n\pi/2$), (a) $d = 125$ nm, $L = 27$ μm, $V_{max} = 83$ μm/s, $U_r = 1.34 \cdot 10^{-3}$; (b) $d = 114$ nm, $L = 30$ μm, $V_{max} = 75$ μm/s, $U_r = 0.4 \cdot 10^{-3}$.

The initial distribution of nanofilaments observed across the width of the microchannel after introducing the flow is relatively uniform (Fig. 4.31, grey bars). Later on, in the presence of an oscillatory flow, the nanofilament distribution shifts (i) closer to the centreline of the microchannel in the case of bent nanofilaments, and (ii) further away for the U-shaped stretched nanofilaments (Fig. 4.31 (a), (b), black dotted lines).

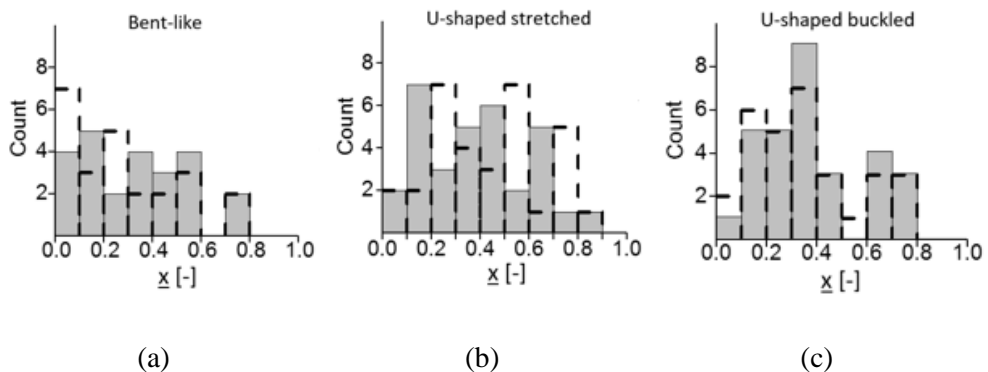(a)   (b)   (c)

Figure 4.31. The centre-of-mass distribution of hydrogel nanofilaments across the microchannel width $\underline{x}$ (0 and 1 denote the microchannel centreline and wall, respectively), before the application of the oscillating hydrodynamic force (*grey bars*), and after over 40 oscillatory cycles (*dashed-contour bars*).

Both types of U-shaped nanofilaments had a relative migration velocity of similar magnitude. High flow velocity values contributed to the migration of filaments towards the centreline of the microchannel. Such behaviour was visible in the case of the U-shaped buckled nanofilaments (Fig. 4.31 (c)). For comparison, the low magnitude of the flow velocity contributed to the lateral migration towards the wall, as in the case of the U-shaped stretched nanofilaments (Fig. 4.31 (b)). Therefore, it can be inferred that the direction of migration within the group of nanofilaments with a similar conformation is determined by the applied flow magnitude.

The relative velocity of this migration, however, seems to be marginally dependent on the magnitude of the oscillating flow applied. The same goes for the "slip velocity", the velocity of the filament related to the local flow velocity: for all the configurations analysed, it appeared to be very similar (Fig. 4.32).
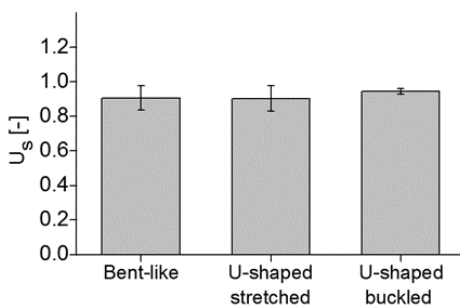

Figure 4.32. The relative slip velocity U_s of three different types of hydrogel nanofilaments.

The tendency of the chain to equilibrate its conformation in the presence of hydrodynamic forces determines the cross-flow migration. In the case of hydrogel nanofilaments, this depends both on the magnitude of the flow applied and on the initial shape. Bent-like nanofilaments are characterized by a cross-flow migration towards the microchannel centreline (Fig. 4.31 (a)). In this region, local shear rates are minimized and the chain conformations are not influenced by any additional deformations. In the case of migration towards the wall, this behaviour may induce the stretching of bent-like nanofilaments, owing to the increasing shear rate. It is also interesting that, in the case of U-shaped stretched nanofilaments, the same flow value velocity caused that migration in the opposite direction (towards the wall) (Fig. 4.31 (b)). When filaments migrate towards higher gradients, the alignment of the U-shaped stretched nanofilaments is not induced and filaments are tilted with respect to the flow direction. As de Pablo et al. suggested [111], in the case of limited by the wall geometry and at the high values of shear rates which are typical for DNA experiments, migration towards the wall can be weak. The reason for this is that the hydrodynamic migration effects of the two walls are cancelled, and also because the chain, which is stretched in the flow direction, is actually compacted in the wall-

normal direction, making it possible for its mass centre to come closer to the wall. Therefore, it seems necessary to conduct some additional studies to obtain further details on: (i) the complex interactions induced by the shear stress of the oscillatory flow, (ii) filament deformability as a result of the flow, (iii) their Brownian diffusivity, and (iv) filaments' tendency to cross-flow migrate.

The possible use of hydrogel nanofilaments as controlled drug release systems

Hydrogel nanofilaments are ideal materials for biomedical use, thanks to their material properties (no toxicity, their physical properties being close to those of living tissues) and shape parameters. Their small size, large surface area, and high flexibility make them ideal for use both as vehicles to carry drugs to specific places in the body, and as systems for the controlled release of drugs. For this reason, we have conducted a series of experiments which have confirmed the possibility to use hydrogel nanofilaments as systems for the controlled release of drugs.

5.1.   Samples preparation

For a protein release study, we analysed six samples of PNIPAAm (EN1–EN3): three samples of hydrogel nanofilaments, and three samples of mats obtained using core-shell nanofibres (with hydrogel core). Each of them contained 7 mg/ml BSA-FITC (Bovine Serum Albumin conjugated with fluorescein) as indicators of the drug release process [112]. Results were then compared with the material of core-shell nanofibres without hydrogel in their core structure. For testing one type of hydrogel nanofilaments, the 3 cm^2 piece of nanofibre mat was weighed to determine its BSA-FITC content. Then, to extract the nanofilaments, the polymer shell of fibres was dissolved in 1 ml of DMF. The nanofilament solution was diluted with 2.5 ml deionised water. After vigorously shaking the vial, we transferred three samples of 1 ml each into plastic vials. For the first sample (1st vial) we waited 1 hour for the BSA-FITC release from nanofilaments (in an incubator with a 37°C temperature), and then we centrifuged the sample for 10 minutes at 10,000 rpm. This process was necessary to separate the nanofilaments from the supernatant. We then transferred this liquid to clean plastic vials. This procedure was applied to the next two samples (in two other vials) after 6 and 24 hours from release, respectively.

To study the release from the nanofibre mat, we used 1 cm^2 of core-shell nanofibre material, weighed it, immersed it in 1 ml of deionised water, and incubated it at 37°C. After 1, 6, and 24 hours the supernatant fluid was replaced by fresh water.

Fluorescein conjugated with BSA served as a marker to determine the concentration of the released factor. To measure the fluorescent intensity by a fluorimeter (Fluoroskan AscentTM Microplate Fluorometer, Thermo Scientific, USA), 300 μl of each collected supernatant were placed in a 96-well microplate. The calibration curve which had been prepared earlier was used to calculate the concentration of the protein released. Additionally, we employed the Fluorescence Recovery After Photobleaching (FRAP) method, using a Leica TCS SP5 microscope, to evaluate the diffusion coefficient of BSA-FITC in EN1 hydrogel (37°C).

5.2.   Results and discussion

The following two charts show the results for the release kinetics of BSA-FITC from (i) the hydrogel material trapped in the core of nanofibres (Fig. 5.1) and (ii) from the nanofilaments extracted (Fig. 5.2).
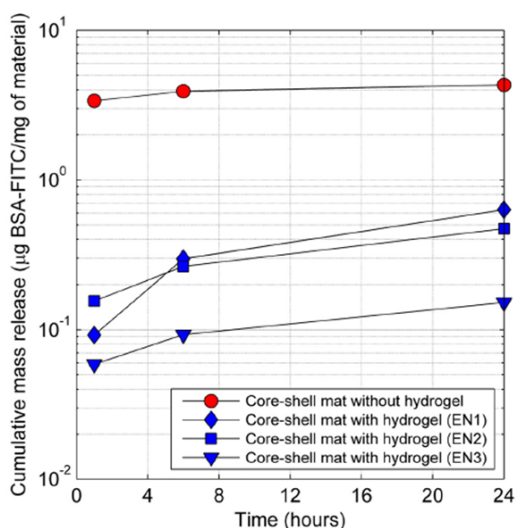
Figure 5.1. Cumulative release of BSA-FITC from: core-shell mat with NIPA hydrogel in the core (EN1-EN3), and core-shell mat with protein water solution in the core (without hydrogel). For a better visibility of results, the y-axis is in a logarithmic scale. Standard deviation was less than 5%.

We compared them with the results obtained for simple nanofibre materials with BSA-FITC. Such materials had been previously used for the drug release modelling by Nakielski et al. [113]. There was a substantial increase in the proteins released from

the nanofilaments still trapped in the core of the nanofibre mat, compared to the proteins released from nanofilaments alone. The reason for this result is probably that the shell polymer precipitates after the addition of water to dissolved materials and after nanofilament absorption, thus preventing the access to the fluid.

After 24 hours, we observed an almost seven-times-lower protein release profile from the material with PNIPAAm hydrogel in the core (EN1) than in the case of the material without hydrogel in the core structure. Similar results were observed by Nakielski et al. [113, 114].

When we look at the characterization of the protein release kinetics for different compositions of materials (Fig. 5.1), we see the lowest release for nanofibre mats with the highest degree of hydrogel crosslinking (EN3), and the highest release for the lowest degree of the hydrogel crosslinking (EN1) after 24 hours. When nanofilaments were extracted from core-shell nanofibres after 24 hours, the release rate for EN1 nanofilaments was the highest (Fig. 5.2).
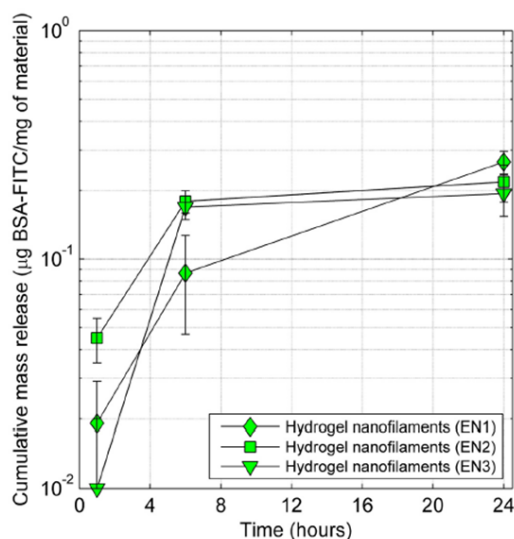
Figure 5.2. BSA-FITC cumulative release from three different compositions of hydrogel nanofilaments. The y-axis is in a logarithmic scale.

The absence of hydrogel in the core led to a burst release, probably caused by a protein solution leakage through some nano ruptures in the nanofibre shell. It should be remembered that the BSA-FITC diffusion coefficient in hydrogel EN1 ($D_{BSA-FITC} = 7.3 \pm 3.7 \ \mu m^2/s$) is three orders of magnitude smaller than its diffusion coefficient in water [115]. For that reason, we can observe a significantly prolonged release from the hydrogel.

We demonstrated the possibility to use core-shell nanofibres with hydrogel filaments and hydrogel nanofilaments as a drug delivery system. Such a system is

based on a hydrogel core delivery and shows a slower release and absence of burst release when compared to materials without hydrogel. It is also interesting to note that the change in proportions between the monomers which form the hydrogel is affecting the diffusion coefficient. These important results will make it possible to adjust the release profile by changing the hydrogel composition.

6

Conclusions

The behaviour of micro and nanoobjects suspended in fluids is a widely studied issue, in the context of both basic research and potential applications. Without a doubt, the current achievements of nanotechnologies have led to their extensive application studies in biology, medicine, and material engineering. In order to be able to discuss the future applications of these materials, it is necessary to be familiar with all their characteristics.

The research conducted on the mobility of spherical nanoparticles under the influence of thermal fluctuations has confirmed that there are numerous factors affecting this mobility. The ionic strength of the medium is one of the most important factors that have a significant impact on the hydrodynamic diameter of nanoparticles. The impact of the environment is essential for estimating the diffusion of nanoparticles and biological macromolecules. It is also important for evaluating the so called "slip velocity", an apparent deviation from the sticky kinematic boundary conditions in nanoscale experiments. Knowing the impact that the environment of biological particles has on the value of the hydrodynamic diameter, it will be possible to estimate the actual size of these molecules and understand their diffusion process.

The second part of the research concerned more complex structures in terms of shape and behaviour – hydrogel nanofilaments. These objects are characterized by high flexibility, while their mechanical behaviour can mimic long biological molecules. We studied our hydrogel nanofilaments for Brownian motion, bending dynamics, and migration. The results we obtained showed that the diffusion coefficients of our flexible hydrogel nanofilaments differ from the theoretical predictions based on a drag force for stiff ellipsoidal nanoobjects. We have also shown that hydrogel nanofilaments are characterized by a great flexibility, which is an essential parameter in the context of future applications. Therefore, for future models, the application of a better approach that would take into account long and deformable objects is necessary. The creation of models of filaments with variable stiffness and dimensions is a great challenge for future theoreticians. The biocompatibility of hydrogel materials, as well as the mechanical properties mentioned above, opens up a number of possible biomedical applications for our nanofilaments.

Depending on their typical in-flow behaviour and shape change, we divided nanofilaments into three groups: bent-like, U-shape backed, and U-shape stretched filaments. Studies on the influence of the oscillatory flow on their dynamics have shown that nanofilaments can be used as models of elastic biopolymers, such as actin filaments or DNA molecules. This is related to the fact that hydrogel nanofilaments and biomolecules are characterized by similar hydrodynamic reactions. Another important result we obtained is the demonstration of the ability of hydrogel nanofilaments to migrate laterally. The direction of their migration depends on the group to which a nanofilament belongs, while their velocity is comparable to the bead-spring model, which was developed at IPPT PAN.

We showed that by changing the content of the hydrogel-forming crosslinking factor, the speed and efficiency of the marker release (for example drug) is affected. Furthermore, the presence of a hydrogel in the core-shell structure of nanofibre mats prevents the almost immediate release of all the drug it contains.

In the future, our electrospun hydrogel nanofilaments could be useful for more systematic studies which will be focused on the development and optimization of microfluidic devices for the sorting of biopolymer and lab-on-a-chip technologies. A particular interest is focused on the use of such flexible polymeric nanoobjects as specialized biomimetic networks for targeting drug delivery and local tissue regeneration. Hydrogel nanofilaments may also be a useful experimental model for elucidating the role of hydrodynamic interactions in describing the physical phenomena responsible for the processes of folding and bending of long molecular chains (e.g. proteins, DNA).

Based on the performed experiments we are in a position to conclude:
1) We showed that the mobility of spherical nanoparticle depends on several factors that affect the hydrodynamic diameter value. Factors influencing the effective diffusivity of nanoparticles by changing the size of hydrodynamic diameter include: ionic strength of medium, valence of salt, size of ions and distance from the channel wall.
2) We presented that the oscillatory flow in microchannel is a very promising tool for investigating micro- and nanoobjects behaviours. A full understanding of this behaviour in a flow which simulates intercellular motion of biomolecules inside the body opened new possibilities for biomedical application as: systems for controlled release of drugs, nanocarriers capable to delivery drugs in specific body tissue, local tissue regeneration.
3) We confirmed that flexible hydrogel nanofilaments can be used as experimental model to elucidate the role of hydrodynamic interactions in describing physical phenomena responsible for the processes of folding and bending of long molecular chains (e.g. proteins, DNA).

Bibliography

1. M. Kochańczyk, J. Jaruszewicz, T. Lipniacki. Stochastic transitions in a bistable reaction system on the membrane. *Journal of The Royal Society Interface*, 10(84):1-12, 2013.

2. J. Jaruszewicz, P. J. Żuk, T. Lipniacki. Type of noise defines global attractors in bistable molecular regulatory systems. *Journal of Theoretical Biology*, 317:140-151, 2013.

3. S. Tay, J. J.Hughey, T. K. Lee, T. Lipniacki, S. R. Quake, M. W. Covert. Single-cell NF-kB dynamics reveal digital activation and analogue information processing. *Nature*, 466:267-271, 2010.

4. R. A. Kellogg, C. Tian, T. Lipniacki, S. R. Quake, S. Tay. Digital signaling decouples activation probability and population heterogeneity. *eLIFE*, 4:e08931-1-26, 2015.

5. W. Pabst, E. Gregorova. *Characterization of particles and particle systems*. ICT Prague, 2007.

6. I. Lisiecki, M . Björling, L. Motte, B. Ninham, M. P. Pileni. Synthesis of copper nanosize particles in anionic reverse micelles: effect of the addition of a cationic surfactant on the size of the crystallites. *Langmuir*, 11(7):2385-2392, 1995.

7. S. Mondini, C. Drago, A. M. Ferretti, A. Puglisi, A. Ponti. Colloidal stability of iron oxide nanocrystals coated with a PEG-based tetra-catechol surfactant. *Nanotechnology*, 24:105702-1-14, 2013.

8. R.-Y. Dong, Y. Zhou, C. Yang, B.-Y. Cao. Experimental study on thermophoresis of colloids in aqueous surfactant solutions. *J. Phys.: Condens. Matter*, 2:495102-1-9, 2015.

9. W. Brown, J. Zhao. Adsorption of sodium dodecyl sulfate on polystyrene latex particles using dynamic light scattering and zeta potential measurements. *Macromolecules*, 26(11):2711-2715, 1993.

10. L. K. Koopal, E. M. Lee, M. R. Bohmer. Adsorption of cationic and anionic surfactants on charged metal-oxide surfaces. *J. Colloid Interface Sci.*, 170:85-97, 1995.

11. M. Elimelech, C. R. O'Melia. Effect of particle size on collision efficiency in the deposition of brownian particles with electrostatic energy barriers. *Langmuir*, 6(6):1153-1163, 1990.

12.   K. Suttiponparnit, J. Jiang, M. Sahu, S. Suvachittanont, T. Charinpanitkul, P. Biswas. Role of surface area, primary particle size, and crystal phase on titanium dioxide nanoparticle dispersion properties. *Nanoscale Res. Lett.*, 6(27):1-8, 2011.

13.   J. Jiang, G. Oberdörster, P. Biswas. Characterization of size, surface charge, and agglomeration state of nanoparticle dispersions for toxicological studies. *J. Nanopart. Res.*, 11:77-89, 2009.

14.   R. Finsy. Particle sizing by quasi-elastic light scattering. *Advances in Colloid and Interface Science*, 52:79-143, 1994.

15.   M. R. Gittings, D. A. Saville. The determination of hydrodynamic size and zetapotential from electrophoretic mobility and light scattering measurements. *Colloids Surf. A*, 141:111-117, 1998.

16.   R. Xu. Shear plane and hydrodynamic diameter of microspheres in suspension. *Langmuir*, 14:2593-2597, 1998.

17.   Ch.-H. Fischer, E. Kenndler. Analysis of colloids IX. Investigation of the electrical double layer of colloidal inorganic nanometer-particles by size-exclusion chromatography. *J. Chromatogr. A*, 773:179-187, 1997.

18.   X. Bian, C. Kim, G. E. Karniadakis. 111 years of Brownian motion. *Soft Matter*, 12:6331-6346, 2016.

19.   M. A. Charsooghi, E. A. Akhlaghi, S. Tavaddod, H. R. Khalesifard. A MATLAB program to calculate translational and rotational diffusion coefficients of a single particle. *Computer Physics Communications*, 182:400-408, 2011.

20.   A. J. Levine, T. B. Liverpool, F. C. MacKintosh. Mobility of extended bodies in viscous films and membranes. *Phys. Rev. E*, 69:021503-1-10, 2004.

21.   A. Ortega, J. Garcia de la Torre. Hydrodynamic properties of rodlike and disklike particles in dilute solution. *J. Chem. Phys.*, 119(18):9914-9919, 2003.

22.   A. M. Słowicka, M. L. Ekiel-Jeżewska, K. Sadlej, E. Wajnryb. Dynamics of fibres in a wide microchannel. *J. Chemical Physics*, 136:044904-1-8, 2012.

23.   A. M. Słowicka, E. Wajnryb, M. L. Ekiel-Jeżewska. Lateral migration of flexible fibres in Poiseuille flow between two parallel planar solid walls. *Eur. Phys. J. E*, 36(31):1-12, 2013.

24.   P. Szymczak, M. Cieplak. Influence of hydrodynamic interactions on mechanical unfolding of proteins. *J. Phys.: Condens. Matter*, 19:285224-1-12, 2007.

25.   M. Bukowicki, M. L. Ekiel-Jeżewska. Different bending models predict different dynamics of sedimenting elastic trumbbells. *Soft Matter*, 2018 (in print).

26.   D. R. Steinhauser. *Actin filaments and bundles in flow*. PhD Thesis, Georg August University of Göttingen, Göttingen, 2008.

27. R. G. Larson. The rheology of dilute solutions of flexible polymers: progress and problems. *Journal of Rheology*, 49(1):1-70, 2005.

28. G. B. Jeffery. The motion of ellipsoidal particles immersed in a viscous fluid. *Proc. Roy. Soc. A*, 102:161-179, 1922.

29. L. C. Nitsche, E. J. Hinch. Shear-induced lateral migration of Brownian rigid rods in parabolic channel flow. *J. Fluid Mech.*, 332:1-21, 1997.

30. C. Bustamante, J. F. Marko, E. D. Siggia, S. Smith. Entropic elasticity of λ-phage DNA. *Science*, 265:1599-1600, 1994.

31. Y. Z. Zhang, C.T. Lim, S. Ramakrishna, Z.-M. Huang. Recent development of polymer nanofibers for biomedical and biotechnological applications. *J. Mater Science Mater Med.*, 16(10):933-946, 2005.

32. G. Verreck, I. Chun, J. Rosenblatt, J. Peeters, A. V. Dijck, J. Mensch, M. Noppe, M. E. Brewster. Incorporation of drugs in an amorphous state into electrospun nanofibers composed of a water insoluble, nonbiodegradable polymer. *J. Controlled Release*, 92:349-360, 2003.

33. W. Cui, Y. Zhou, J. Chang. Electrospun nanofibrous materials for tissue engineering and drug delivery. *Sci. Technol. Adv. Mater.*, 11:014108-1-11, 2010.

34. S. Pawłowska. *Dynamics of nano objects suspended in liquids: experimental analysis*. Ph.D. Thesis, IPPT PAN, Warsaw 2018. (http://fluid.ippt.pan.pl/papers/PhD/PhD_Pawlowska2018.pdf)

35. E. S. Medeiros, G. M. Glenn, A. P. Klamczynski, W. J. Orts, L. H. C. Mattoso. Solution blow spinning: a new method to produce micro- and nanofibres from polymer solutions. *Journal of Applied Polymer Science*, 113:2322-2330, 2009.

36. T . Grafe, K. Graham. *Polymeric nanofibres and nanofibre webs: a new class of nonwovens*. International Nonwovens Technical Conference, Atlanta, Georgia, 2002.

37. P. Nakielski, S. Pawlowska, F. Pierini, V. Liwinska, P. Hejduk, K. Zembrzycki, E. Zabost, T. A. Kowalewski. Hydrogel nanofilaments via core-shell electrospinning. *PLoS ONE*, 10(6): e0129816-1-16, 2015.

38. H. Qu, S. Wei, Z. Guo. Coaxial electrospun nanostructures and their applications. *J. Mater. Chem. A*, 1:11513-11528, 2013.

39. D.-G. Yu, J. H. Yu, L. Chen, G. R. Williams, X. Wang. Modified coaxial electrospinning for the preparation of high-quality ketoprofen-loaded cellulose acetate nanofibers. *Carbohydr Polym.*, 90:1016-1023, 2012.

40. M. F. Elahi, W. Lu, G. Guoping, F. Khan. Core-shell fibres for biomedical applications - A review. *J. Bioengineer and Biomedical Sci.*, 3(1):1-14, 2013.

41. A. V. Bazilevsky, A. L. Yarin, C. M. Megaridis. Co-electrospinning of core−shell fibres using a single-nozzle technique. *Langmuir*, 23:2311-2314, 2007.

42. Ch. Wang, L. Wang, M. Wang. Evolution of core-shell structure: from emulsions to ultrafine emulsion electrospun fibres. *Materials Letters*, 124:192-196, 2014.

43. J. D´ıaz, A. Barrero, M. M´arquez, I. Loscertales. Controlled encapsulation of hydrophobic liquids in hydrophilic polymer nanofibres by co-electrospinning. *Adv. Funct. Mater.*, 16:2110-2116, 2006.

44. Z. Maolin, L. Jun, Y. Min, H. Hongfei. The swelling behavior of radiation prepared semi-interpenetrating polymer networks composed of polyNIPAAm and hydrophilic polymers. *Radiation Physics and Chemistry*, 58:397-400, 2000.

45. F. Sabbagh, I. I. Muhamad. Acrylamide-based hydrogel drug delivery systems: release of acyclovir from MgO nanocomposite hydrogel. *Journal of the Taiwan Institute of Chemical Engineers*, 72:182-193, 2017.

46. M. Kurečič, M. Sfiligoj-Smole, K. Stana-Kleinschek. UV polymerization of poly (N-isopropylacrylamide) hydrogel. *Materials and Technology*, 46(1):87-91, 2012.

47. J. R. Tse, A. J. Engler. *Current protocols in cell biology: preparation of hydrogel substrates with tunable mechanical properties*. John Wiley & Sons, Inc., supplement 47:10.161-16, 2010.

48. T. Kanai, D. Lee, H. C. Shum, D. A. Weitz. Fabrication of tunable spherical colloidal crystals immobilized in soft hydrogels. *Small Journal*, 6(7):807-810, 2010.

49. Z. Wei, Z. Jia, J. Athas, C. Wang, S. R. Raghavan, T. Li, Z. Nie. Hybrid hydrogel sheets that undergo pre-programmed shape transformations. *Soft Matter*, 10:8157-8162, 2014.

50. Y. Ono, T. Shikata. Hydration and dynamic behavior of poly(n-isopropylacrylamide)s in aqueous solution: a sharp phase transition at the lower critical solution temperature. *J. Am. Chem. Soc.*, 128(31):10030–10031, 2006.

51. J. H. Priest, S. L. Murray, R. J. Nelson, A. S. Hoffma. *Reversible polymeric gels and related systems: lower critical solution temperatures of aqueous copolymers of N-isopropylacrylamide and other N-substituted acrylamides*. American Chemical Society, Washington, DC, 255-264, 1987.

52. K. Zembrzycki, S. Pawłowska, P. Nakielski, F. Pierini. *Development of a hybrid Atomic Force Microscope and Optical Tweezers apparatus*. IPPT Reports on Fundamental Technological Research, 2:1-58, 2016.

53. C. Chassagne, M. Ibanez. Hydrodynamic size and electrophoretic mobility of latex nanospheres in monovalent and divalent electrolytes. *Colloids and Surfaces A: Physicochem. Eng. Aspects*, 440:208-216, 2014.

54. Y. Sun. New interpretation for laser light scattering. arXiv:physics/0511159v1, 2005.

55. J. Gross, S. Sayle, A. R. Karow, U. Bakowsky, P. Garidel. Nanoparticle tracking analysis of particle size and concentration detection in suspensions of polymer and protein samples: influence of experimental and data evaluation parameters. *European Journal of Pharmaceutics and Biopharmaceutics*, 104:30-41, 2016.

56. D. H. Everett. Basic principles of colloid science. *The Royal Society of Chemistry*, 130-134, 1988.

57. www.therom.com/particletechnology

58. M. L. Bleam, C. F. Anderson, M. T. J. Record. Relative binding affinities of monovalent cations for double-stranded DNA. *Proc. Natl Acad. Sci. USA*, 77(6):3085-3089, 1980.

59. Y. Wang, I. A. Weinstock. Polyoxometalate-decorated nanoparticles. *Chem. Soc. Rev.*, 41:7479-7496, 2012.

60. K. Bohinc, V. Kralj-Iglic, A. Iglic. Thickness of electrical double layer. Effect of ion size. *Electrochimica Acta*, 46:3033-3040, 2001.

61. A. E. Larsen, D. G. Grier. Like-charge attractions in metastable colloidal crystallites. *Nature*, 385:230-233, 1997.

62. C. A. Murray. When like charges attract. *Nature News and Views*, 385:203-204, 1997.

63. S. Assemi, J. Nalaskowski, W. P. Johnson. Direct force measurements between carboxylate-modified latex microspheres and glass using atomic force microscopy. *Colloids and Surfaces A: Physicochem. Eng. Aspects*, 286:70-77, 2006.

64. F. Pierini, K. Zembrzycki, P. Nakielski, S. Pawłowska, T. A. Kowalewski. Atomic force microscopy combined with optical tweezers (AFM/OT). *Meas. Sci. Technol.*, 27:025904-1-11, 2016.

65. G. Segre, A. Silberberg. Behaviour of macroscopic rigid spheres in Poiseuille flow. Part2. Experimental results and interpretation. *J. Fluid Mech.*, 14:136-157, 1962.

66. F. J. Gauthier, H. L. Goldsmith, S. G. Mason. Flow of suspensions through tubes – X. Liquid drops as models of erythrocytes. *Biorheology*, 9:205-224, 1972.

67. P. C. H. Chan, L. G. Leal. Motion of a deformable drop in a second order fluid. *J. Fluid Mech.*, 92:131-170, 1979.

68. W. Hiller, T. A. Kowalewski. An experimental study of the lateral migration of a droplet in a creeping flow. *Exp. in Fluids*, 5:43-48, 1987.

69. X. Chen, Ch. Xue, L. Zhang, G. Hu., X. Jiang, J. Sun. Inertial migration of deformable droplets in a microchannel. *Phys. Fluids*, 26:112003-1-25, 2014.

70. B. P. Ho, L. G. Leal. Inertial migration of rigid spheres in two-dimensional unidirectional flows. *J. Fluid Mech.*, 65(2):365-400, 1974.

71. G. Segre, A. Silberberg. Radial particle displacements in Poiseuille flow of suspensions. *Nature*, 189:209-210, 1961.

72. A. Brandt, G. Bugliarello. Concentration redistribution phenomena in the shear flow of monolayers of suspended particles. *Trans. Soc. Rheo.*, 10(1):229-251, 1966.

73. A. D. Maude, J. A. Yearn. Particle migrations in suspension flows. *J. Fluid Mech.*, 30:601-621, 1967.

74. W. S. Rasband, ImageJ, U. S. National Institutes of Health, Bethesda, Maryland, USA, 1997-2014, 2014. Available: http://www.imagej.nih.gov/ij.

75. Matlab, Mathworks, www.mathworks.com, 2014

76. B. Bhaduri, A. Neild, T. W. Ng. Directional Brownian diffusion dynamics with variable magnitudes. *Appl. Phys. Lett.*, 92(8):084105-1-3, 2008.

77. E. P. Tan, C. T. Lim. Mechanical characterization of nanofibers - A review. *Compos Sci Technol.*, 66:1102-1111, 2006.

78. M. Ahearne, Y. Yang, A. J. El Haj, K. Y. Then, K.-K. Liu. Characterizing the viscoelastic properties of thin hydrogel-based constructs for tissue engineering applications. *Journal of The Royal Society Interface*, 2:455-463, 2005.

79. S. Kasas, G. Longo, G. Dietler. Mechanical properties of biological specimens explored by atomic force microscopy. *J. Phys. D: Appl. Phys.*, 46:133001-1-12, 2013.

80. F. Gittes, B. Mickey, J. Nettleton, J. Howard. Flexural rigidity of microtubules and actin filaments measured from thermal fluctuations in shape. *The Journal of Cell Biology*, 120(4):923–934, 1993.

81. A. Ott, M. Magnasco, A. Simon, A. Libchaber. Measurement of the persistence length of polymerized actin using fluorescence microscopy. *Physical Review E*, 48(3):R1642-R1645, 1993.

82. M. Kikumoto, M. Kurachi, V. Tosa, H. Tashiro. Flexural rigidity of individual microtubules measured by a buckling force with optical traps. *Biophysical Journal*, 90:1687-1696, 2006.

83. J. S. Graham, B. R. McCullough, H. Kang, W. A. Elam, W. Cao, E. M. De La Cruz. Multi-platform compatible software for analysis of polymer bending mechanics. *PLoS ONE*, 9(4):e94766-1-6, 2014.

84. N. Mücke, K. Klenin, R. Kirmse, M. Bussiek, H. Herrmann, M. Hafner, J. Langowski. Filamentous biopolymers on surfaces: atomic force microscopy images compared with brownian dynamics simulation of filament deposition. *PLoS ONE*, 4(11):e7756-1-7, 2009.

85. T. B. Liverpool. Active gels: where polymer physics meets cytoskeletal dynamics. *Phil. Trans. R. Soc. A*, 364:3335-3355, 2006.

86. V. Kantsler, R. E. Goldstein. Fluctuations, dynamics, and the stretch-coil transition of single actin filaments in extensional flows. *Phys. Rev. Lett.*, 108(3):038103-1-5, 2012.

87. L. Li, H. Manikantan, D. Saintillan, S. E. Spagnolie. The sedimentation of flexible filaments. *J. Fluid Mech.*, 735:705-736, 2013.

88. H. M. Lopez, J.-P. Hulin, H. Auradou, M. D'Angelo. Deformation of a flexible fiber in a viscous flow past an obstacle. *Phys. Fluids*, 27:013102-1-12, 2015.

89. B. Delmotte, E. Climent, F. Plouraboue. A general formulation of Bead Models applied to flexible fibres and active filaments at low Reynolds number. *Journal of Computational Physics*, 286:14-37, 2015.

90. G. A. Evingür, Ö. Pekcan. Elastic properties of a swollen PAAm-NIPA copolymer with various NIPA contents. *Polymer-Plastics Technology and Engineering*, 53:834-839, 2014.

91. O. San, A. E. Staples. An improved model for reduced-order physiological fluid flows. *J. Mech. Med. Biol.*, 12(3):1250052-1-28, 2012.

92. S. Pawłowska. Highly deformable nanofilaments in flow. *Journal of Physics: Conference Series*, 760:012022-1-10, 2016.

93. K. Sadlej, E. Wajnryb, M. L. Ekiel-Jezewska, D. Lamparska, T. A. Kowalewski. Dynamics of nanofibres conveyed by low Reynolds number flow in a microchannel. *Int. J. Heat Fluid Flow*, 31:996-1004, 2010.

94. K. Jo, Y. L. Chen., J. J. de Pablo, D. C. Schwartz. Elongation and migration of single DNA molecules in microchannels using oscillatory shear flows. *Lab on a Chip*, 9(16):2348-2355, 2009.

95. D. Steinhauser, S. Köster, T. Pfohl. Mobility gradient induces cross-streamline migration of semiflexible polymers. *ACS Macro Lett.*, 1:541-545, 2012.

96. B. Nöding, S. Köster. Intermediate filaments in small configuration spaces. *Phys. Rev. Lett.*, 108(8):088101-1-4, 2012.

97. K.S. Bloom. Beyond the code: the mechanical properties of DNA as they relate to mitosis. *Chromosoma*, 117(2):103-110, 2008.

98. S. Pawłowska, P. Nakielski, F. Pierini, I. K. Piechocka, K. Zembrzycki, T. A. Kowalewski. Lateral migration of electrospun hydrogel nanofilaments in an oscillatory flow. *PLoS ONE*, 12(11): e0187815-1-21, 2017.

99. S. Birner, C. Uhl, M. Bayer, P. Vogl. Theoretical model for the detection of charged proteins with a silicon-on-insulator sensor. *J. Phys.: Conf. Ser.*, 107:012002-1-15, 2008.

100. P. Jurney, R. Agarwal, V. Singh, K. Roy, S. V. Sreenivasan, L. Shi. Size-dependent nanoparticle margination and adhesion propensity in a microchannel. *Journal of Nanotechnology in Engineering and Medicine*, 4:031002-1-7, 2013.

101. N. Quennouz, M. Shelley, O. du Roure, A. Lindner. Transport and buckling dynamics of an elastic fibre in a viscous cellular flow. *J. Fluid Mech.*, 769:387-402, 2015.

102. E. Wandersman, N. Quennouz, M. Fermigier, A. Lindner, O. du Roure. Buckled in translation. *Soft Matter*, 6:5715-5719, 2010.

103. P. LeDuc, C. Haber, G. Bao, D. Wirtz. Dynamics of individual flexible polymers in a shear flow. *Nature*, 399:564-566, 1999.

104. Y.J. Chen, S. Johnson, P. Mulligan, A.J. Spakowitz, R. Phillips. Modulation of DNA loop lifetimes by the free energy of loop formation. *Proc. Natl. Acad. Sci.*, 111(49):17396-17401, 2014.

105. A. Izmitli, D.C. Schwartz, M.D. Graham, J.J. de Pablo. The effect of hydrodynamic interactions on the dynamics of DNA translocation through pores. *J. Chem. Phys.*, 128(8):085102-1-7, 2008.

106. O. Kratky, G. Porod. Röntgenuntersuchung gelöster Fadenmoleküle. *Rec. Trav. Chim. Pays-Bas.*, 68:1106-1122, 1949.

107. S. Reddig, H. Stark. Cross-streamline migration of a semiflexible polymer in a pressure driven flow. *J. Chem. Phys.*, 135:165101-1-11, 2011.

108. A. Farutin, T. Piasecki, A.M. Słowicka, Ch. Misbah, E. Wajnryb, M.L. Ekiel-Jezewska. Dynamics of flexible fibers and vesicles in Poiseuille flow at low Reynolds number. *Soft Matter*, 12(35):7307-23, 2016.

109. M. Harasim, B. Wunderlich, O. Peleg, M. Kröger, A. R. Bausch. Direct observation of the dynamics of semiflexible polymers in shear flow. *Physical Review Letters*, 110:108302-1-5, 2013.

110. R. Chelakkot, R.G. Winkler, G. Gompper. Migration of semiflexible polymers in microcapillary flow. *EPL*, 91(1):14001-1-6, 2010.

111. J.J. de Pablo, H.C. Ottinger, Y. Rabin. Hydrodynamic changes of the depletion layer of dilute polymer solutions near a wall. *AIChE J.*, 38(2):273-283, 1992.

112. T. Kowalczyk, A. Nowicka, D. Elbaum, T. A. Kowalewski. Electrospinning of bovine serum albumin. Optimization and the use for production of biosensors. *Biomacromolecules*, 9(7):2087-2090, 2008.

113. P. Nakielski, T. Kowalczyk, K. Zembrzycki, T. A. Kowalewski. Experimental and numerical evaluation of drug release from nanofiber mats to brain tissue. *J. Biomed. Mater. Res. B: Applied Biomaterials*, 103(2):282-291, 2015.

114. P. Nakielski. *Systemy uwalniania leków oparte na nanowłóknach*. IPPT Reports on Fundamental Technological Research, 1:1-216, 2015.

115. A. Shkilnyya, P. Proulxb, J. Sharpa, M. Lepagec, P. Vermette. Diffusion of rhodamine B and bovine serum albumin in fibrin gels seeded with primary endothelial cells. *Colloids and Surfaces B: Biointerfaces*, 93:202-207, 2012.